



A Model Rotor in Axial Flight

K. W. McAlister, S. S. Huang, and A. I. Abrego

DISTRIBUTION STATEMENT A:
Approved for Public Release -
Distribution Unlimited

June 2001

20021029 051

The NASA STI Program Office ...in Profile

Since its founding, NASA has been dedicated to the advancement of aeronautics and space science. The NASA Scientific and Technical Information (STI) Program Office plays a key part in helping NASA maintain this important role.

The NASA STI Program Office is operated by Langley Research Center, the Lead Center for NASA's scientific and technical information. The NASA STI Program Office provides access to the NASA STI Database, the largest collection of aeronautical and space science STI in the world. The Program Office is also NASA's institutional mechanism for disseminating the results of its research and development activities. These results are published by NASA in the NASA STI Report Series, which includes the following report types:

- **TECHNICAL PUBLICATION.** Reports of completed research or a major significant phase of research that present the results of NASA programs and include extensive data or theoretical analysis. Includes compilations of significant scientific and technical data and information deemed to be of continuing reference value. NASA's counterpart of peer-reviewed formal professional papers but has less stringent limitations on manuscript length and extent of graphic presentations.
- **TECHNICAL MEMORANDUM.** Scientific and technical findings that are preliminary or of specialized interest, e.g., quick release reports, working papers, and bibliographies that contain minimal annotation. Does not contain extensive analysis.
- **CONTRACTOR REPORT.** Scientific and technical findings by NASA-sponsored contractors and grantees.
- **CONFERENCE PUBLICATION.** Collected papers from scientific and technical conferences, symposia, seminars, or other meetings sponsored or cosponsored by NASA.
- **SPECIAL PUBLICATION.** Scientific, technical, or historical information from NASA programs, projects, and missions, often concerned with subjects having substantial public interest.
- **TECHNICAL TRANSLATION.** English-language translations of foreign scientific and technical material pertinent to NASA's mission.

Specialized services that complement the STI Program Office's diverse offerings include creating custom thesauri, building customized databases, organizing and publishing research results ...even providing videos.

For more information about the NASA STI Program Office, see the following:

- Access the NASA STI Program Home Page at:
<http://www.sti.nasa.gov>
- E-mail your question via the Internet to:
help@sti.nasa.gov
- Fax your question to NASA Access Help Desk at:
(301) 621-0134
- Telephone the NASA Access Help Desk at
(301) 621-0390
- Write to:
NASA Access Help Desk
NASA Center for AeroSpace Information
7121 Standard Drive
Hanover, MD 21076-1320



A Model Rotor in Axial Flight

K. W. McAlister and S. S. Huang
Army/NASA Rotorcraft Division
Aeroflightdynamics Directorate (AMRDEC)
US Army Aviation and Missile Command
Ames Research Center, Moffett Field, CA

A. I. Abrego
Army/NASA Rotorcraft Division
Aeromechanics Branch
NASA Ames Research Center, Moffett Field, CA

National Aeronautics and
Space Administration

Ames Research Center
Moffett Field, California 94035-1000

Available from:

NASA Center for AeroSpace Information
7121 Standard Drive
Hanover, MD 21076-1320
(301) 621-0390

National Technical Information Service
5285 Port Royal Road
Springfield, VA 22161
(703) 487-4650

A Model Rotor in Axial Flight

K. W. McAlister, S. S. Huang, and A. I. Abrego

Army/NASA Rotorcraft Division

Ames Research Center, Moffett Field, CA

ABSTRACT

A model rotor was mounted horizontally in the settling chamber of a wind tunnel to obtain performance and wake structure data under low climb conditions. The immediate wake of the rotor ($\psi \leq 31^\circ$) was carefully surveyed using 3-component particle image velocimetry to define the velocity and vortical content of the flow, and the data used in a subsequent study to validate a theory for the separate determination of induced and profile drag. Measurements were obtained for two collective pitch angles intended to render a predominately induced drag state and another with a marked increase in profile drag. A majority of the azimuthally directed vorticity in the wake was found to be concentrated in the tip vortices. However, adjacent layers of inboard vorticity with opposite sense were clearly present. At low collective, the close proximity of the tip vortex from the previous blade caused the wake from the most recent blade passage to be distorted. The deficit velocity component that was directed along the azimuth of the rotor blade was never more than 15% of the rotor tip speed, and except for the region of the tip vortex, appeared to have totally disappeared from the wake left by the previous blade.

NOMENCLATURE

a	speed of sound, m/s
A	area of rotor disk, m^2
c	chord, m
C_Q	torque coefficient, $\text{torque}/\rho\pi\Omega^2 R^5$
C_T	thrust coefficient, $\text{thrust}/\rho\pi\Omega^2 R^4$
FM	hover induced power/actual power
M	hover tip Mach number, $R\Omega/a$
Q	rotor torque, N-m
r	radial distance from vortex center, mm
r_c	vortex core radius, mm
R	radius of rotor, m
Re	hover tip Reynolds number, $cR\Omega/\nu$
T	rotor thrust, N
u	radial velocity component, m/s
v	azimuthal velocity component, m/s

w	axial velocity component, m/s
V_∞	velocity upstream of rotor, m/s
V_{tip}	velocity of rotor tip, ΩR , m/s
θ	rotor collective pitch angle, deg
ν	kinematic viscosity, m^2/s
ρ	air density, N/m^3
σ	rotor solidity, blade area/disk area
ψ	azimuthal distance from blade, deg
ω_θ	vorticity normal to r - z plane, $1/s$
Ω	angular velocity of rotor blade, rad/s

INTRODUCTION

The performance of a helicopter rotor blade is influenced by two types of drag: induced and profile. Induced drag is primarily related to the concentrated vortex that trails from the tip of the rotor blade. Profile drag is related to the chordwise-directed viscous forces that develop on the surface of the blade which give rise to both positive and negative layers of vorticity oriented along the span. Neither of these drag components can exist without viscosity. Induced and profile drag forces, which combine to produce the torque that the helicopter must overcome, can be reduced by cleverly tailoring the shape (profile, twist, planform, etc) of the blade. To facilitate this endeavor, it is important to distinguish between these two sources of drag. Since neither drag component can be measured directly, a theory was developed for separately determining the value of the induced and profile drag components by examining the velocity and vortical content of the flow in the wake immediately behind the rotor blade (ref. 1). The evidence needed is believed to be present within the first few chord lengths behind the blade, after which viscous diffusion causes the layers of spanwise vorticity to undergo self annihilation. The purpose of this experiment was to gather the data needed to validate this theory. This paper describes the test facility, model, flow measurement technique, and data acquisition and processing. A discussion of the results is provided along with specific findings.

TEST DESCRIPTION

Test Facility- This experiment was performed in the settling chamber of the 7- by 10-Foot Wind Tunnel at Ames Research Center (fig. 1). The maximum speed that could be obtained in this section of the tunnel circuit was about 18 m/s. Screens that are located upstream of the settling chamber rendered the flow approaching the rotor with estimated turbulence levels below 1.2%.

A model rotor was placed in the center of the settling chamber and mounted horizontally with its axis of rotation coincident with the centerline of the test section. Aside from the influence of the tunnel walls (approximately 15 feet away) and the contraction into the test section (with an area ratio of 13.3:1), the rotor wake was allowed to pass through the test section without interference. To simulate a hover state, a curtain was drawn across the heat-exchanger section to prevent the wake from recirculating around the tunnel and creating an unwanted climb condition. In this configuration, any portion of the wake reaching this section would be expelled through the heat-exchanger doors and fresh stagnant air would be drawn by the rotor as required into the tunnel circuit. To simulate a climb condition, the curtain was removed and the tunnel fan was operated in a manner similar to an earlier experiment (ref. 2). That is, the upstream velocity was a combination of flows generated by both the rotor and the tunnel fan.

Video cameras were mounted upstream and to the side of the rotor to monitor critical elements during the test (fig. 2). It is customary to infer the velocity in the test section from the differential pressure between the settling chamber and the test section. However, this procedure does not reveal the nonuniform character of the flow across the test section and, at low speeds, is not sufficiently accurate. Therefore, the velocity in the test section was measured with a vane anemometer (1 to 130 ft/s range) attached to an existing tunnel traverse. In the settling chamber, where the velocity was considerably lower, a hot-film probe was used to measure velocity (0 to 8 ft/s range) directly upstream of the rotor at a distance of about 28 feet from the tip-path plane. A flow seeder was placed sufficiently far upstream to minimize any disturbance to the flow approaching the rotor and to allow enough time for the particles to spread uniformly over the near-wake region of the rotor to be studied.

Model Rotor- The model used in this experiment was a 1/7-scale of the AH-1/OLS rotor. The profile of this blade was based on a simple trailing-edge extension to the shape of a NACA 0012 airfoil (fig. 3). The rotor consisted of two blades, each with a chord of 4.09 inches and a span of 37.7 inches measured from the axis of rotation to the blade tip (fig.

4). Beginning at 25% radius, the twist of each blade was $-0.27^\circ/\text{inch}$, so that the total variation in geometric twist along the span was 7.55° . Collective pitch settings were referenced to the geometric pitch angle at 75% radius. Therefore, a collective pitch setting of zero meant that the blade pitch was about 5.00° at the root (held fixed for locations less than $R/4$) and -2.50° at the tip. The rotor hub had a built-in blade precone of 1.30° .

Information related to safety-of-flight was obtained by flap- and chord-bending gages mounted on the blade. The drag link used to adjust the blade sweep was instrumented with a strain gage that responded to the aerodynamic drag on the rotor, and as such, offered a redundant measurement of chord-wise bending. Depending on the sweep of the blade and the location of the center of mass of the blade, this gage could also be loaded by a centrifugal force induced moment. Strain gages were placed on the pitch horns that transmitted commands to the rotor blades. Reactions to these commands resulted in bending loads on these elements that were proportional to the torsional moments on the blades. A transducer for measuring the angular tilt of the rotor (called the teeter pot) was mounted on top of the hub. The rotor operator monitored the signals from each of these gages. Since the center of mass of each rotor blade was located aft of the feathering axis (aligned with the quarter chord), it was necessary to sweep the blades forward 1.20° to minimize steady chord-wise bending due to centripetal force. The blades were strobed at 2/rev to verify that the blades were tracking. A blade sweep of 1.20° corresponded to a 0.19c movement of the tip.

The model rotor was attached to a teetering hub, which in turn was mounted on the VSB-54 force and moment balance. The most significant element of the balance in the present test was the axial gage, which had a capacity of 350 lbs and provided a measure of the rotor thrust. Rotor torque was measured using torsion gages mounted on a flex coupling located between the balance and the transmission, and had a capacity of 54 ft-lbs. The rotor was driven by a 90 HP electric motor through a 4:1 transmission. The complete rotor and drive system (fig. 5) was supported on a tripod-like structure that was rigidly attached to the frame of the wind tunnel. This setup placed the tip-path plane of the rotor about 6 feet upstream of the beginning of the contraction section of the tunnel, well within the protective steel-wall section of the tunnel.

Performance Data- The primary variables needed to establish the performance of the rotor are given in table 3. This data was sampled at 10 Hz and then averaged over a minimum period of 10 seconds.

Some cases were averaged over an extended period of time, sometimes as long as 30 minutes, to resolve equilibrium issues. All safety-of-flight data were sampled and digitally recorded at a rate of over 100,000 samples/s and displayed at 1-second intervals on a monitor.

The central region of the flow sampled with the vane anemometer at intervals of about 8 inches in the horizontal direction and 9 inches in the vertical direction. This matrix of measurements covered about 36% of the cross section. The matrix was extended in both directions in a few cases to ascertain the value of surveying an additional 37% of the test section area.

Table 1: Rotor Performance Variables

Collective pitch angle
Rotor thrust
Rotor torque
Air temperature
Settling chamber velocity
Test section velocity

Stereoscopic PIV Method- The velocity of a fluid can be inferred from the motion of discrete particles that are suspended in the flow. This method is known as particle image velocimetry (PIV). A single thin sheet of light is normally used to define the plane of interest. The particle images that are recorded at two different times are then cross-correlated to yield displacement vectors (magnitude and direction). The time interval between the two images must be short enough so that the particles remain in the light sheet, yet long enough so that the particle displacements are perceptible. It is assumed that the particles are small enough to accurately track the flow.

A single camera placed normal to the sheet of light provides the images that are needed to produce a two-dimensional array of velocity vectors. If the flow has a significant third component (directed normal to the plane of the light sheet), an error due to perspective develops in the two-dimensional array that is zero in the center and increases toward the image boundaries. This seemingly undesirable sensitivity to out-of-plane motion was later exploited to derive the third component of velocity (ref. 3). In fact, sensitivity to the out-of-plane component of velocity over the entire image plane can be increased by intentionally placing the camera at an oblique angle to the light sheet. To uniquely determine a three-dimensional particle displacement requires two cameras that are oblique to the light sheet, each offering a different perspective of the particle motion between the two exposures (fig. 6). This procedure is known as Stereoscopic PIV or 3D-PIV.

The technique demands both critical focus and maximum brightness of the particle image. Conventional lens mounts create a plane of focus in object space that is parallel with both the image plane and the lens plane. When the lens plane is oblique to the object plane (as is the case for Stereoscopic PIV), particles will be increasingly defocused as their distance from the centerline of the object plane increases. The conventional corrective action would be to increase the depth of field by reducing the aperture of the lens. Unfortunately, reducing the lens aperture drastically reduces both the particle image intensity and the image resolution. The problem is solved with Scheimpflug focusing (refs. 4 and 5). To keep the object plane in focus when the lens plane is rotated to an oblique orientation, the image plane (where the camera sensor is placed) must also be rotated such that all three planes (object, lens, and image) intersect along a common line.

Arrangement of PIV Equipment- Elements of a basic Stereo PIV system normally consist of a pulsed laser, optics to spread the beam into a thin sheet, CCD cameras to record the images, and a calibration target. Due to numerous physical constraints in this test, the blade was considered to be at zero azimuth when the trailing edge was horizontal. Interest in the near wake behind the rotor therefore required that the plane of the light sheet be horizontal as well, and that it should skim the trailing edge of the rotor (fig. 7). In order for both cameras to be in a forward scatter position, two opposing, coplanar light sheets were needed. To avoid interference with the model supports, the cameras were at different distances away from the light sheet (nominally 5 feet) and at different angles. The relatively low power of the Nd:YAG lasers that were available (120 mJ) meant that two such lasers would have to be synchronized. A 1/rev reference signal was obtained by directing a small continuous-wave laser beam onto a small mirror attached to the hub of the rotor and intercepting the reflected beam with a fast-response photo detector.

Camera Specifications- Images were acquired with 8-bit charged-coupled device (CCD), cross-correlation cameras having a sensor array of $2K \times 2K$ pixels (nominal). Each pixel measured $7.4 \mu m$ on a side. The cameras were operated in a double-exposure mode to acquire two non-interlaced, full-frame images in a single frame interval. The time interval between images was variable between $2 \mu s$ and 30 ms. These are non-standard video cameras that could be externally triggered and driven at any frequency up to 15 Hz in double-exposure mode. A computer interface provided control over gain, contrast, black level, and trigger mode. Because the cameras were located at

different distances from the object plane, one used a 55-mm lens while the other used an 85-mm lens. The lenses were remotely translated to focus on the centerline of the image area and the sensor (located inside the camera body) was rotated about its centerline to satisfy the Scheimpflug condition.

Laser and Sheet Optics- A Nd:YAG laser was frequency doubled to provide a beam having a wavelength of 532 nm, a pulse width of about 4 ns, and power of 120 mJ. The laser beam had a diameter of about 5 mm and a divergence of 0.60 mrad. In this test the laser-light sheet was formed by first passing the beam through a set of spherical lenses (consisting of -500 mm and +500 mm). By adjusting the distance between these two lenses, the beam waist (approximately 1-mm thick) could be positioned in the region imaged by the cameras. Two cylindrical lenses (-12.7 mm and +25.4 mm) were used to expand the beam in the horizontal direction. The distance between the sheet forming optics and the imaged area was about 5 feet.

System Alignment- The lasers, sheet-forming optics, and cameras were mounted on a common structure, which could be traversed in 3 orthogonal directions. A 6- by 9-inch rectangle was milled into the surface of a flat aluminum plate and used as the calibration target. The calibration plate was leveled and the light sheets adjusted so as to evenly graze the surface. The lens of each camera was traversed along its optical axis and the CCD sensors rotated until a uniform focus on the calibration target was achieved. After recording the calibration images, the structure supporting the entire optical system was elevated and translated to match the wake region of interest.

PIV Software- This experiment was performed using ProVision software developed by Integrated Design Tools (IDT). This software controlled both data acquisition and the image-processing interface. This dual role had the advantage of providing a fully integrated calibration procedure that allowed for acquisition, quality assurance and data reduction. The calibration yielded all the optical parameters required for the accurate reconstruction of three-component velocity-vector fields.

Images were processed by first covering the region of interest with an interrogation grid. The intersections of the vertical and horizontal grid lines defined the centers of each interrogation window. The interrogation window was the smaller region in the reference and delayed images that were cross-correlated using an optimized Fourier transform. When the camera calibrations were applied, the grid in each camera view covered the exact same area in the flow field.

The size of the interrogation window was based

on the particle density and the maximum instantaneous displacement of the particles. Typically, window sizes range from 8 to 64 pixels on a side and each interrogation window yields one vector. The cross-correlation of the interrogation window in the reference image with that of the delayed image yields a correlation map. The location of the correlation peak in space determines the local displacement in both magnitude and direction.

ProVision incorporates quality-assurance tests in the vector calculations. The processing begins with a first-pass correlation between the reference image and delayed image to determine the maximum displacement range. For the second pass the software enlarges the interrogation area in the delayed image. The amount of the enlargement is based on the maximum displacement range determined in the first pass. Since the Fourier transform requires both interrogation areas to be identical, the software "adds zeros" to the interrogation area of the reference image to match the size of the delayed image area. This technique maximizes the probability of correlating all the particles found in the reference image interrogation area to those found in the delayed image, thereby maximizing the statistical accuracy.

The software then counts the number of particle images (each composed of several contiguous pixels) in the interrogation window. Ten particle pairs are required to contribute to a correlation map. The centroid of each particle is calculated, thus yielding sub-pixel accuracy of their position. A second-order curve fit is determined from the ten displacements. This curve fit yields a single vector, at the precise grid point location, whose error is reduced by a factor of 0.3 ($1/\sqrt{N}$, where $N = 10$ particles) over the straight fast Fourier transform (FFT) of the same area (ref. 6).

If there are not enough particles in a given interrogation region, the program will automatically enlarge the interrogation area of the reference image. If there are ten or more particles in this enlarged area, then the correlation proceeds in the same manner described above. The data for this grid point is considered to be a recalculation. If ten particles are not counted, the software will expand the interrogation area incrementally. It will repeat this process until the interrogation area expands to a limit of 64x64 pixels. If the ten-particle threshold is not met for the largest area, then velocity values are interpolated for that grid point using a second-order curve fit based on nearest-neighbor values. This vector is also counted as a recalculation. The software tracks the number of these recalculations and displays that number after each camera view is processed. If the number of recalculations is less than 1% of the total vectors, then

the data are considered reliable.

Particle Seeding- Proper seeding of the flow is critical to accurate PIV measurements. The seed particles must be evenly distributed and of sufficient density to define the flow without altering its physical properties. The particles must also be small enough that they accurately follow the flow (especially challenging in accelerating flows), yet large enough so that they scatter a sufficient amount of light to be detected. It is usually convenient to have remote control over the delivery of the seed material into the flow. The particle generator used in this test employed an inert gas to atomize a non-toxic, pharmaceutical-grade mineral oil. The mist was vaporized and then condensed before being released into the flow. The particle size was estimated to be less than $0.5\ \mu\text{m}$. The particle generator was located upstream of the settling chamber so that the particles would mix with the air entering the tunnel circuit before being drawn into the wake of the rotor.

PIV Data Acquisition- The CCD cameras were connected to separate frame-grabber cards installed in a PC workstation. Using ProVision software, images were acquired and selectively processed immediately in order to evaluate the quality of the raw images and the adequacy of the inter-pulse time delay. Good image correlations depend on such issues as background light contamination, particle image brightness, contrast, focus, beam alignment, and light pulse separation.

Prior to taking data, fine beam focusing and alignment were performed. Focusing was accomplished by translating the camera lenses while observing the real-time image displays. The gain and black levels were adjusted to maximize the contrast and brightness of the particle images. The laser sheets were judged to be coplanar when both laser pulses were recorded as a single image and the resulting particle images appeared as doublets.

The correct inter-pulse delay can best be determined under actual test conditions. Images were acquired and correlated to determine the maximum particle displacement. This displacement corresponded to the maximum particle velocity and the pulse separation was adjusted to produce a ± 3 pixel range, regardless of the window size. Pixel displacements that are too small will limit the dynamic range whereas displacements that are too large will decrease the probability of correlation (ref. 7). Because of the high in-plane particle displacements, caused by the high circumferential velocity of the trailing vortex from the rotor at different wake ages, the optimum pulse separations varied from 5 to $40\ \mu\text{s}$ (tables 4 and 5). It should be noted that if the thickness of the light sheet is 1 mm and the tip of the rotor blade is moving at

87 m/s, the time delay between laser pulses should be no more than about $12\ \mu\text{s}$ to capture the highest out-of-plane velocities just behind the rotor. If this condition is not satisfied at a calculation node, an interpolated value based on values at neighboring nodes results. Once image quality was assured, 25 image pairs were acquired per wake age. Data for each wake age required about 400 megabytes of storage.

Table 2: Pulse Delay Times when $\theta = 5^\circ$

Wake Age	Zone A	Zone B	Zone C
0.50 c	$15\ \mu\text{s}$	$20\ \mu\text{s}$	$12\ \mu\text{s}$
1.00 c	$15\ \mu\text{s}$	$20\ \mu\text{s}$	$20\ \mu\text{s}$
2.00 c	$15\ \mu\text{s}$	$20\ \mu\text{s}$	$30\ \mu\text{s}$
3.00 c	$15\ \mu\text{s}$	$20\ \mu\text{s}$	$40\ \mu\text{s}$
4.00 c	$15\ \mu\text{s}$	$20\ \mu\text{s}$	$40\ \mu\text{s}$
5.00 c	$15\ \mu\text{s}$	$20\ \mu\text{s}$	$40\ \mu\text{s}$

Table 3: Pulse Delay Times when $\theta = 11^\circ$

Wake Age	Zone A	Zone B	Zone C
0.50 c	$5\ \mu\text{s}$	$5\ \mu\text{s}$	$12\ \mu\text{s}$
1.00 c	$5\ \mu\text{s}$	$5\ \mu\text{s}$	$12\ \mu\text{s}$
2.00 c	$5\ \mu\text{s}$	$5\ \mu\text{s}$	$20\ \mu\text{s}$
3.00 c	$5\ \mu\text{s}$	$5\ \mu\text{s}$	$25\ \mu\text{s}$
4.00 c	$5\ \mu\text{s}$	$5\ \mu\text{s}$	$30\ \mu\text{s}$
5.00 c	$5\ \mu\text{s}$	$5\ \mu\text{s}$	$40\ \mu\text{s}$

Processing Wake Images- After completion of the test, the data were processed on a PC workstation using ProVision software. To obtain good resolution of the primary vortex, a calculation mesh having 101 nodes by 78 nodes was constructed over the region of significant interest in the flow field. The area covered by the mesh resulted in approximately 17 pixels between nodes in both directions. The interrogation window was set at 24 pixels on a side, which gave a 70% overlap. The physical area measured in each image zone was 262 mm (with an axial increment of 2.6 mm) by 149 mm (with a radial increment of 1.9 mm). The 2.6 mm by 1.9 mm increments, which defined the calculation step sizes in the axial and radial directions, also defined the resolution of the measurements.

A single file for each wake age included a flag for every velocity measurement that indicated the nature of that vector (such as valid, invalid, interpolated, recalculated, or not calculated). Reduced data files containing the coordinates of each calculation node and the three components of velocity (in

terms of displacement) were stored in ASCII format and then transferred to a mainframe computer for analysis.

The velocity components were first converted from displacement units to velocity units based on the pulse duration for that particular measurement. The physical coordinates were transformed so that $r = z = 0$ would correspond to the center of the rotor hub (fig. 7). The sequence for extracting the characteristics of the trailing vortex (fig. 8) for each case began with a calculation of the vorticity field, ω_θ , for every image pair. Vorticity was calculated by integration (circulation box method) according to:

$$\omega_\theta = A^{-1}\Gamma = A^{-1} \oint (\vec{u}, \vec{w}) \cdot d(\vec{r}, \vec{z}) \quad (1)$$

where the direction of integration was such that the enclosed area, A , was on the left of the integration path. The size of each circulation box was defined by the local mesh spacing, which on average rendered $A = 5 \text{ mm}^2$.

When more than one vorticity center was present in the field of view, a single image pair had to be processed to determine where the field should be partitioned so that statistics could be built on only one vortex. A simple circular partition that focused on the vortex of interest was usually sufficient to separate the two vortices.

After calculating the vorticity distribution over the entire image, a search was performed to discover the zone of greatest vorticity concentration based on values exceeding 50% of the maximum. The center of vorticity for a given image was defined to be at the average of these selected locations. The 50% threshold criterion prevented the center of vorticity for an image from being influenced by a single, and possibly erroneous, measurement of velocity (which in turn contributes to the calculation of vorticity). The resulting centers of vorticity (one for each image) formed a set for which the mean value and the standard deviation could be calculated. Normally any image with a vortex center that deviated from the mean by more than 1.5 times the standard deviation would be purged from the set. Since the flow in the near wake was exceptionally periodic in this experiment, the resulting standard deviation was small enough that all images were eligible for inclusion in the average. The standard deviation criterion prevents an atypical departure, albeit a legitimate image, from being factored into the average. The threshold and purging criteria both have the affect of reducing the degree of wander in the data.

The images must be averaged to smooth out small irregularities in the flow. However, whenever

there are features in the flow with high gradients, such as a trailing vortex, and the vortex appears in different positions from image to image (vortex wander), important details of the structure tend to be smeared out if a simple average of the images is performed. The remedy was to perform the average after artificially aligning the images based on a recurring feature of the flow, which in this case was the center of vorticity. This process, in contrast to a simple average, is referred to as conditional ensemble averaging; the condition here being the alignment of all the images in the set based on their centers of vorticity. The image with a vortex center closest to the mean location that was established for the set of images was selected as the "anchor". The indices of each image matrix were then adjusted according to the offset of each vortex center from the vortex center in the anchor image. All data in the anchor image were retained. However, some portion of all other images with adjusted indices that fall outside the boundaries of the anchored image were necessarily discarded. Hence, as a consequence of vortex wander, the population contributing to the conditional average was greatest over the interior of the matrix.

To extract information about the geometry of the vortex (see ref. 8 for more detail), the center of the vortex was assumed to be at the center of swirl (which was not necessarily at the center of the vorticity that was accreted from the rotor wake, which had the form of a spiraling sheet with varying vorticity). Using the center of vorticity as a starting point, the surrounding locations were interrogated to determine the best node for which the sum of the dot products of two unit vectors was a minimum over a neighborhood of locations surrounding the candidate node. The coordinates of the neighboring node relative to the candidate node defined one of the unit vectors. The velocity vector at the neighboring node defined the other unit vector. Denoting the angles of these two unit vectors by α and β (fig. 9), then the node nearest the center of swirl was found when the following expression was a minimum:

$$\sum_{n=1}^N |\cos(\alpha - \beta)| / N \quad (2)$$

where N is the total number of neighboring points considered. Relative to the center of swirl for a pure vortex in a stationary flow, α and β will be orthogonal for all neighboring points and the sum will be exactly zero. For most real flows the sum will not be precisely zero, and the procedure works best when the neighborhood under consideration does not extend beyond about one or two core diameters (which is normally sufficient to cover a majority of the vorticity in a sin-

gle trailing vortex).

After locating the center of swirl, the size of the vortex core can be found by dividing the surrounding region into annular zones and calculating the average swirl velocity and the associated mean radius of each annulus. This data can then be fit with a least-squares spline subject to the condition that the resulting curve have only one inflection along its inner extent (nominally set to twice the estimated core radius that was previously found). The point of inflection now defines the radius of the vortex core, since that is where a maximum value for the swirl velocity is reached. This procedure was considered to offer a more rational approach for determining the size of the vortex, especially when the velocity peaks that are characteristic of vortices (and upon which core sizes are traditionally based) are dependent on how the vortex is sliced (vertical, horizontal, or otherwise).

Test Conditions- The experiment was performed at a constant rotor speed of 870 RPM (14.5 Hz), which for a rotor diameter of 75.4 inches corresponds to a tip speed of 286.2 ft/s. Based on an average ambient temperature of 62° F, the Reynolds number based on tip chord was $Re = 0.6 \times 10^6$ and the Mach number was $M = 0.26$. The collective pitch angle and the rate of climb were the only variables in this test (table 1). The lowest climb condition was intended to occur when the return flow was not blocked and the fan was idle. This is referred to as the "normal tunnel" configuration, with the rotor itself substituting for the tunnel fan to establish a modest flow around the tunnel circuit.

As indicated in table 1, wake measurements were performed only for collective pitch angles of 5° and 11°. In order to obtain high resolution PIV images, the cameras were focused on a small region in the near wake behind the trailing edge of the rotor. To expand the physical area under study the camera view was radially translated over a total of 3 contiguous regions, giving a total coverage of the outer 56% of the rotor blade. Measurements at different wake ages were obtained by adjusting the timing of the pulsed light sheets, thereby permitting the tip of the rotor blade to incrementally pass beyond the plane of the light sheets by up to 5 chord lengths. The PIV measurement locations are shown in table 2.

RESULTS AND DISCUSSION

Equilibrium Conditions- Given that it takes a certain amount of time for the flow in the tunnel to adjust to the action of the rotor and to reach equilibrium (during which time balance zeros may drift due to heating), time histories of the rotor loads and the tunnel velocity were recorded (fig. 10). The results indicate that the velocity in the test section and the rotor

Table 4: Test Conditions

Configuration	Collective Pitch Angle				
	3°	5°	7°	9°	11°
Tunnel Blocked	✓	*	✓	✓	*
Normal Tunnel	✓	✓	✓	✓	✓
Climb, fan @ 22 RPM	✓	✓	✓	✓	✓
Climb, fan @ 52 RPM	✓	✓	✓	✓	✓
Climb, fan @ 80 RPM	✓	✓	✓	✓	✓
Climb, fan @ 105 RPM	✓	✓	✓	✓	✓

* including PIV wake measurements

Table 5: Location of PIV Measurements

Wake Age	Zone A	Zone B	Zone C
0.50 c	✓	✓	✓
1.00 c	✓	✓	✓
2.00 c	✓	✓	✓
3.00 c	✓	✓	✓
4.00 c	✓	✓	✓
5.00 c	✓	✓	✓

torque reached acceptably level values within 5 minutes. However, the thrust (which was measured with a 6-component balance) asymptotically approached a steady value over a period of about 20 minutes. This suggests that the air in the tunnel circuit was set into motion rather quickly and that the continued change in thrust was due to balance heating.

Since the balance appears to be considerably more sensitive to temperature at low thrust levels, it is clear that a pre-run tare reading will not be useful. To evaluate the suitability of a post-run zero, time histories of the thrust and torque were recorded during successive start ups and shut downs of the rotor (fig. 11). Using arbitrary references, the buildup and decay in thrust readings are distinctly different from the torque readings. After a shutdown was initiated, the rotor quickly came to rest while the flow in the settling chamber (where the rotor was located) became essentially zero after one minute. During that brief one-minute time interval the diminishing impact of the air stagnating on the blades appears to be somewhat offset by the temperature drift of the balance. Although not ideal, the thrust and torque readings at one minute after shutdown were taken to be the correct tare values.

Rotor Performance- The wake of the rotor was free to locally recirculate and become reingested by the rotor, while the remainder of the wake passed downstream and through the test section. As depicted in the upper contour plot (fig. 12), the flow

in the test section was not only nonuniform, but favored one side. The skewing of the flow toward one side is believed to be due to the blockage effect of the PIV support structure on the opposite side of the tunnel, which restricted the amount of air flowing near the walls of the settling chamber as it was being entrained by the rotor wake and drawn into the test section. Adding an additional 37% to the area surveyed (lower contour plot) yielded only a negligible change in the averaged velocity.

With the return flow blocked, rotor loads were measured for collective angles 3° to 11° (fig. 13). The subplot showing the variation in test section velocity with collective pitch angle shows that the single measurement at the centerline of the tunnel reasonably approximates the value obtained by averaging over the central portion of the test section. Using these values to represent the flow through the test section, conservation of mass and the known area ratio dictate the velocity that must exist upstream of the rotor. These deduced values agree well with the velocities that were measured upstream of the rotor (about 4.5 rotor diameters). Based on thrust and torque measurements, the calculated hover figure-of-merit (FM) is also shown for the range of collective pitch angles.

$$FM = (T^3/2\rho A)^{1/2}/Q\Omega \quad (3)$$

It should be noted that the above relation assumes that the flow is unbounded and that the far upstream velocity is zero. Although these assumptions were violated in this experimental setup, especially when the tunnel fan was used to create a climb condition, the hover figure-of-merit will simply serve as a convenient nondimensional group for comparison purposes.

With the tunnel circuit in its normal configuration (return flow unblocked), that portion of the rotor wake that is not skimmed off near the walls of the heat exchanger section will continue around the tunnel. That means that the rotor had to be drawing stagnant air from outside the facility and mixing it with a portion of the wake that the rotor had already generated. In essence, even with the tunnel fan at 0 RPM, the rotor was in a slight climb condition. With all other parameters remaining the same, the resulting rotor loads were slightly lower (fig. 14). The measured velocity approaching the rotor was perceptively higher, a condition that was made more evident in the "amplified" flow that developed in the test section.

Running the tunnel fan at speeds from 22 to 105 RPM increased the upstream velocity until it completely dominated the contribution of the rotor to the recirculating flow in the tunnel circuit. The load variation with collective pitch angle retained the same shape (figs. 15-18), however the loads decreased with

increasing "climb rate" due to an effective reduction in the blade incidence (fig. 19). The climb velocity is defined as the relative motion of the rotor disk to free air. Since the tunnel walls bound the rotor, the upstream velocity was not entirely the climb velocity. However, for simplicity, the climb rate in this paper is taken to mean V_∞/V_{tip} , where V_∞ refers to the upstream velocity and $V_{tip} = R\Omega$.

It would appear that a good estimate for the hover figure of merit can be obtained by extrapolating the curve for any given collective pitch back to $V_\infty/V_{tip} = 0$ (as suggested in ref. 2). Although the placement of the rotor in the settling chamber of the wind tunnel did result in a smoother flow than would normally be achieved in the Hover Test Facility at Ames Research Center (a comparatively small cubic space with an asymmetric flow intake), the confining boundaries of the wind tunnel do affect the flow and may prevent the simulation of a true hover condition, even with the return flow blocked. When the return flow in the tunnel is blocked and the rotor wake that passes through the test section is totally expelled, continuity requires that a flow upstream of the rotor must exist, and this contradicts the ideal hover state. Given that an upstream flow did exist in this experiment, it is difficult to imagine how this flow could have passed through the rotor entirely, and not have at least a portion of the flow travel around the rotor. By considering the case when the return flow was blocked, one can show that a portion of the flow did indeed bypass the rotor. If the rotor were to have been operating in free air, it can be shown from momentum theory that:

$$V_a = \left(\frac{T}{2\rho A} \right)^{1/2} \quad (4)$$

where V_a represents the flow through the rotor disk, and A represents the area of the disk (31 ft^2). For $\theta = 11^\circ$ the thrust is about 40 lb_f . The volume flow rate through the rotor disk is $AV_a = 505 \text{ ft}^3/\text{s}$. However, based on the averaged velocity measured across the test section, the volume flow rate passing through the tunnel is $1444 \text{ ft}^3/\text{s}$, which is about 3 times higher than the volume passing through the disk. This implies that the rotor had set into motion a great deal more fluid upstream of the rotor than actually passed through the rotor disk, and places some degree of uncertainty on just what flow state can be ascribed to this experimental setup.

As the wake of the rotor (along with the surrounding air that had been entrained) passed through the tunnel contraction, the entire flow was accelerated and the static pressure decreased. This difference in pressure between the test section and the settling chamber must have lead to the development of an up-

stream velocity that appeared to the rotor as a climb velocity. This unintentional climb velocity could have been forced to zero by restricting (or blocking) the flow through the test section, but then the rotor would have been operating in a "ground effect" state. A better solution may be to eliminate this pressure differential by exposing the test section to atmospheric pressure, although the tunnel contraction boundaries would undoubtedly still have some influence on the flow. A numerical analysis was performed on a rotor in free air as well as with straight wall and tunnel contraction boundaries (ref. 8). These results indicate that the tunnel walls do indeed have an effect on the flow and that the correct hover figure of merit (which was shown to be higher) can only be obtained in free air.

Rotor Wake- The following discussion of the rotor wake will initially focus on the tip region of the flow (zone A) over progressively larger wake ages (from $\psi = 3^\circ$ to 31°). Each series, first for $\theta = 5^\circ$ and then for $\theta = 11^\circ$, will consist of two parts: (a) the location and size of the vortex and (b) contour maps of the velocity and vorticity fields.

Statistics on the location and size of the vortex (part (a) of each figure) includes a graphic showing the degree of wander for the set of images (for example, fig. 20). The grid spacing of $\Delta r = 1.9$ mm and $\Delta z = 2.6$ mm corresponds to the calculation mesh used to determine the velocity field. The vorticity field is shown as a color contour map. The magnitude of the vorticity is represented by the level of color saturation, with a blue hue denoting $\omega_\theta < 0$ and a red hue denoting $\omega_\theta > 0$. Along with the position of the rotor tip, the location of the vorticity center (defined at the centroid of vorticity values exceeding 50% of the maximum) is also shown. The inplane velocity is shown as colored vectors with the hue ranging from blue (zero velocity) to red (maximum velocity). The location of the center of swirl (as defined earlier) is also shown. The circled area identifies the range of swirl vectors used to construct the swirl velocity fit, which in turn defines the peak swirl velocity and the size of the vortex core.

The velocity and vorticity contours (part b of each figure), which include a superposition of contour lines, more clearly emphasize the relationship between the tip vortices and the remainder of the rotor wake. Only blue and red hues are used, with the magnitude of the variable indicated by the saturation of the two colors. Maximum and minimum values of each variable are shown along side of the respective color bars.

The results for $\theta = 5^\circ$ (figs. 20 - 25) show that the vortex wandered by an average of 0.65 mm, which is about 8% of the core radius. The vortex from the second blade ($\psi = 180^\circ$ earlier) accompanied the vor-

tex from the first blade in all zone-A images. The inboard portion of the wake that is associated with the first vortex appears to be distorted by the close proximity of the second vortex at all wake ages studied (up to $\psi = 31^\circ$). Aside from the tip vortex, the wake from the second blade cannot be detected. The difference in the locations of the vorticity center and the swirl center averages about 2 to 3 mm, or about 32% of the core radius. The viscous wake along the span of the first rotor blade is clearly evident in the strong out-of-plane velocity component (v), which shows a noticeable disconnect in magnitude just as it approaches the tip vortex.

The results for $\theta = 11^\circ$ (figs. 26 - 31) show that the vortex wandered by an average of 0.54 mm, which is less than in the $\theta = 5^\circ$ case, yet is about 9% of the core radius that occurred at this higher collective angle. The axial separation between the vortices from the first and second blades has substantially increased. Although the axial position of the viscous wake from the first blade has also increased, the distance between this wake and the second vortex is now sufficient (compared to the $\theta = 5^\circ$ case) that no distortion of the wake appears to be present. Aside from the tip vortex, the wake from the second blade cannot be detected (similar to the $\theta = 5^\circ$ case). The difference in the locations of the vorticity center and the swirl center averages little more than 1 mm, or about 21% of the core radius. The out-of-plane velocity component continues to show a disconnect between the flow in the tip vortex and the remainder of the viscous wake.

The data does not support any obvious trend in either the size or intensity of the vortex during the first 31° of wake age (fig. 32). On average, $r_c = 7.7$ mm (7.4% of c) when $\theta = 5^\circ$ and decreases to $r_c = 6.3$ mm (6.1% of c) when $\theta = 11^\circ$. The maximum swirl velocity averages 7.4 m/s (8.5% of $R\Omega$) when $\theta = 5^\circ$ and increases to 29 m/s (33% of $R\Omega$) when $\theta = 11^\circ$. The radial location of the tip vortex decreases rapidly with wake age, traveling in a linear fashion at about 0.5 mm per degree of wake age (totaling 1.5% of R) when $\theta = 5^\circ$ and nearly double this amount when $\theta = 11^\circ$. The axial location of the tip vortex is more difficult to summarize. In the $\theta = 5^\circ$ case, the tip vortex appears to suddenly jump in elevation after $\psi = 10^\circ$ and remain at this level. On the other hand, in the $\theta = 11^\circ$ case, the tip vortex travels in an increasingly steep axial descent with a total displacement of about 1.1% of R after reaching $\psi = 31^\circ$.

The extent of the imprint along the wake of the rotor blade can be more fully appreciated by assembling all 3 measurement zones. In the $\theta = 5^\circ$ case (fig. 33), this presentation encompasses the position of the tip vortex after 1 revolution (zone B). Clearly

the bulk of the vorticity in the wake is primarily confined to the tip vortices. It is also evident that a deficit in the out-of-plane velocity component (v) exists all along the wake of the blade as well as within the tip vortices. At this wake age ($\psi = 12.4^\circ$) the maximum magnitude of the out-of-plane component is about 54% of the maximum swirl velocity.

Although dwarfed by the intensity of the tip vortex, selected regional enlargements and a rescaling of the color contours can enhance the appearance of vorticity that is present in the remainder of the wake. In the $\theta = 5^\circ$ case (fig. 34), a thin stretch of positive vorticity overlays an equally thin stretch of negative vorticity over a majority of the wake. The positive vorticity adjacent to the first vortex (fig. 34a) probably relates to the change in blade circulation and is in the process of being accreted into the primary vortex. The patches of negative vorticity located above and to the left of both the first and second vortices are due to the shear layers created between these vortices and the surrounding fluid (fig. 35). The layered pattern of positive and negative vorticity along the inner portion of the blade wake (figs. 34b and 34c) may relate to the shear layers caused by a centrifugal pumping of the fluid within the boundary layers of the rotating blade (thereby causing a radially outward flow on both the upper and lower surface of the blade). Another reason may be the changing strength of the spanwise vorticity in the upper and lower surface boundary layers, which would in turn require the shedding of stream-wise oriented vorticity (positive and negative).

Similar flow patterns exist in the $\theta = 11^\circ$ case (figs. 36 and 37). However, one distinctive difference is the greater separation between the first and second tip vortex. As a result, the blade wake associated with the first vortex does not appear to be distorted by the second vortex. Although the second vortex continues to have some affect, theories attempting to relate measured wake vorticity to conditions on the blade can be expected to be more accurate in cases where the wake is convected away quickly and the interaction between the wakes from different blades is minimized. Another difference between the two collective pitch cases is the maximum magnitude of the out-of-plane component, which for the $\theta = 11^\circ$ case is only about 24% of the maximum swirl velocity.

Vortex characteristics at a distance of 2 chord lengths into the wake are presented in table 6. Nondimensional groups are formed using the chord, radius and rotational speed at the tip of the rotor blade.

CONCLUSIONS

1. Although the confining boundaries of the facility prevented ideal hover conditions from being achieved, a steady flow environment was formed in which rotor performance and wake structures could be studied at low rates of climb.

2. The hover figure of merit increased with increasing collective pitch angles. A reasonably well-behaved and steady increase in this quantity was observed as the climb rate diminished toward zero.

3. A majority of the vorticity in the wake is concentrated in the tip vortices. The absence of any sizeable levels of vorticity (within an order of magnitude) was noted in the remainder of the wake, even at the early wake age of $\psi = 12^\circ$.

4. Aside from the persistent presence of the tip vortices generated by each passing blade, the imprint of the blade on the remainder of the wake is evident primarily in terms of the out-of-plane components of velocity and vorticity. However, this evidence appears to fade quickly and cannot be observed at all in the wake of the following blade ($\psi = 180^\circ$).

5. When the rotor thrust is low (for $\theta = 5^\circ$), the inboard portion of the wake is distorted by the close proximity of the tip vortex from the preceding blade. The axial separation distance is greatly extended when the rotor thrust is increased ($\theta = 11^\circ$), which may allow the vortical composition of the near wake to be more easily identified with the drag components (induced and profile) on the rotor.

6. The size of the vortex core in the near wake ($\psi \leq 31^\circ$) is about 6% of the blade chord for collective pitch angles of 5° and 11° . At $\psi = 12^\circ$, the out-of-plane velocity component is about 8% of the rotational speed of the blade tip at $\theta = 5^\circ$ and the swirl velocity is only slightly higher. However, at $\theta = 11^\circ$, the out-of-plane velocity increases to 11% of the rotational speed of the blade tip, but the swirl velocity nearly triples the magnitude of the out-of-plane velocity.

REFERENCES

- [1] Wu, J. C.; and Wang, C. M.: Separate Determination of Coexisting Components of Aerodynamic Drag on Rotors. USAAMCOM TR-01-D-10, 2001.
- [2] Caradonna, F.; Henley, E.; Silva, M.; Huang, S.; Komerath, N.; Reddy, U.; Funk, R.; Wong, O.;

Table 6: Vortex Characteristics at $\psi = 12.4^\circ$

θ	r_c/c	$(u+v)/R\Omega$	$w/R\Omega$
5°	6.4%	8.9%	8.4%
11°	6.1%	33.8%	11.0%

- Ames, R.; Darden, L.; Villareal, L.; and Gregory, J.: An Experimental Study of a Rotor in Axial Flight. AHS Technical Specialists' Meeting for Rotorcraft Acoustics and Aerodynamics, Williamsburg, VA, 1997.
- [3] Lourenco, L. M.: Particle Image Velocimetry. von Karman Institute for Fluid Dynamics, Lecture Series on Particle Image Velocimetry, 1996.
- [4] Arroyo, M. P.; and Greated, C. A.: Stereoscopic Particle Image Velocimetry. *Measurement Science and Technology*, 2, 1991.
- [5] Prasad, A. K.; and Jensen, K.: Scheimpflug Stereocamera for Particle Image Velocimetry in Liquid Flows. *Applied Optics*, 34:7092-9, 1995.
- [6] Lourenco, L.: Mesh-Free Second-Order Accurate Algorithm for PIV Processing. Proceedings of VSJ-SPIE98, Paper AB079, Yokohama, Japan, 1998.
- [7] Westerweel, J.: Theoretical Analysis of the Measurement Precision and Reliability in PIV. Proceedings of the Third International Workshop on PIV'99, 1999.
- [8] Rajagopalan, R. G.: A Procedure for Rotor Performance, Flowfield and Interference: A Perspective. AIAA-2000-0116. AIAA 38th Aerospace Sciences Meeting & Exhibit, Reno, NV, 2000.
- [9] McAlister, K. W.; Tung, C.; and Heineck, J. T.: Forced Diffusion of Trailing Vorticity from a Hovering Rotor. AHS 57th Annual Forum, Washington, D.C., 2001.

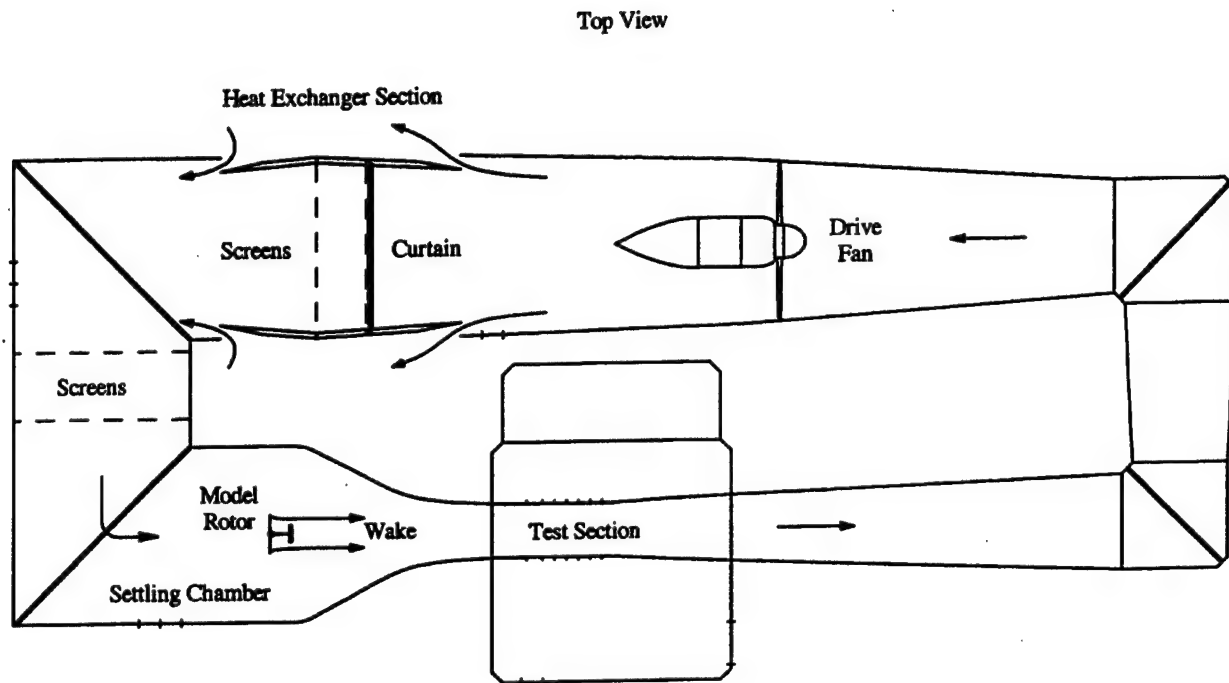


Figure 1: 7- by 10-Foot Wind Tunnel flow circuit.

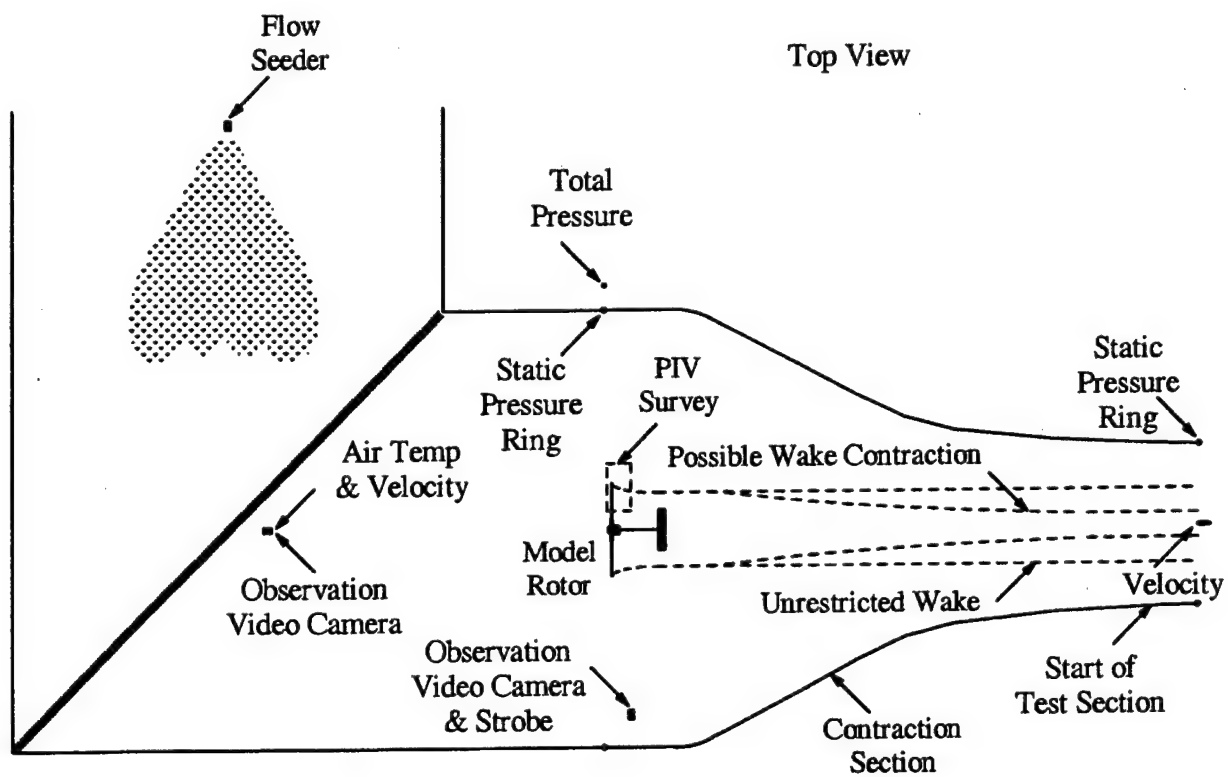


Figure 2: Instrument setup in settling chamber of 7- by 10-Foot Wind Tunnel.

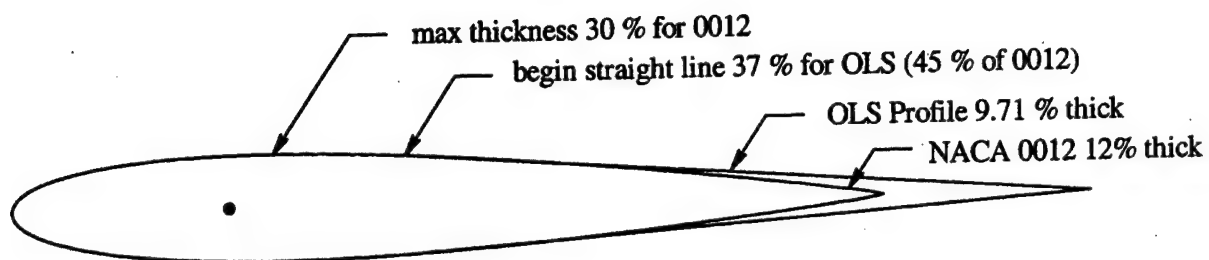


Figure 3: OLS blade profile.

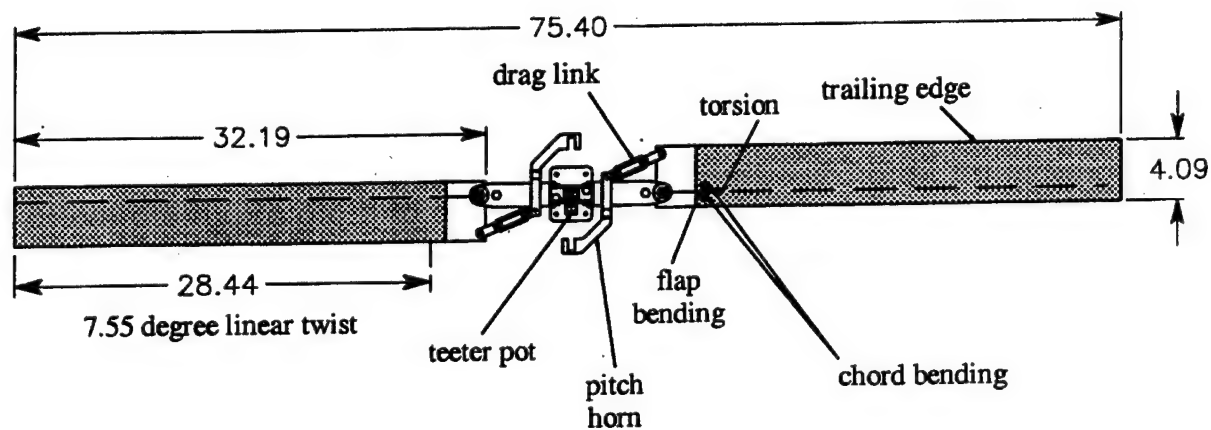


Figure 4: OLS Model rotor.

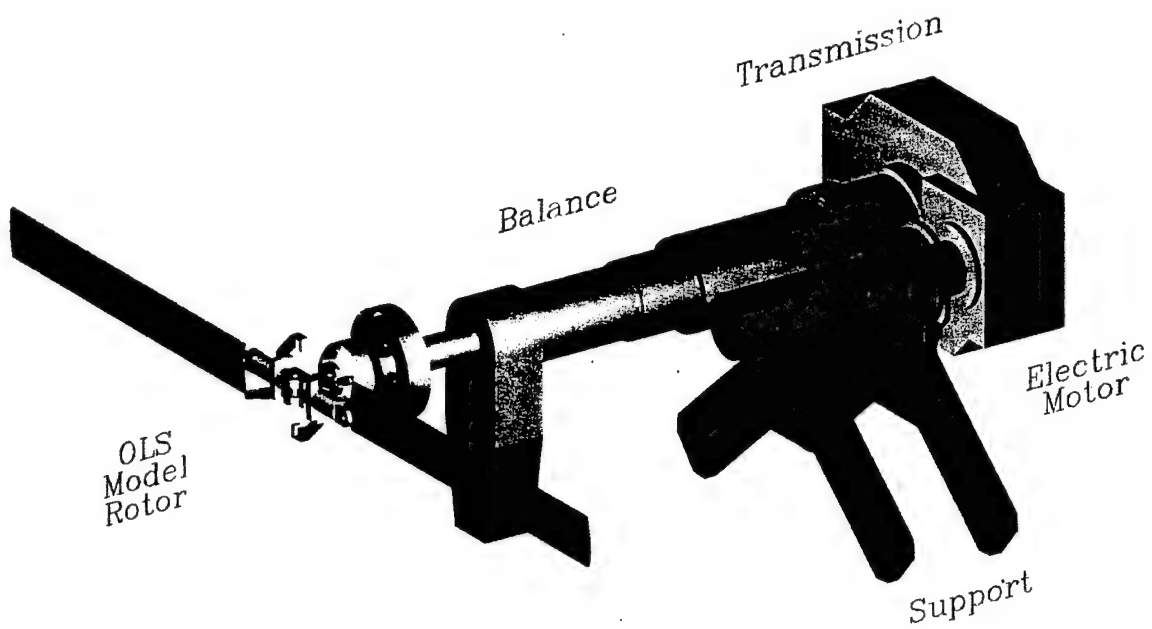


Figure 5: Model rotor assembly.

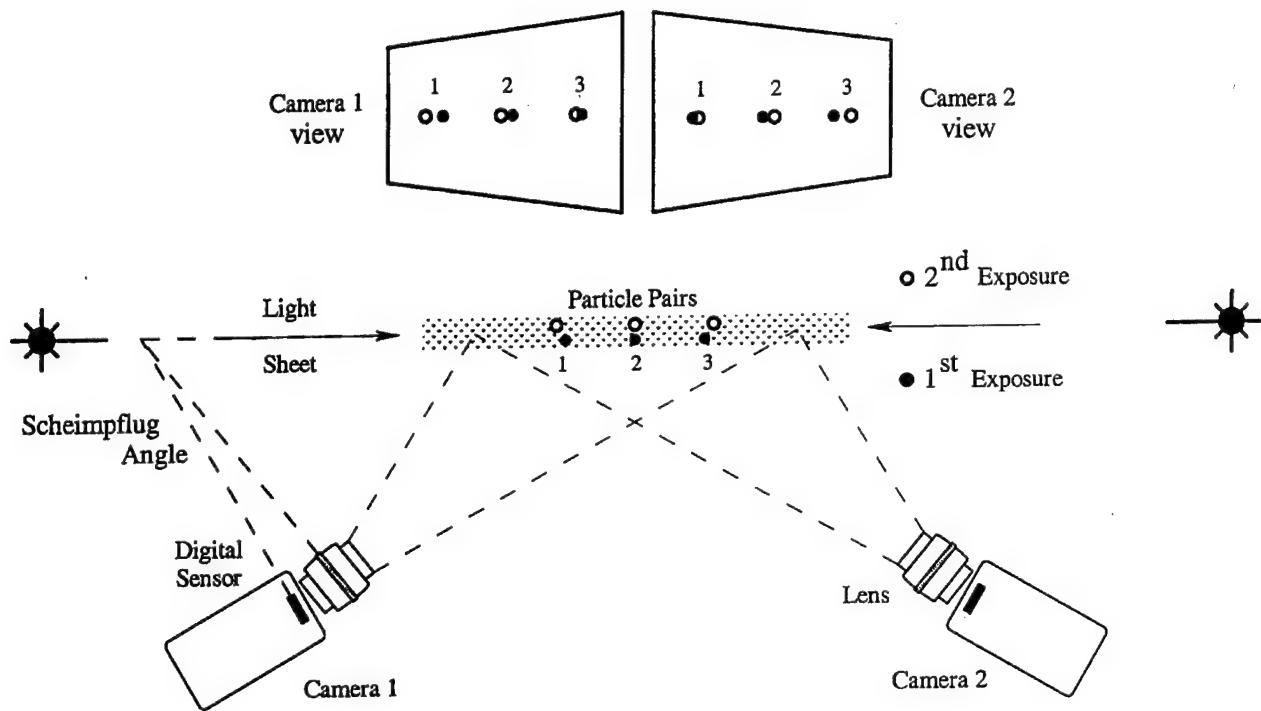


Figure 6: Perspective effect of particle displacement with Stereoscopic PIV.

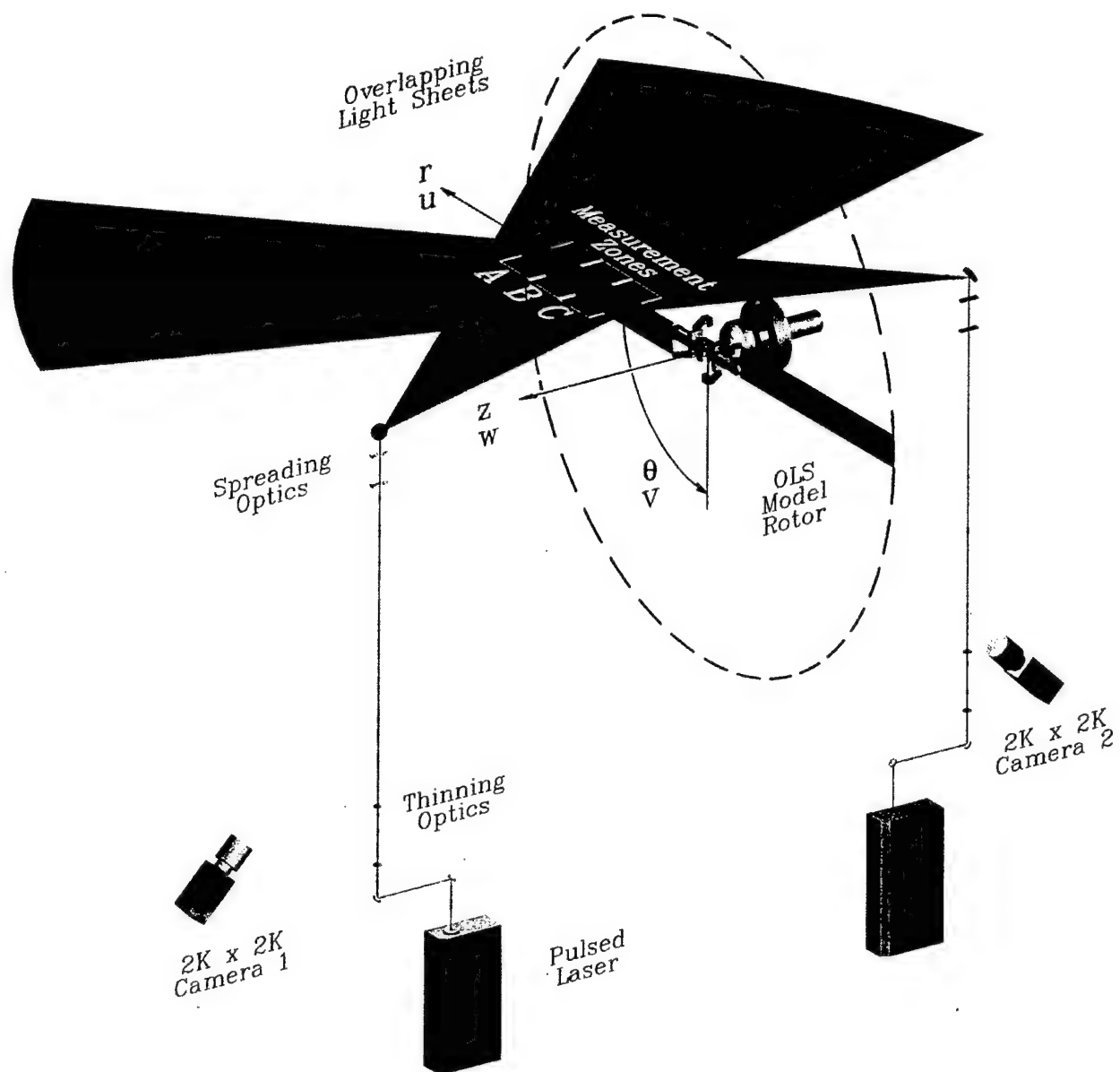


Figure 7: Particle imaging system layout.

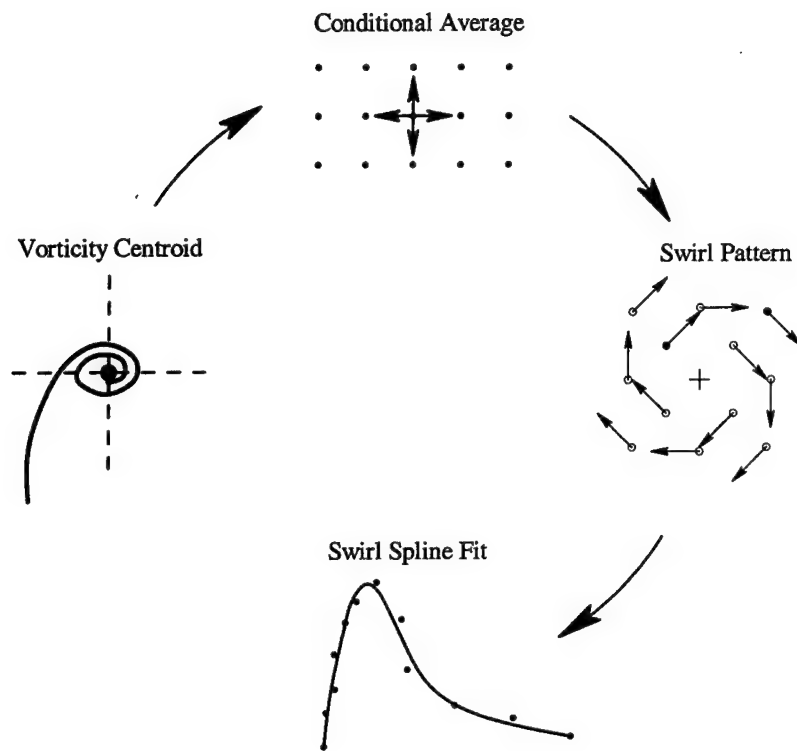


Figure 8: Sequence for extracting vortex characteristics.

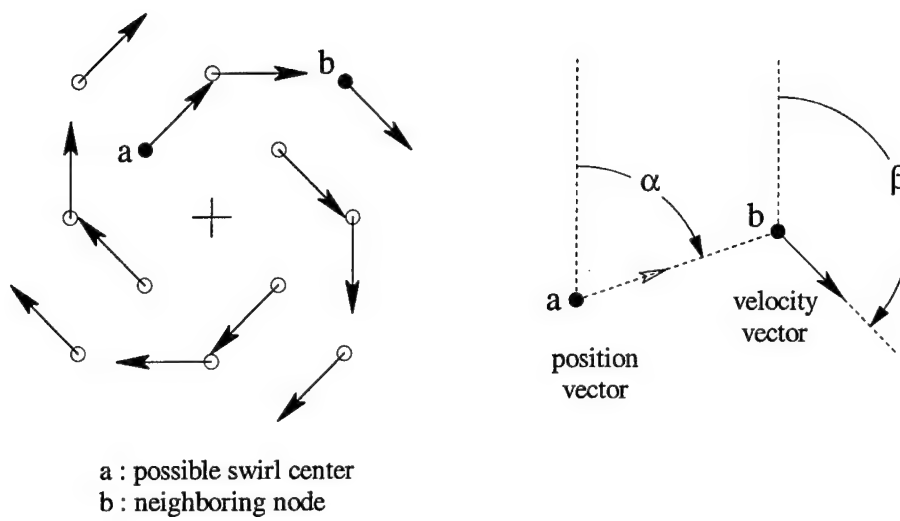


Figure 9: Angles used in search for center of swirl.

Configuration: Normal Tunnel
 $\theta=5^\circ$ Runs 1880 thru 1911
 $\theta=11^\circ$ Runs 2435 thru 2465

Configuration: Return Flow Blocked
 $\theta=5^\circ$ Runs 1951 thru 1983
 $\theta=11^\circ$ Runs 1986 thru 2018

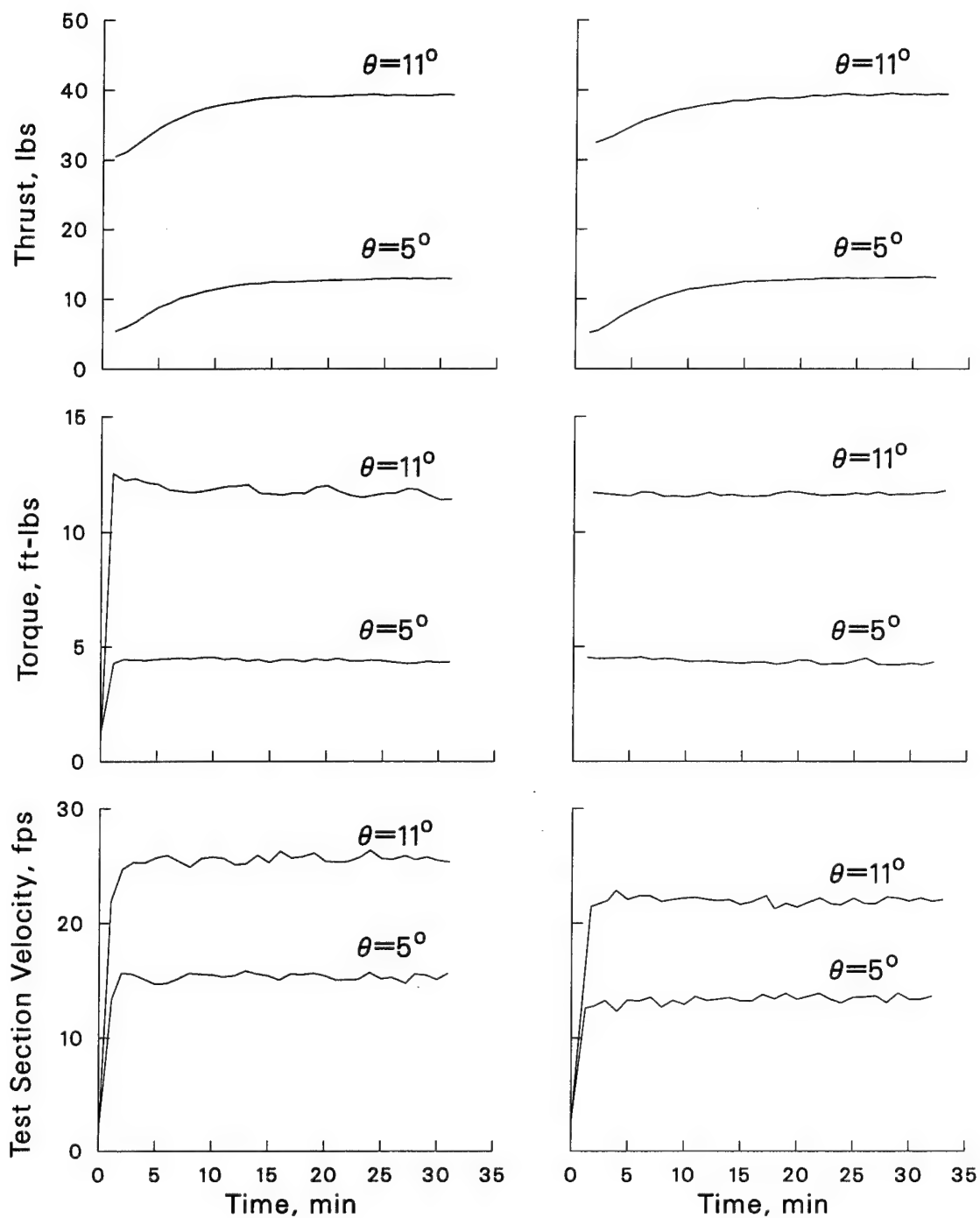


Figure 10: Time required to reach equilibrium conditions.

Configuration: Return Flow Blocked
 $\theta=5^\circ$ Runs 2962 thru 3082

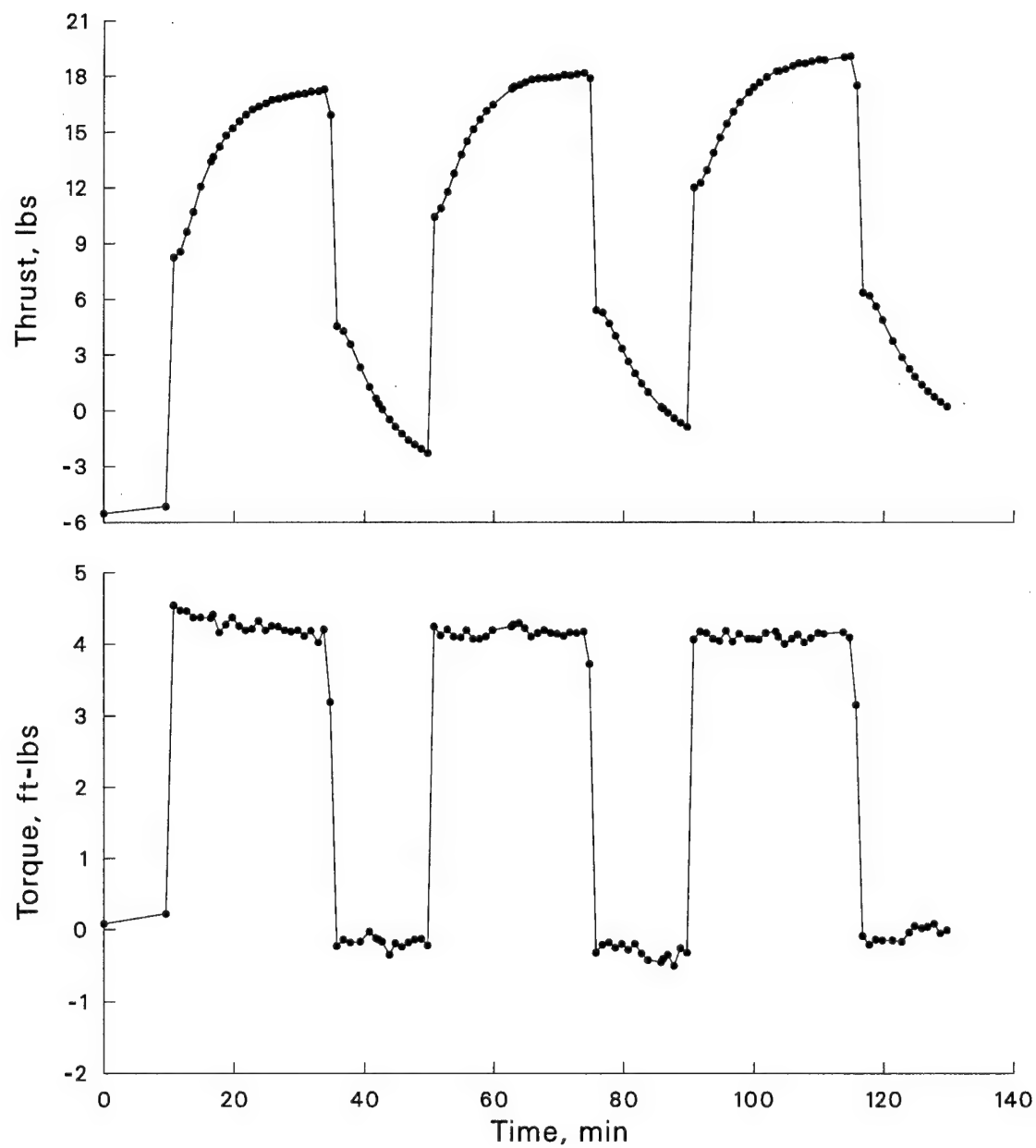
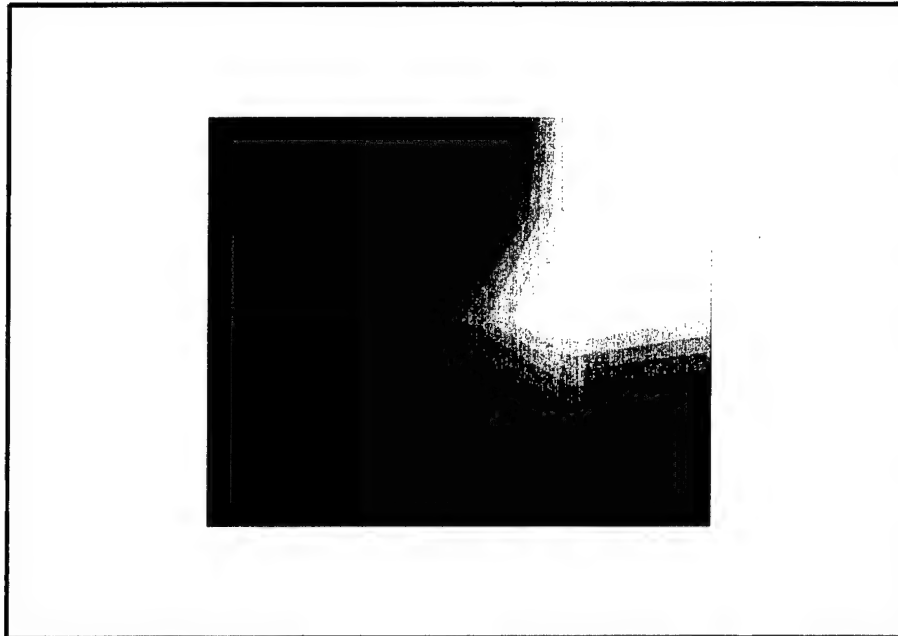


Figure 11: Temperature effects on rotor loads.

Configuration: Tunnel Return Flow Blocked

7  11 m/s



$\theta=3^\circ$

Central Region

$V_{\min} = 6.8$ fps

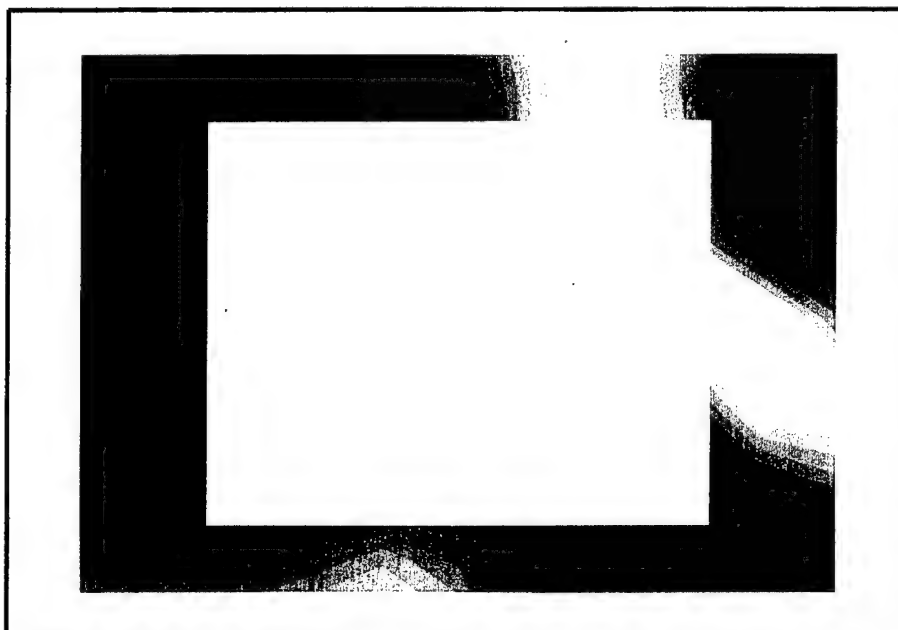
$V_{\max} = 9.4$ fps

$V_{\text{ctr}} = 8.7$ fps

$V_{\text{ave}} = 8.2$ fps

Run series

2108 - 2170



$\theta=3^\circ$

Border Region

$V_{\min} = 6.8$ fps

$V_{\max} = 10.6$ fps

Both Regions

$V_{\text{ave}} = 8.3$ fps

Run series

2108 - 2223

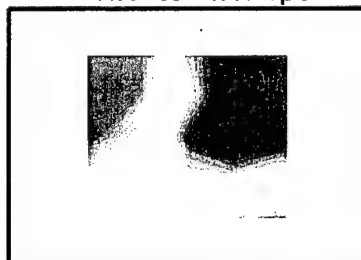
Figure 12: Velocity distribution in test section with return flow blocked.

Air return section blocked ... fan speed = 0 RPM

Collective = 3°
Run Series 2536
5.5 to 8.3 fps



Collective = 7°
Run Series 2602
11.6 to 17.1 fps



Collective = 11°
Run Series 2668
17.2 to 23.3 fps



Test section velocity ... view looking downstream

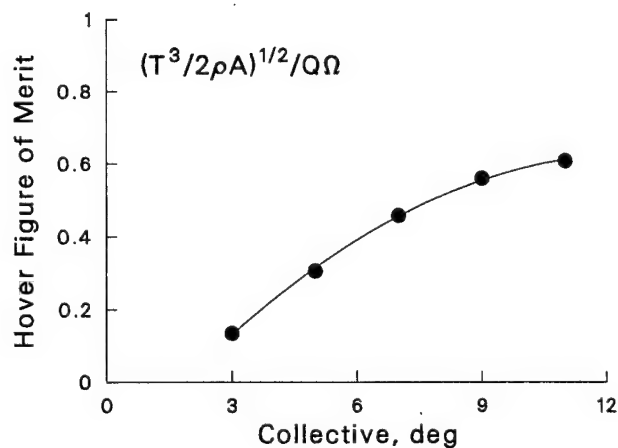
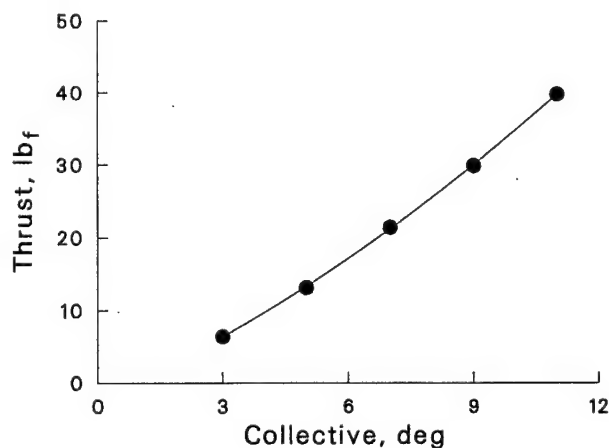
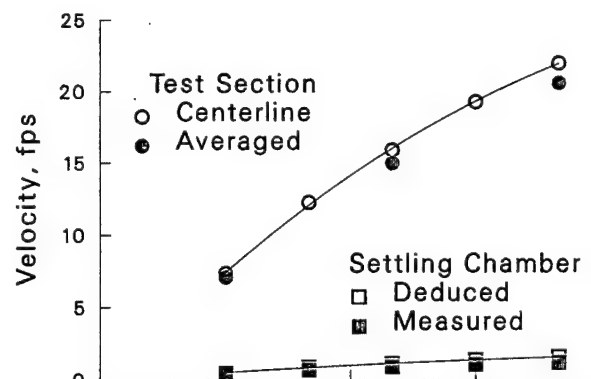
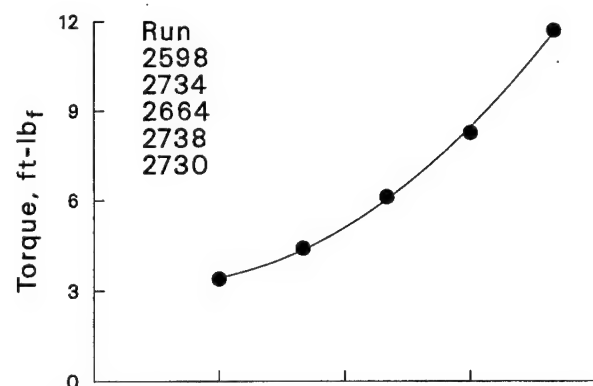


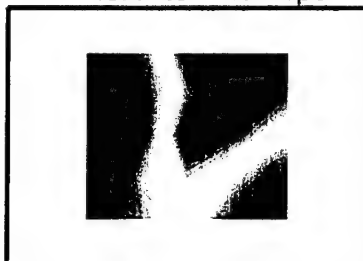
Figure 13: Rotor loads and tunnel velocities with return flow blocked.

Normal wind tunnel configuration ... fan speed = 0 RPM

Collective = 3°
Run Series 2750
7.4 to 10.3 fps



Collective = 7°
Run Series 2816
15.4 to 19.8 fps



Collective = 11°
Run Series 2882
20.8 to 26.3 fps



Test section velocity ... view looking downstream

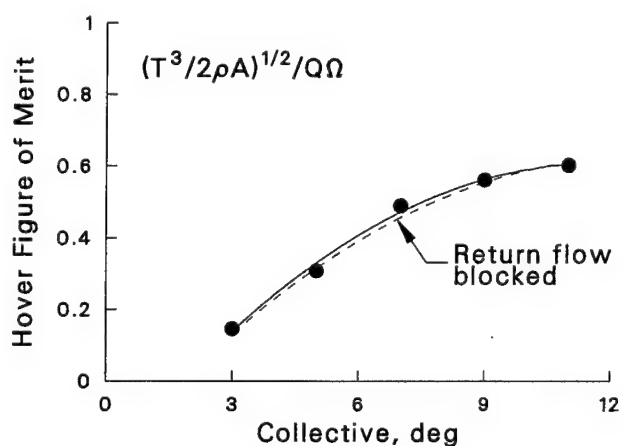
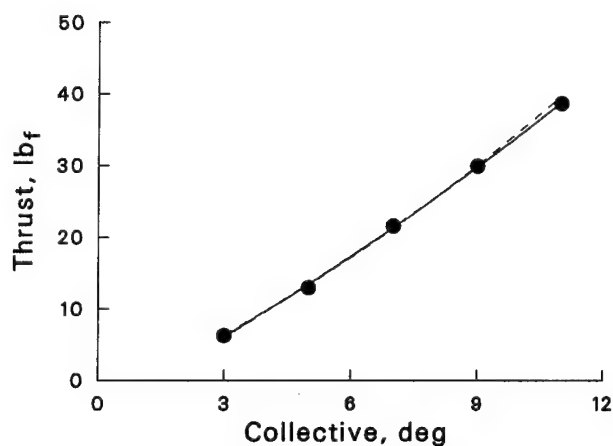
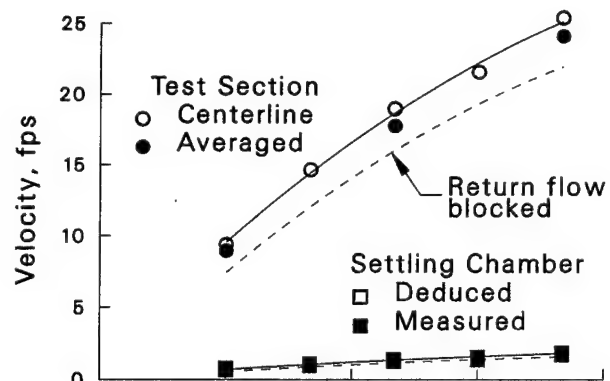
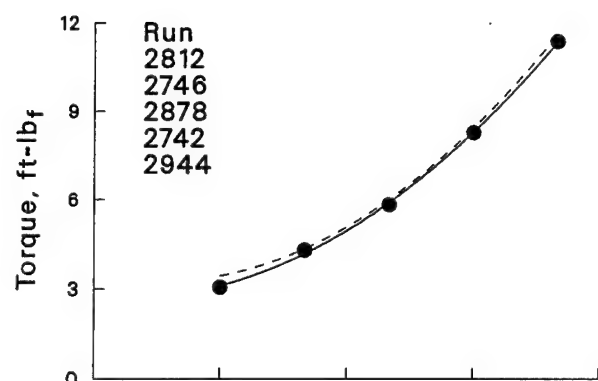


Figure 14: Rotor loads and tunnel velocities with return flow unblocked and fan speed = 0 RPM.

Normal wind tunnel configuration ... fan speed = 22 RPM

Collective = 3°
Run Series 777
31.5 to 34.3 fps



Collective = 7°
Run Series 848
31.6 to 35.4 fps



Collective = 11°
Run Series 919
31.0 to 35.5 fps



Test section velocity ... view looking downstream

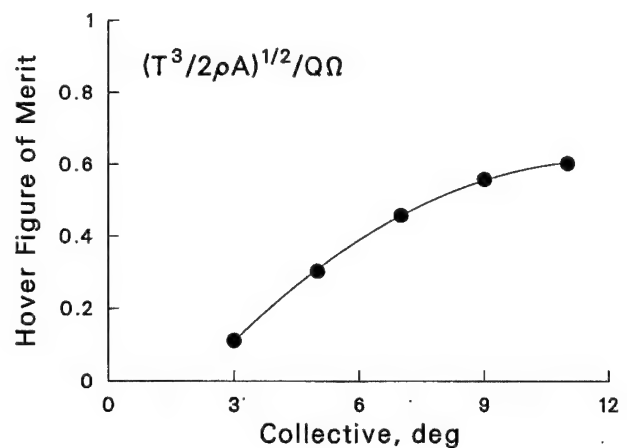
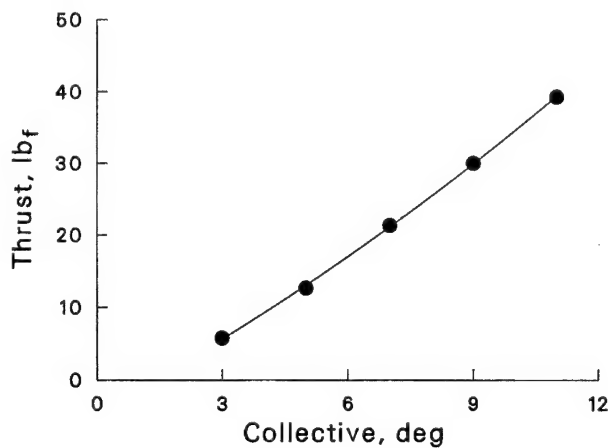
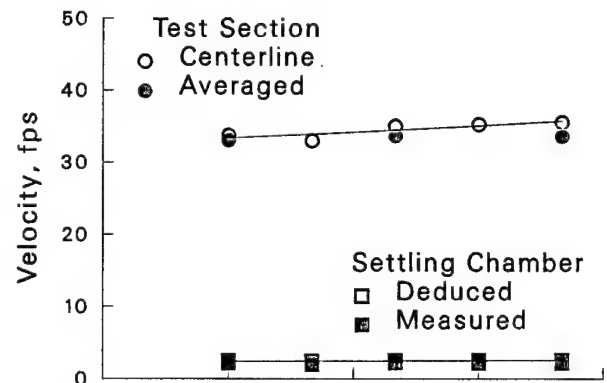
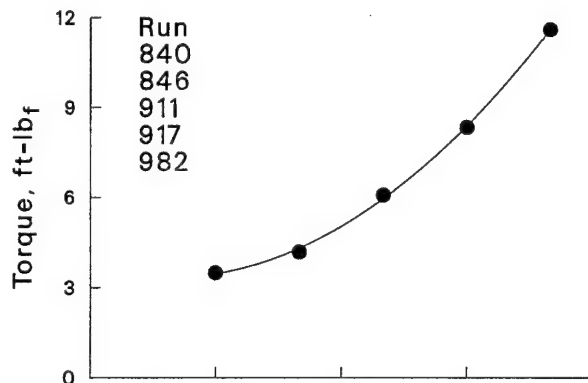


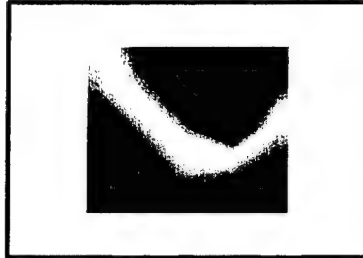
Figure 15: Rotor loads and tunnel velocities with return flow unblocked and fan speed = 22 RPM.

Normal wind tunnel configuration ... fan speed = 52 RPM

Collective = 3°
Run Series 986
61.9 to 65.1 fps



Collective = 7°
Run Series 1062
55.7 to 59.3 fps



Collective = 11°
Run Series 1138
55.2 to 60.8 fps



Test section velocity ... view looking downstream

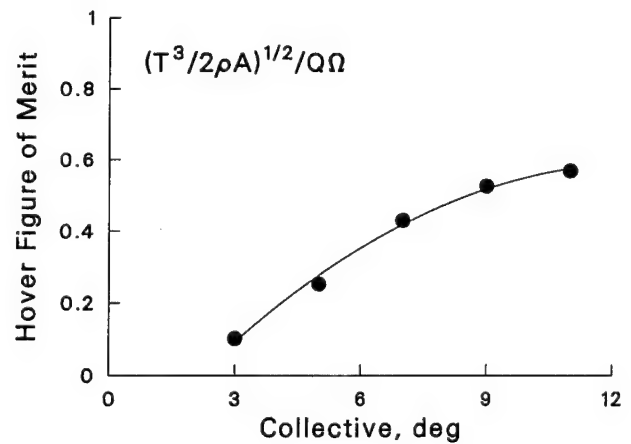
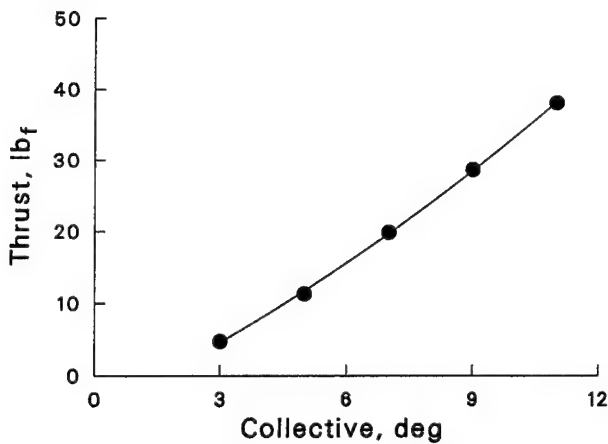
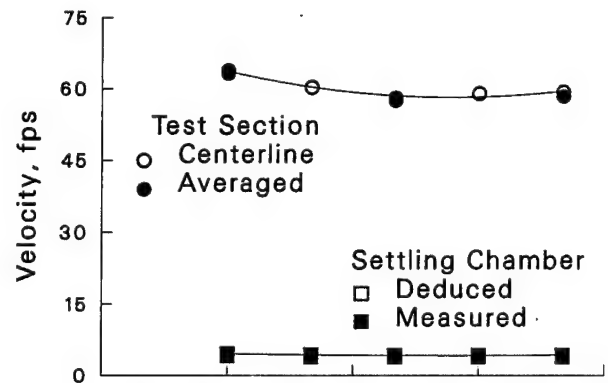
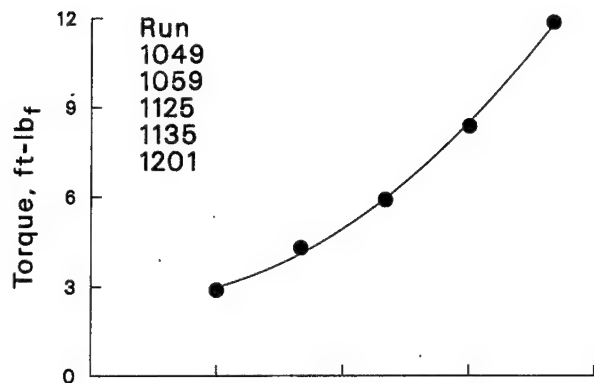


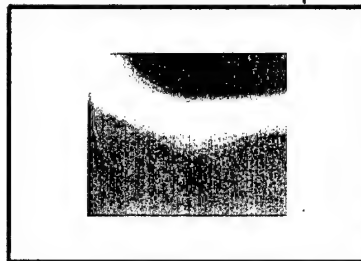
Figure 16: Rotor loads and tunnel velocities with return flow unblocked and fan speed = 52 RPM.

Normal wind tunnel configuration ... fan speed = 80 RPM

Collective = 3°
Run Series 1210
87.8 to 92.1 fps



Collective = 7°
Run Series 1289
86.4 to 91.9 fps



Collective = 11°
Run Series 1365
86.4 to 92.8 fps



Test section velocity ... view looking downstream

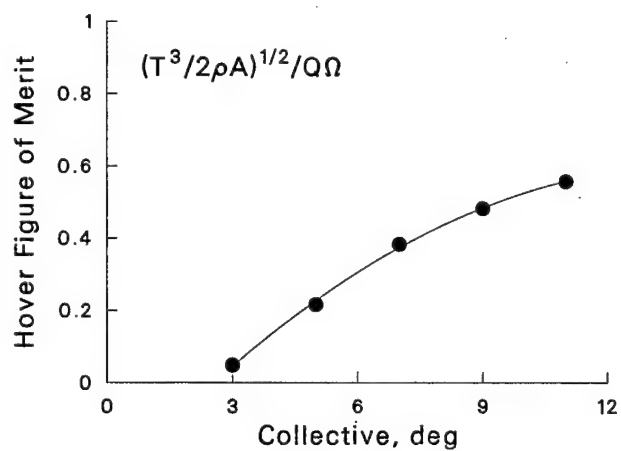
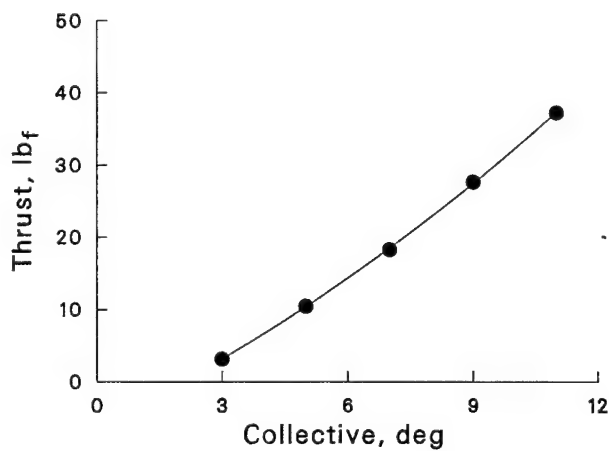
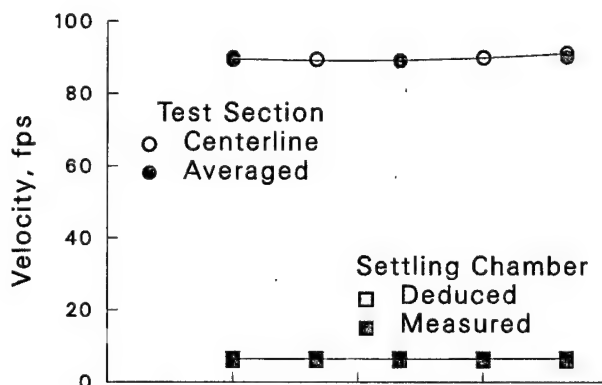
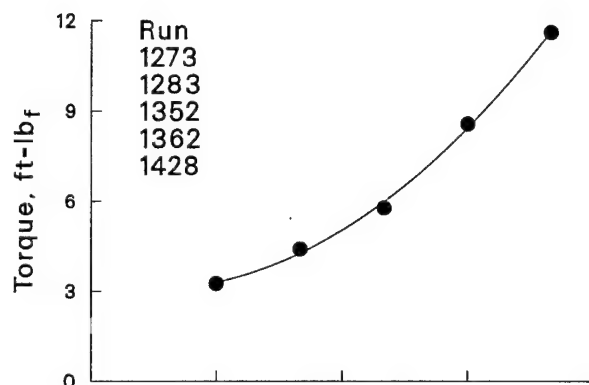


Figure 17: Rotor loads and tunnel velocities with return flow unblocked and fan speed = 80 RPM.

Normal wind tunnel configuration ... fan speed = 105 RPM

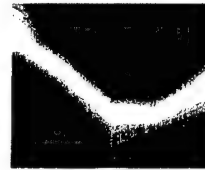
Collective = 3°
Run Series 1692
120.3 to 125.8 fps



Collective = 7°
Run Series 1629
120.9 to 126.0 fps



Collective = 11°
Run Series 1566
119.2 to 124.7 fps



Test section velocity ... view looking downstream

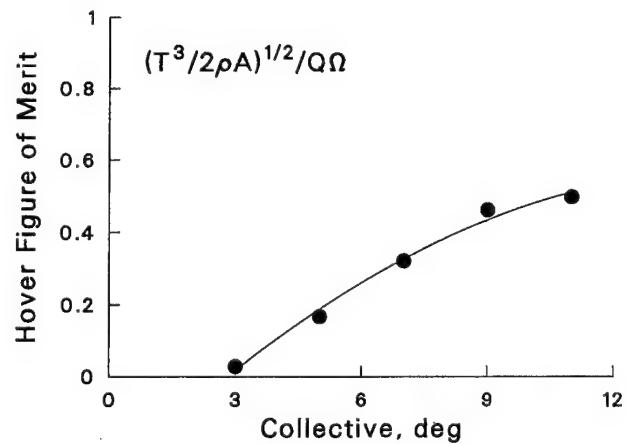
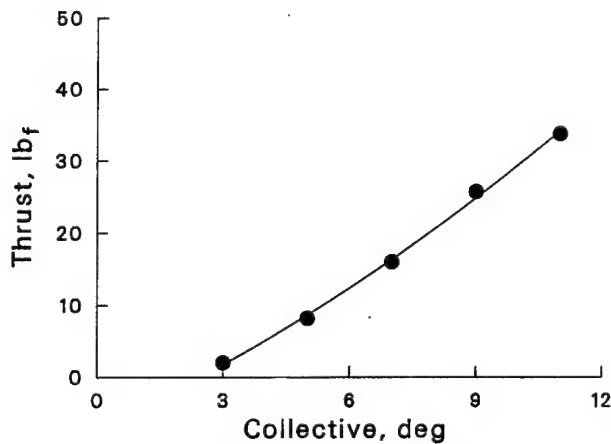
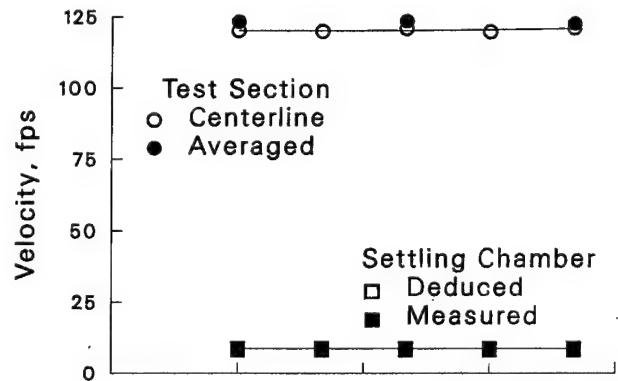
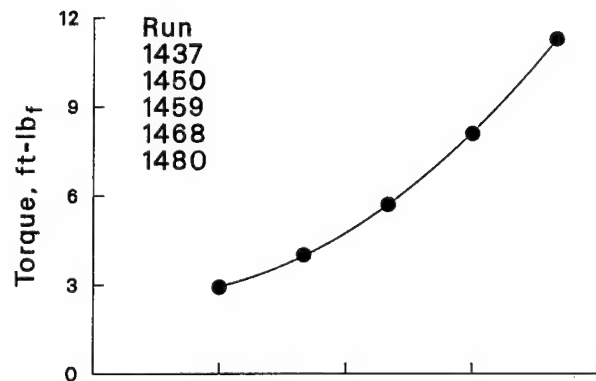


Figure 18: Rotor loads and tunnel velocities with return flow unblocked and fan speed = 105 RPM.

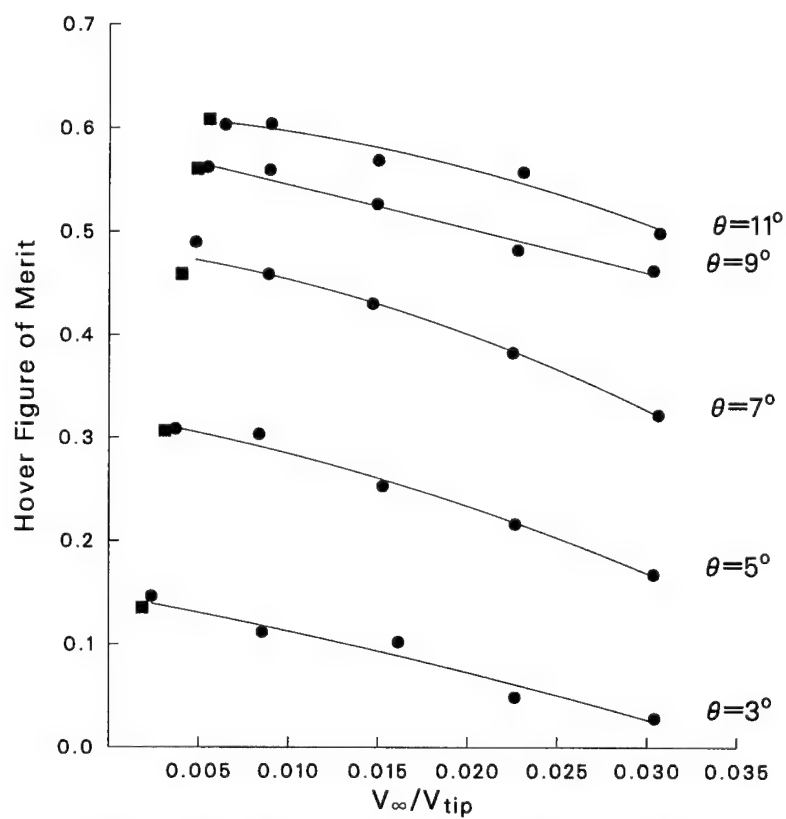
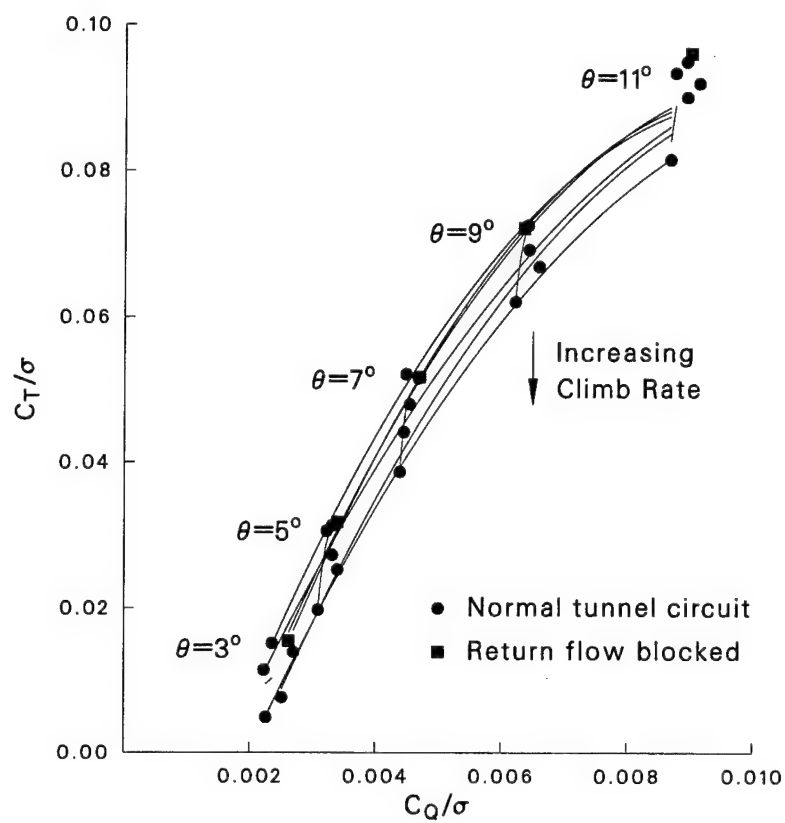
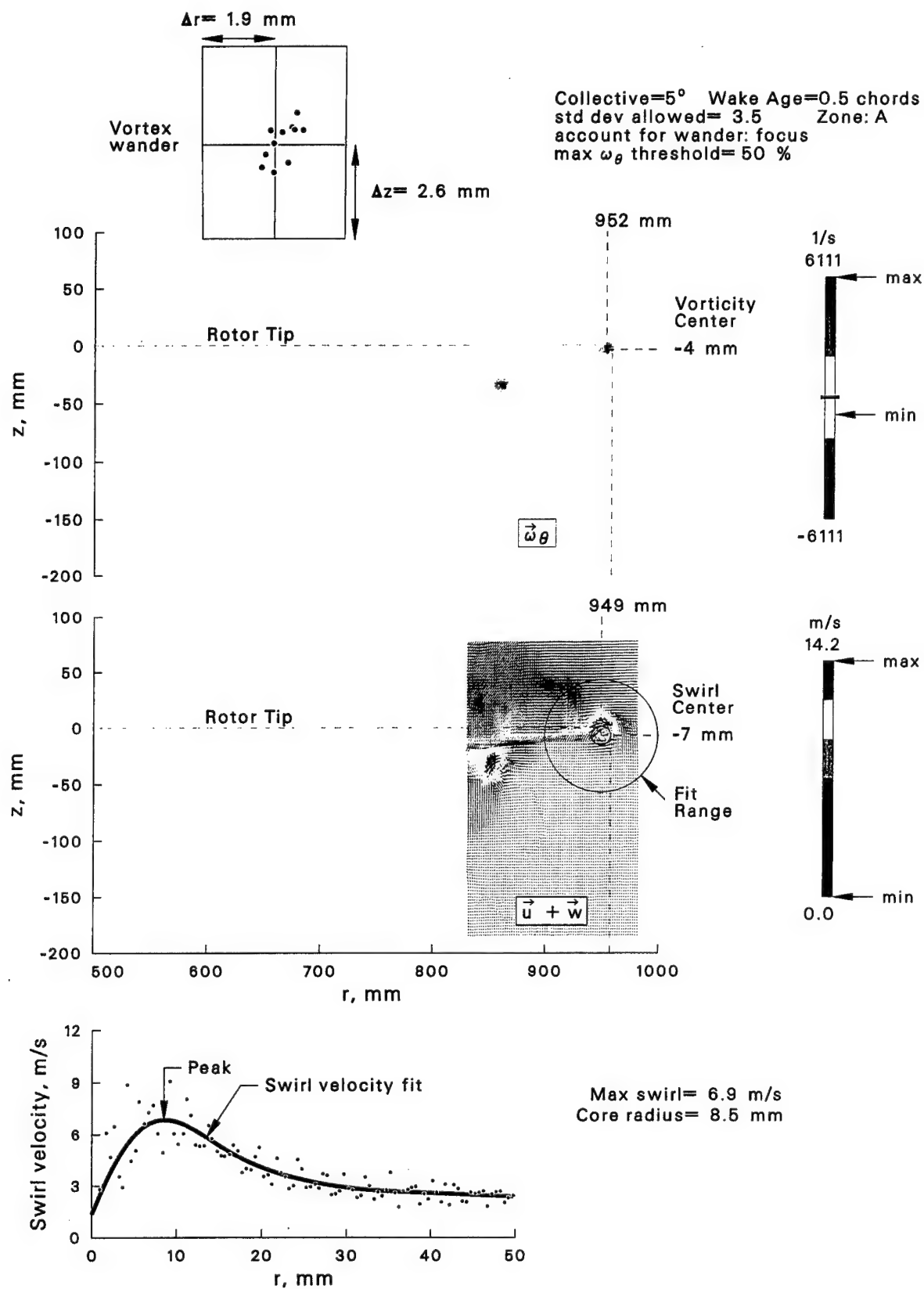
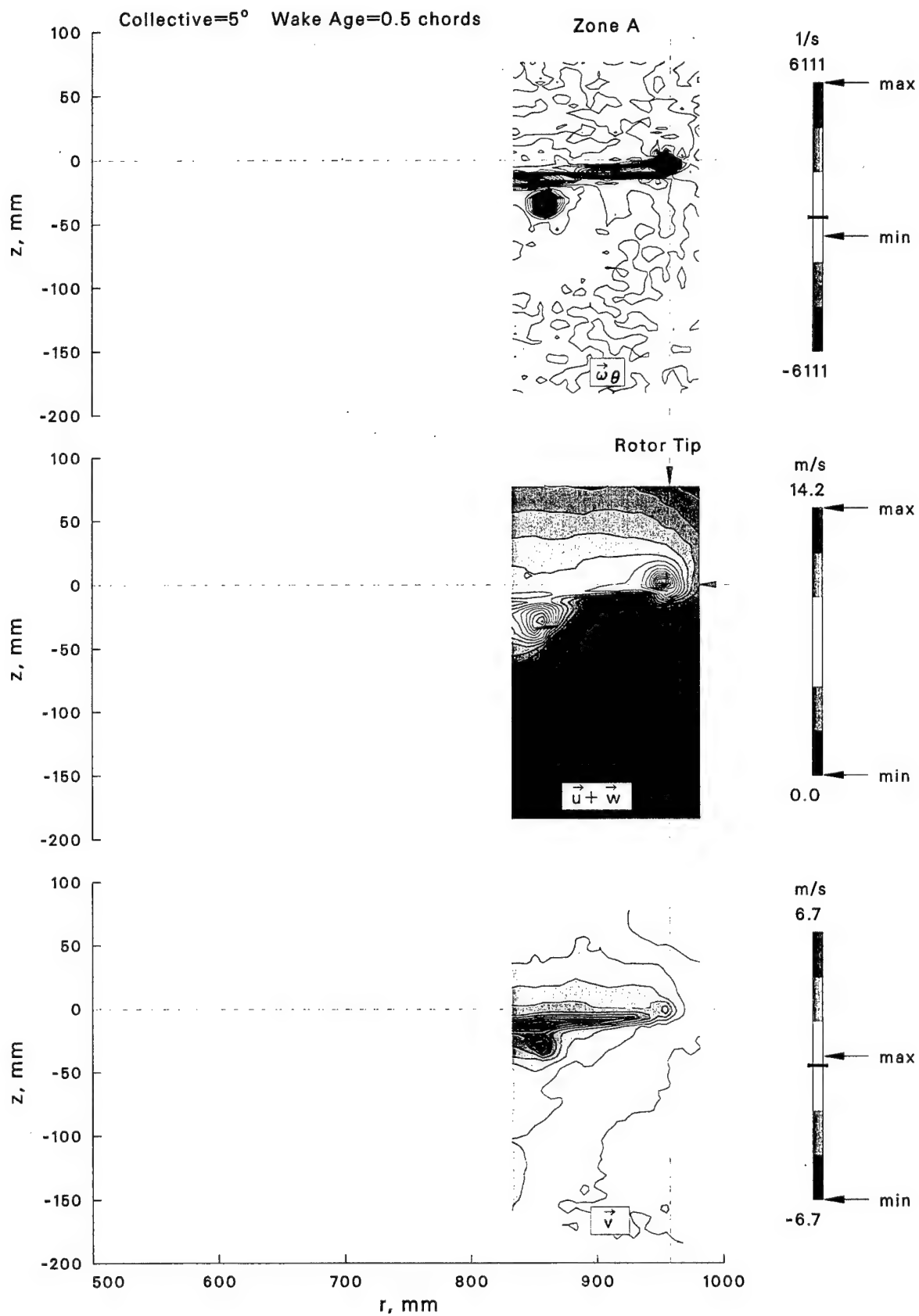


Figure 19: Rotor performance for various climb rates and collective pitch angles.



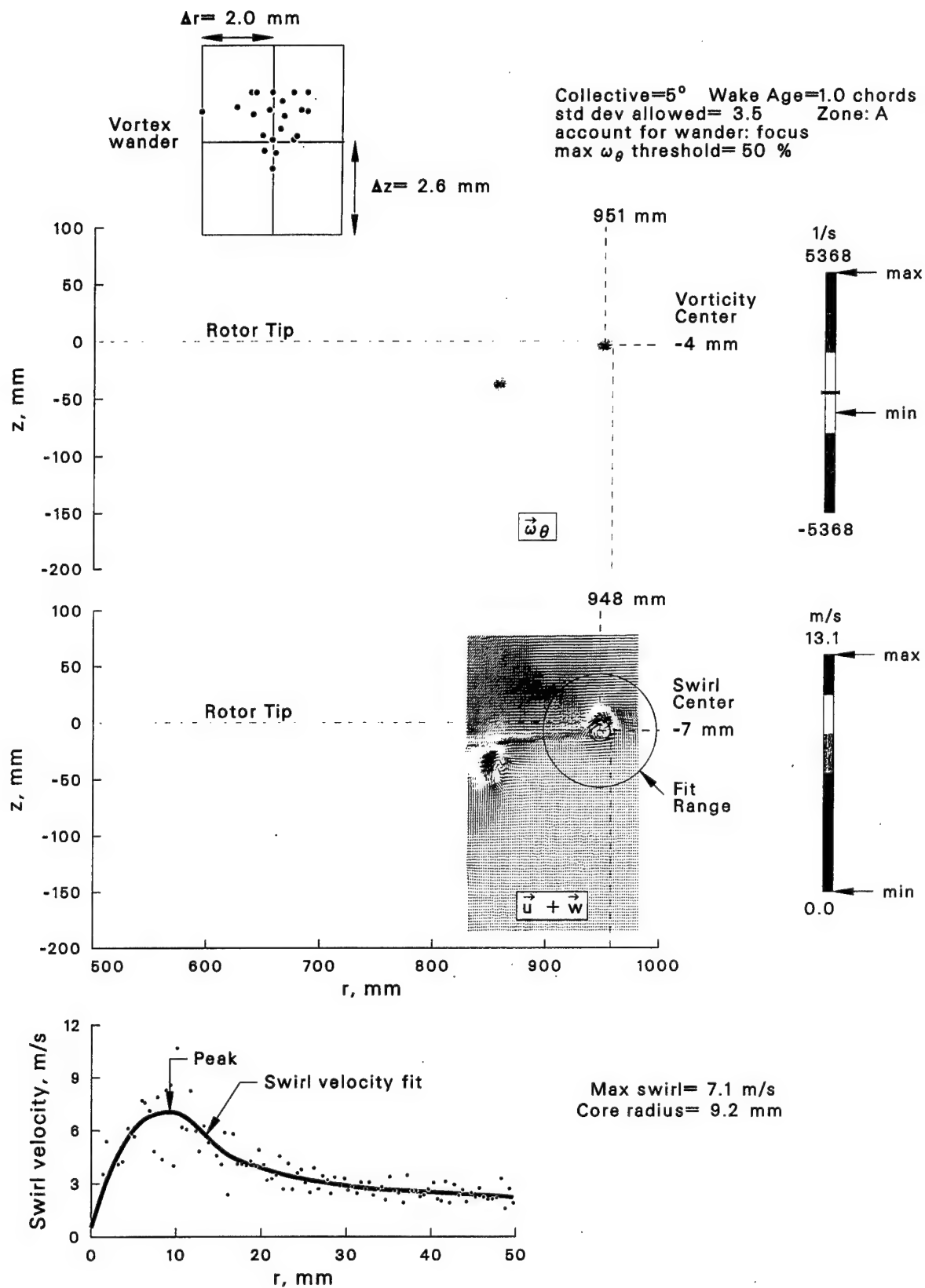
(a) Location and size of vortex.

Figure 20: Near wake at $\theta = 5^\circ$ and $\psi = 3.1^\circ$ (0.5 chord downstream from rotor tip).



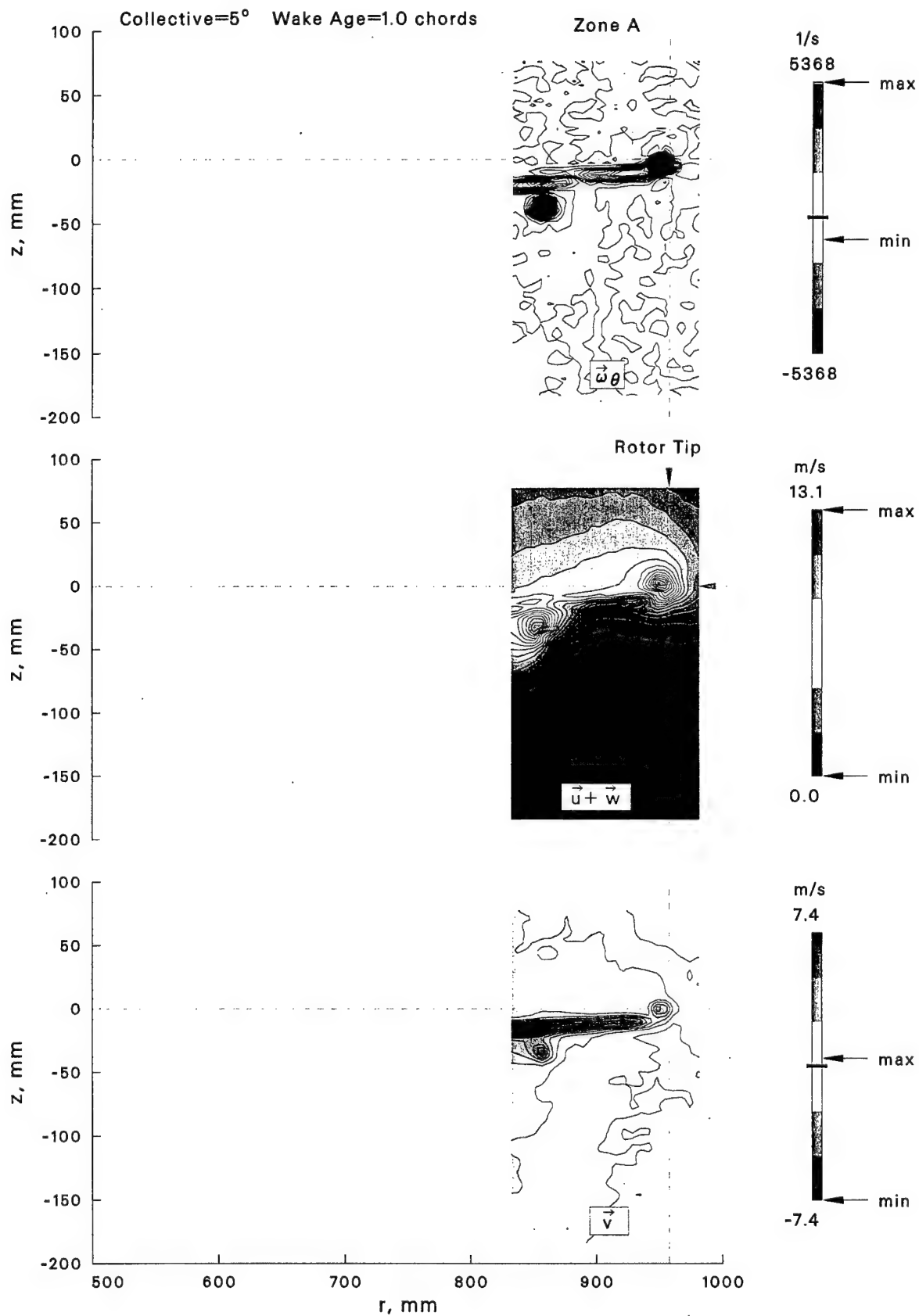
(b) Velocity and vorticity contour maps.

Figure 20: Concluded.



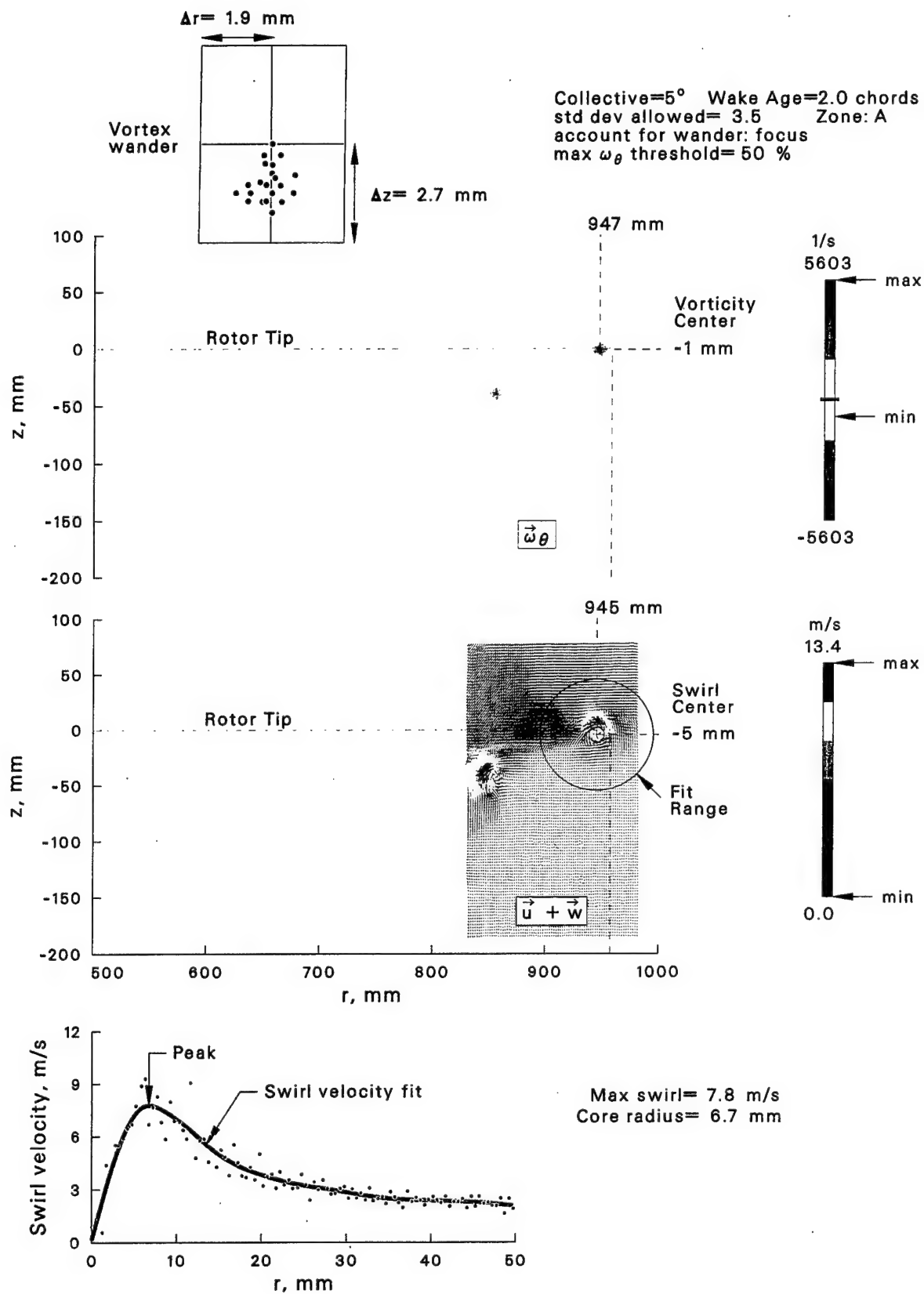
(a) Location and size of vortex.

Figure 21: Near wake at $\theta = 5^\circ$ and $\psi = 6.2^\circ$ (1 chord downstream from rotor tip).



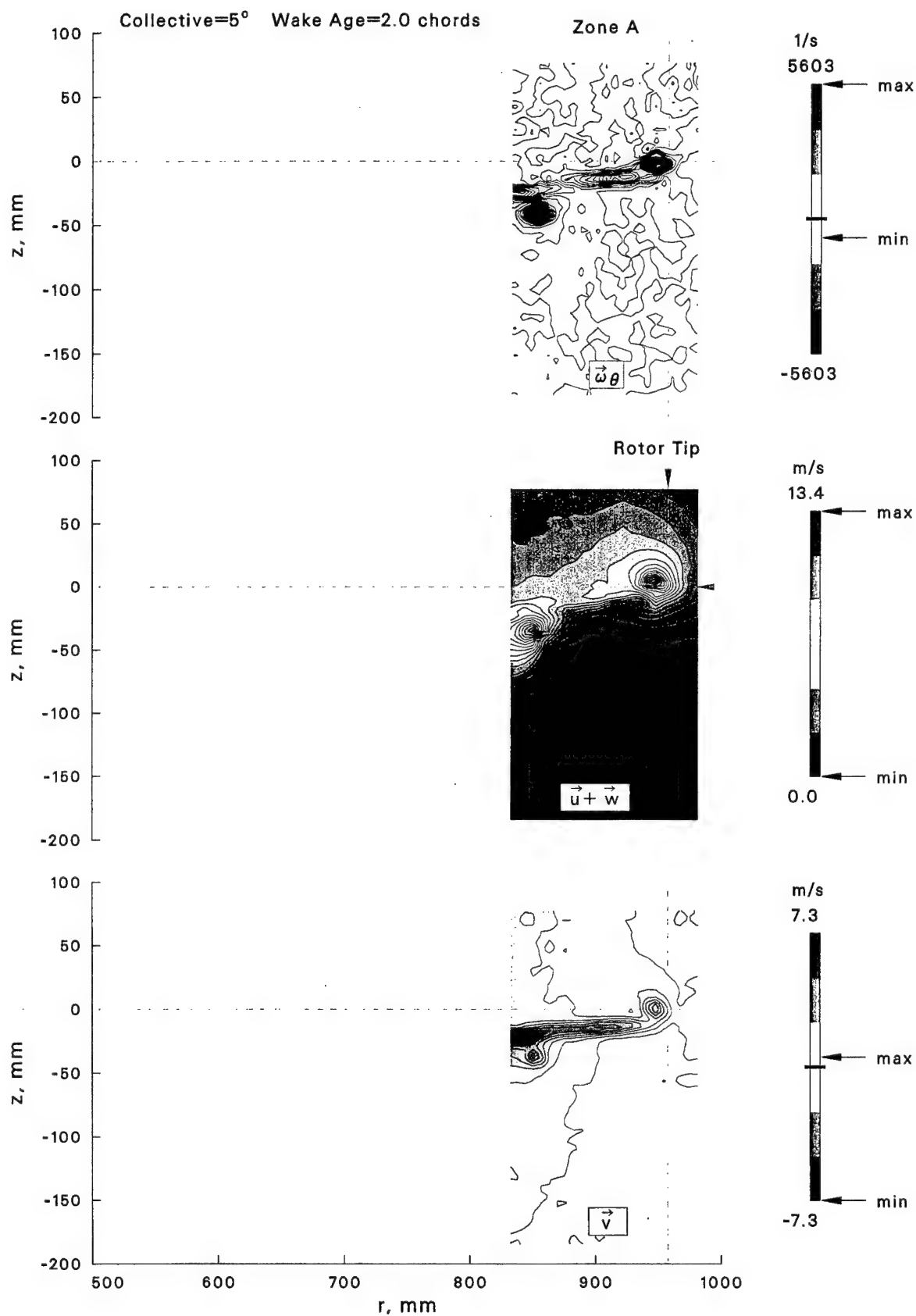
(b) Velocity and vorticity contour maps.

Figure 21: Concluded.



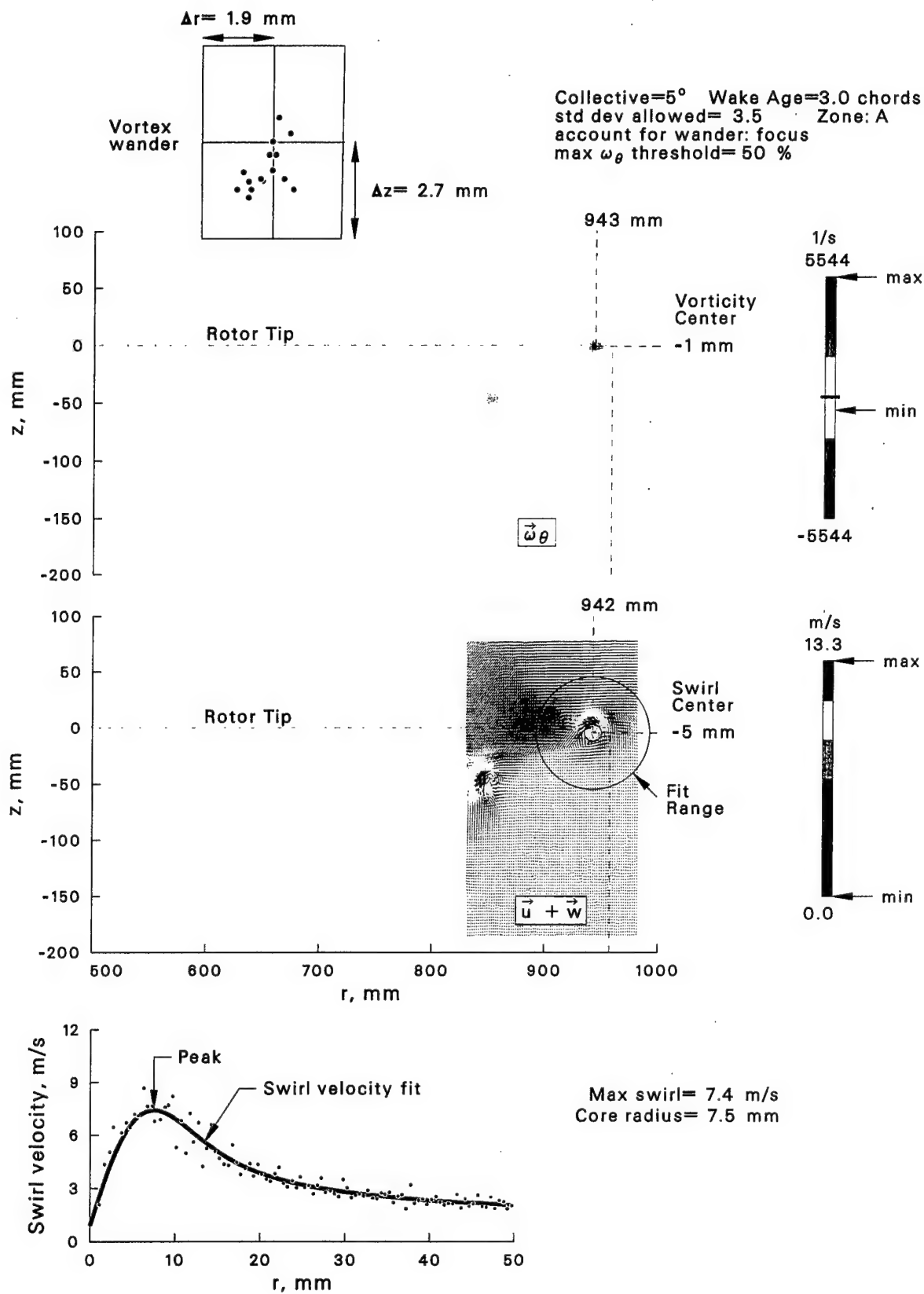
(a) Location and size of vortex.

Figure 22: Near wake at $\theta = 5^\circ$ and $\psi = 12.4^\circ$ (2 chords downstream from rotor tip).



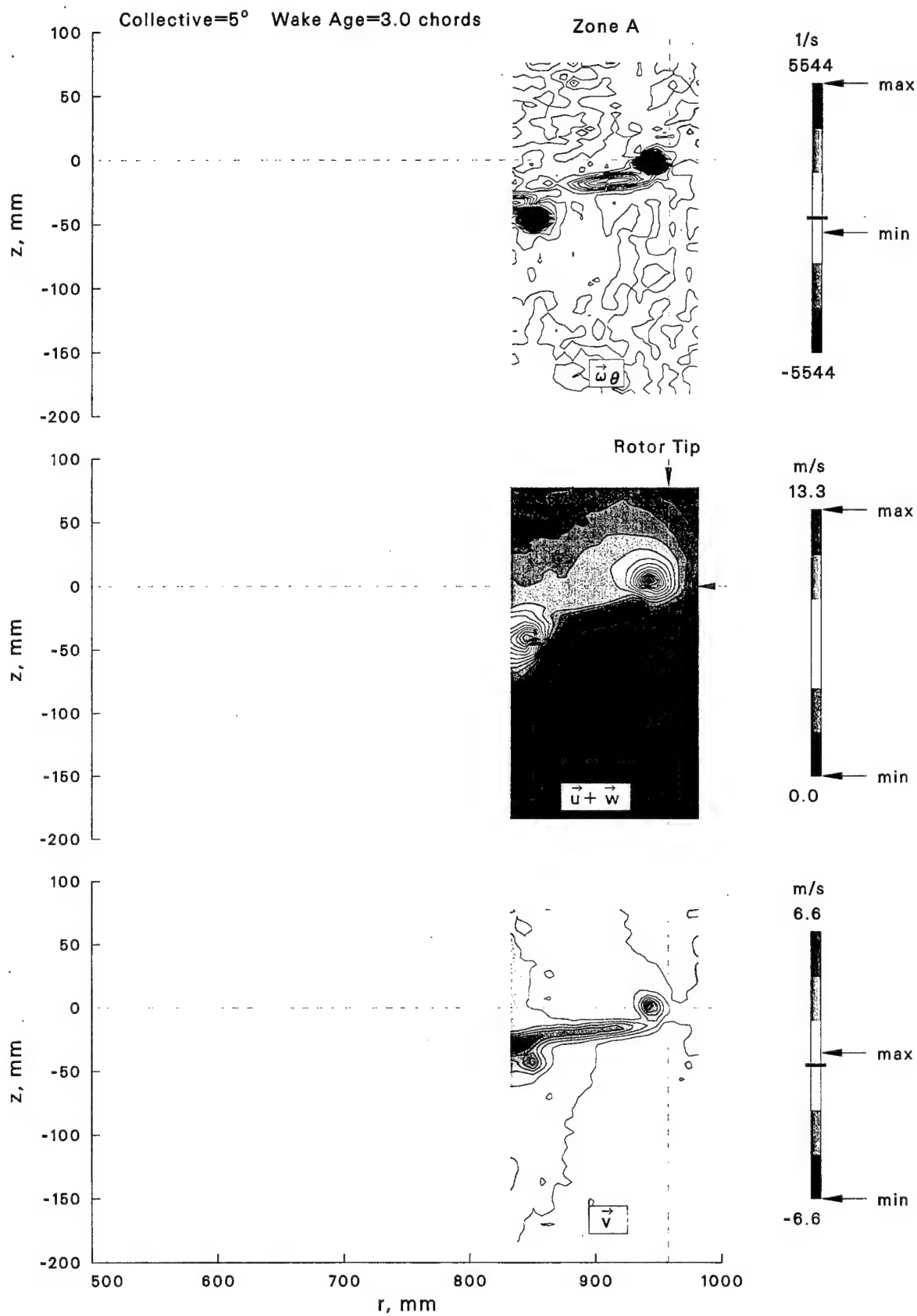
(b) Velocity and vorticity contour maps.

Figure 22: Concluded.



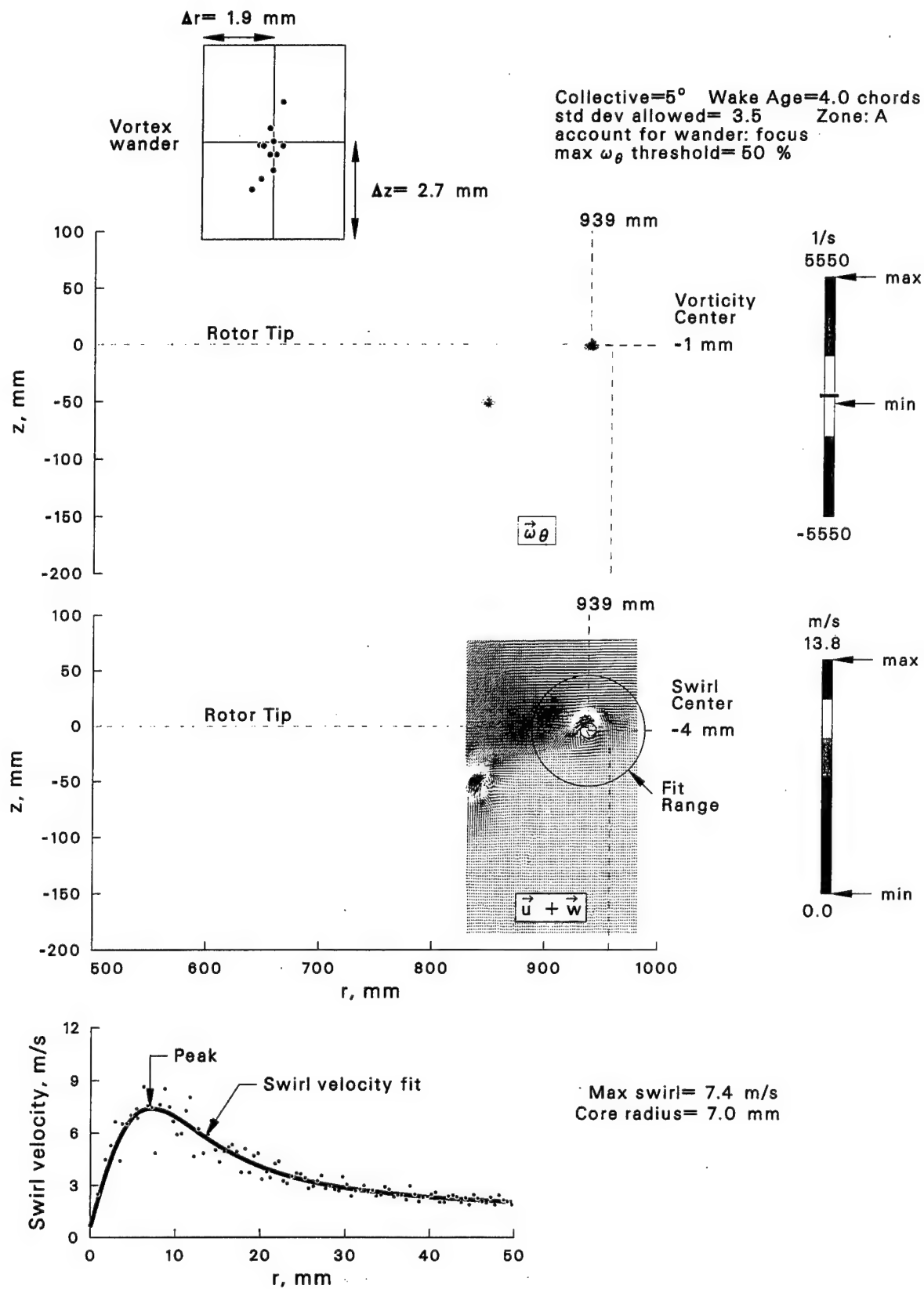
(a) Location and size of vortex.

Figure 23: Near wake at $\theta = 5^\circ$ and $\psi = 18.6^\circ$ (3 chords downstream from rotor tip).



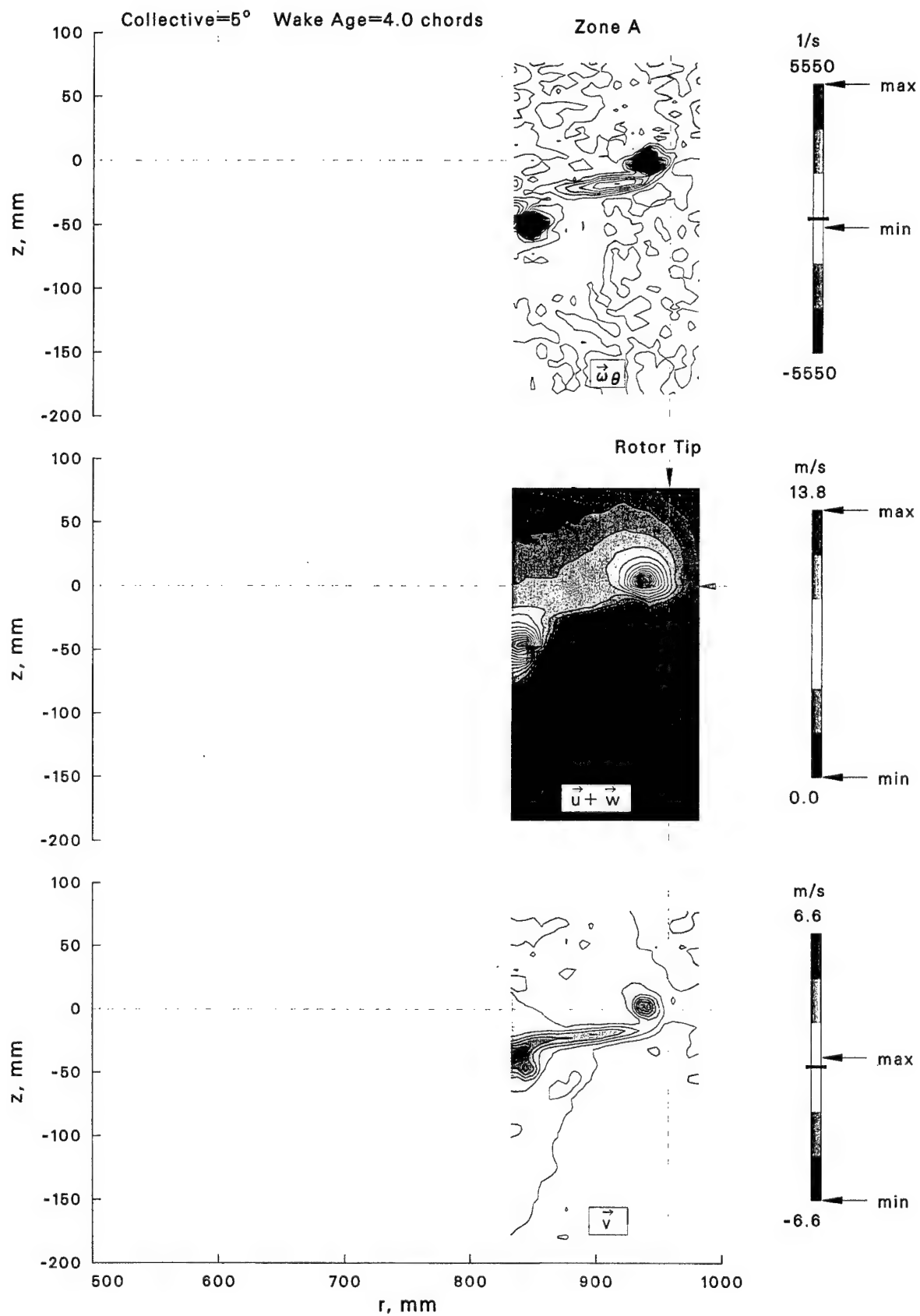
(b) Velocity and vorticity contour maps.

Figure 23: Concluded.



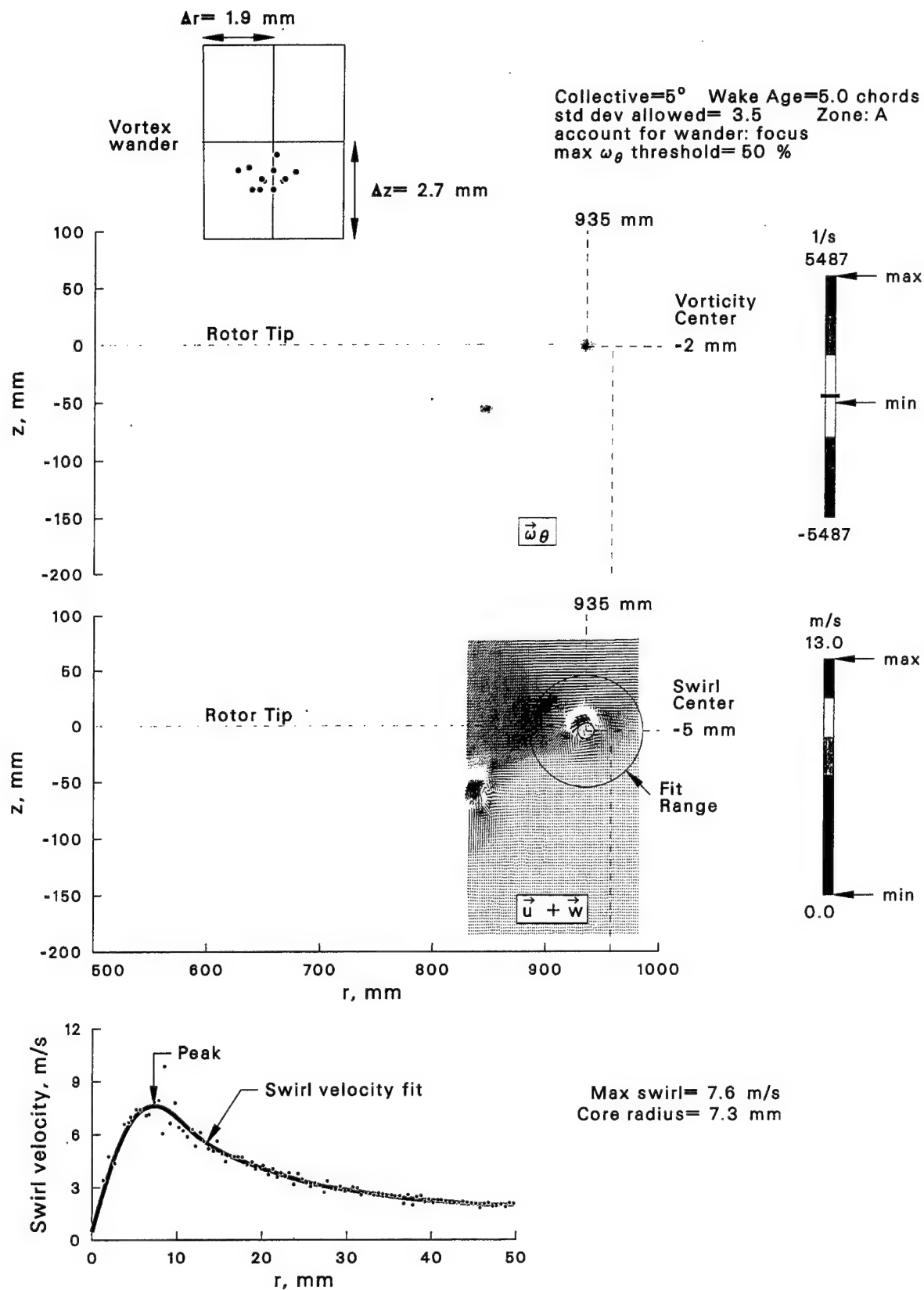
(a) Location and size of vortex.

Figure 24: Near wake at $\theta = 5^\circ$ and $\psi = 24.8^\circ$ (4 chords downstream from rotor tip).



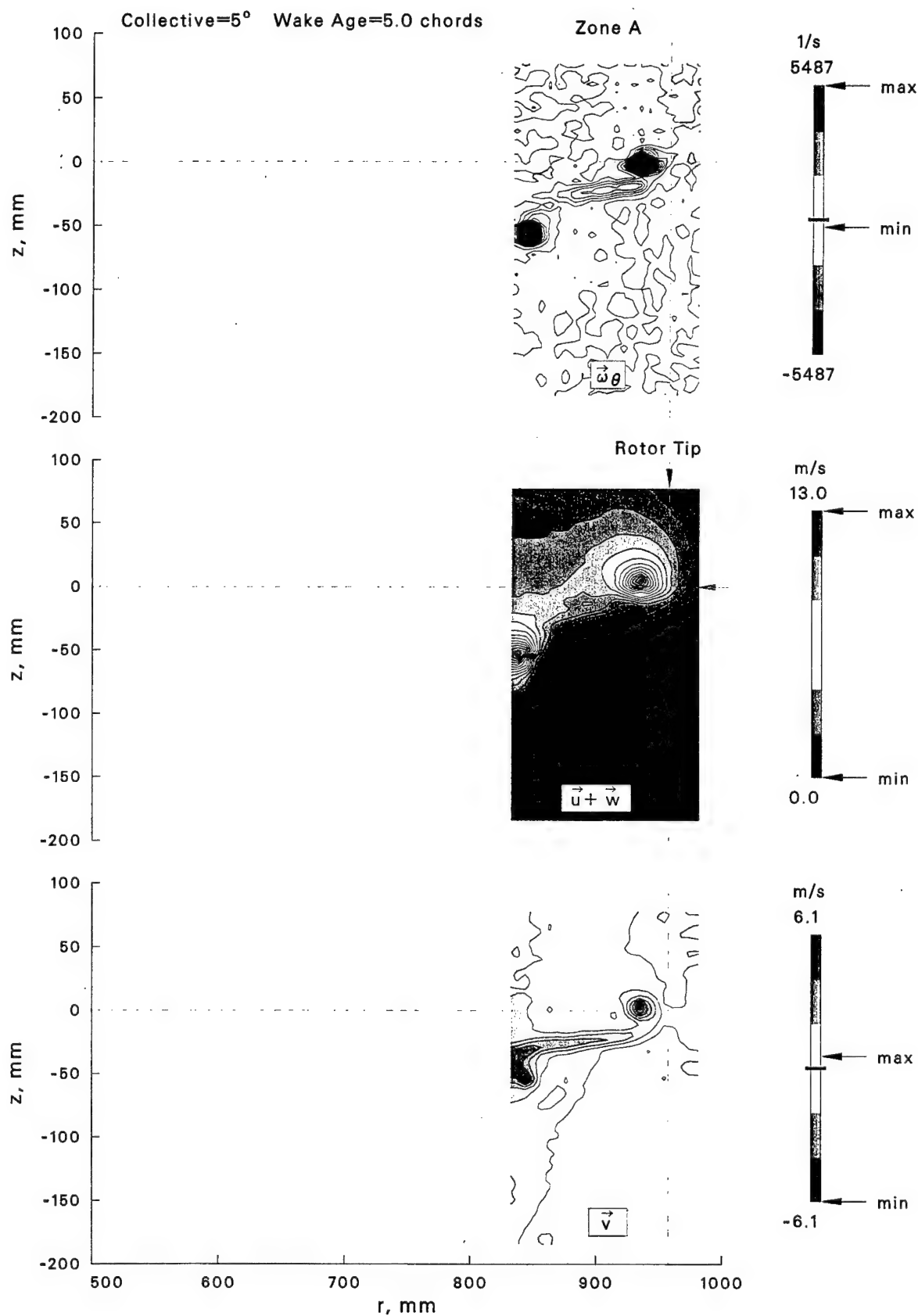
(b) Velocity and vorticity contour maps.

Figure 24: Concluded.



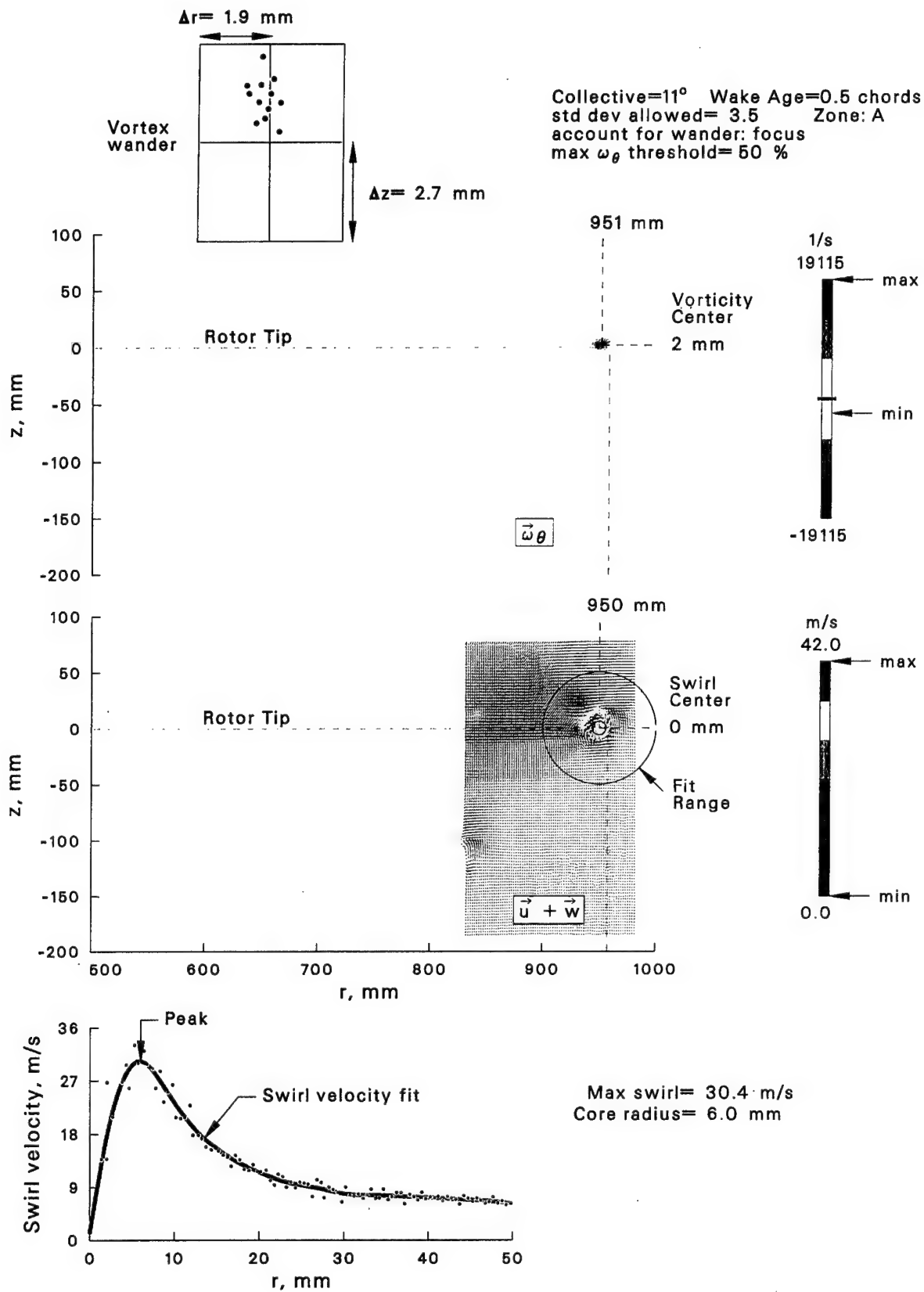
(a) Location and size of vortex.

Figure 25: Near wake at $\theta = 5^\circ$ and $\psi = 31.0^\circ$ (5 chords downstream from rotor tip).



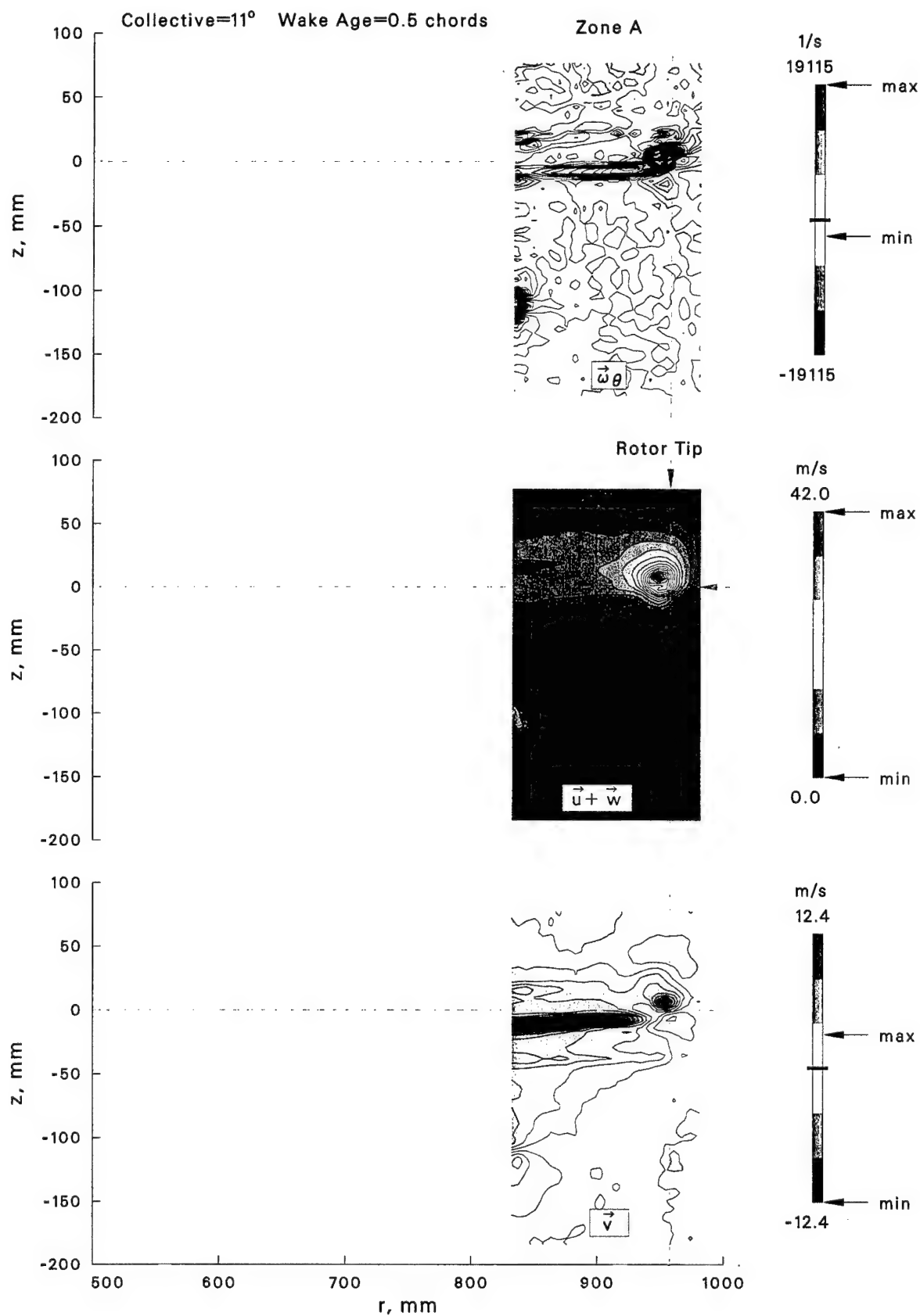
(b) Velocity and vorticity contour maps.

Figure 25: Concluded.



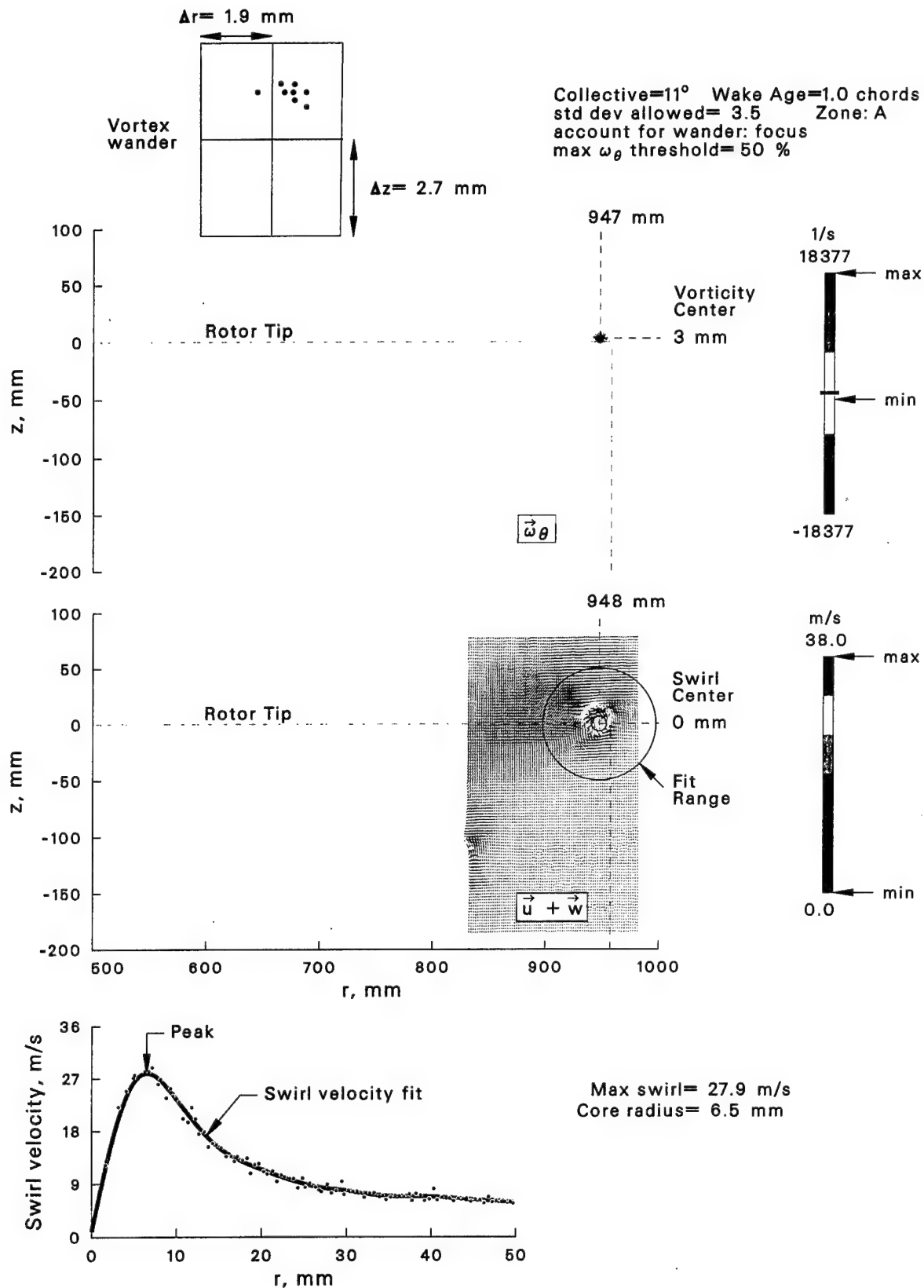
(a) Location and size of vortex.

Figure 26: Near wake at $\theta = 11^\circ$ and $\psi = 3.1^\circ$ (0.5 chord downstream from rotor tip).



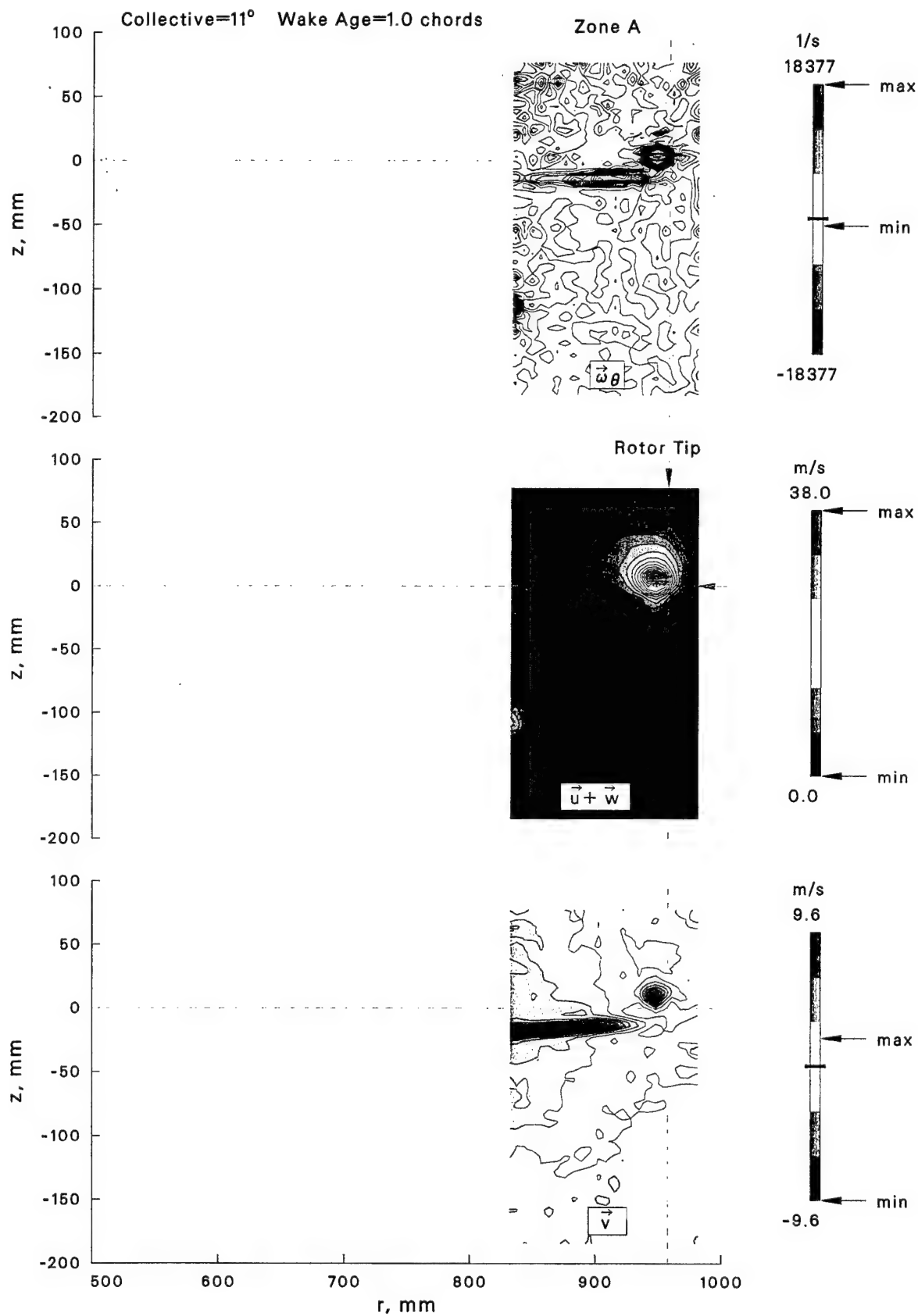
(b) Velocity and vorticity contour maps.

Figure 26: Concluded.



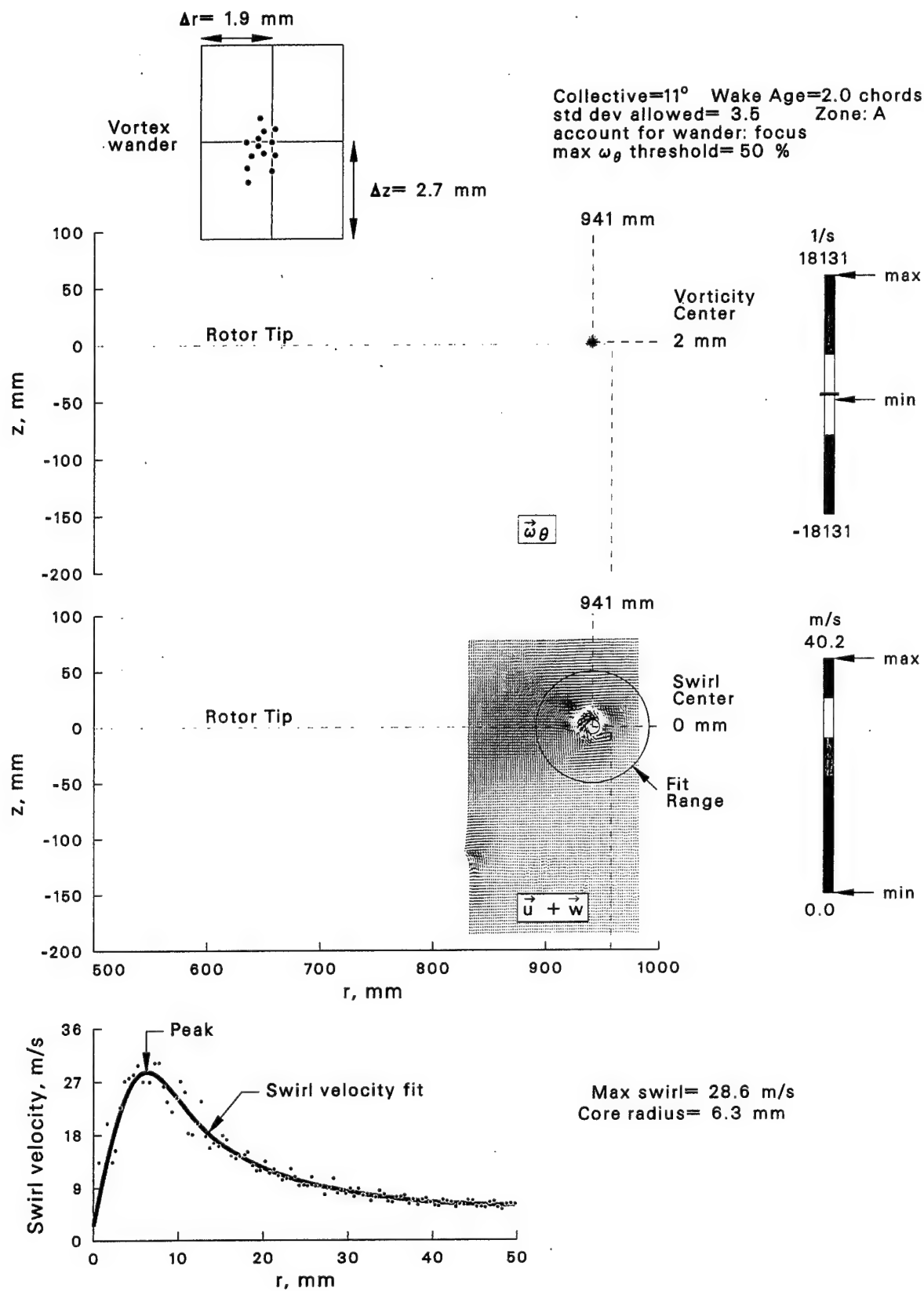
(a) Location and size of vortex.

Figure 27: Near wake at $\theta = 11^\circ$ and $\psi = 6.2^\circ$ (1 chord downstream from rotor tip).



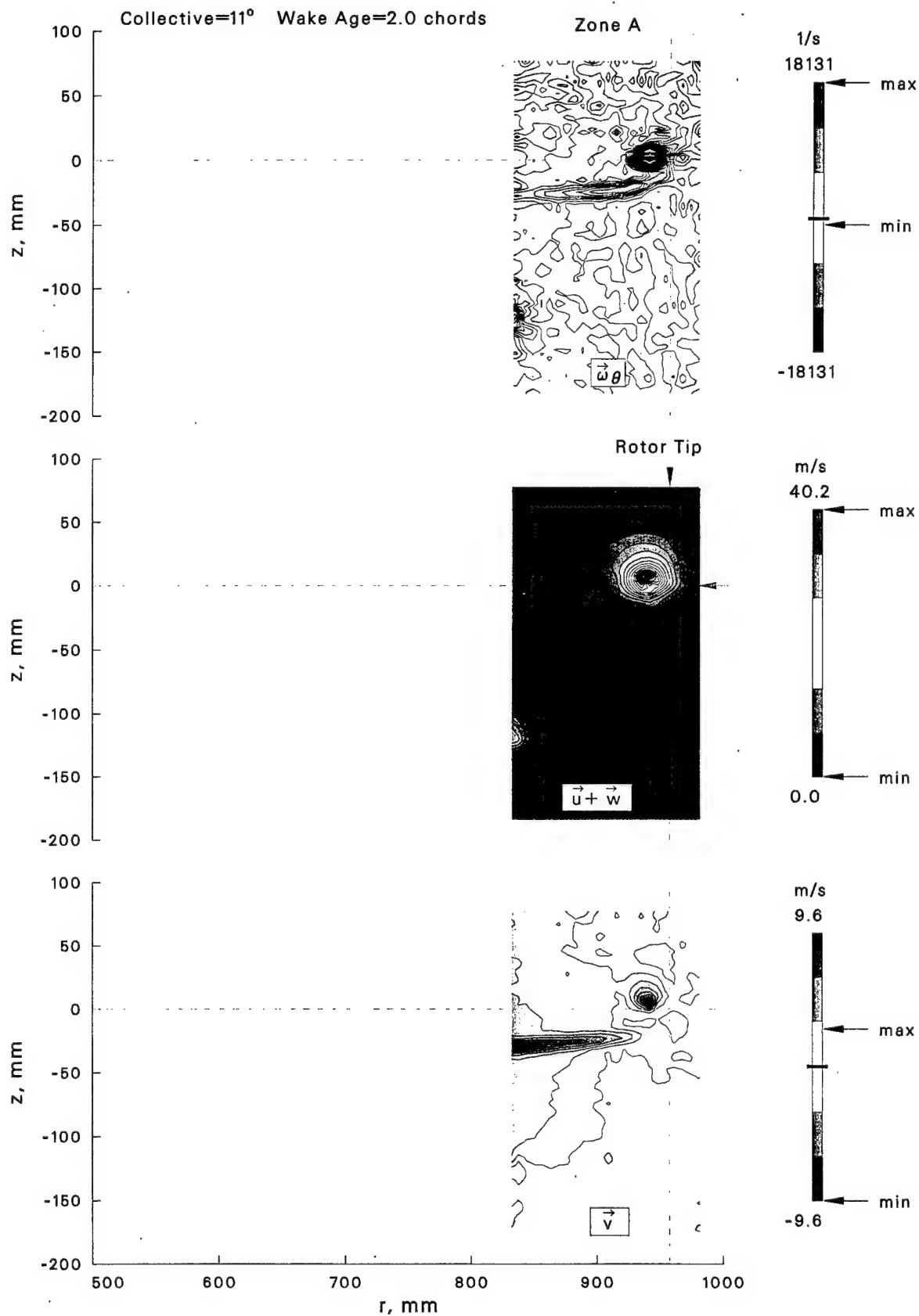
(b) Velocity and vorticity contour maps.

Figure 27: Concluded.



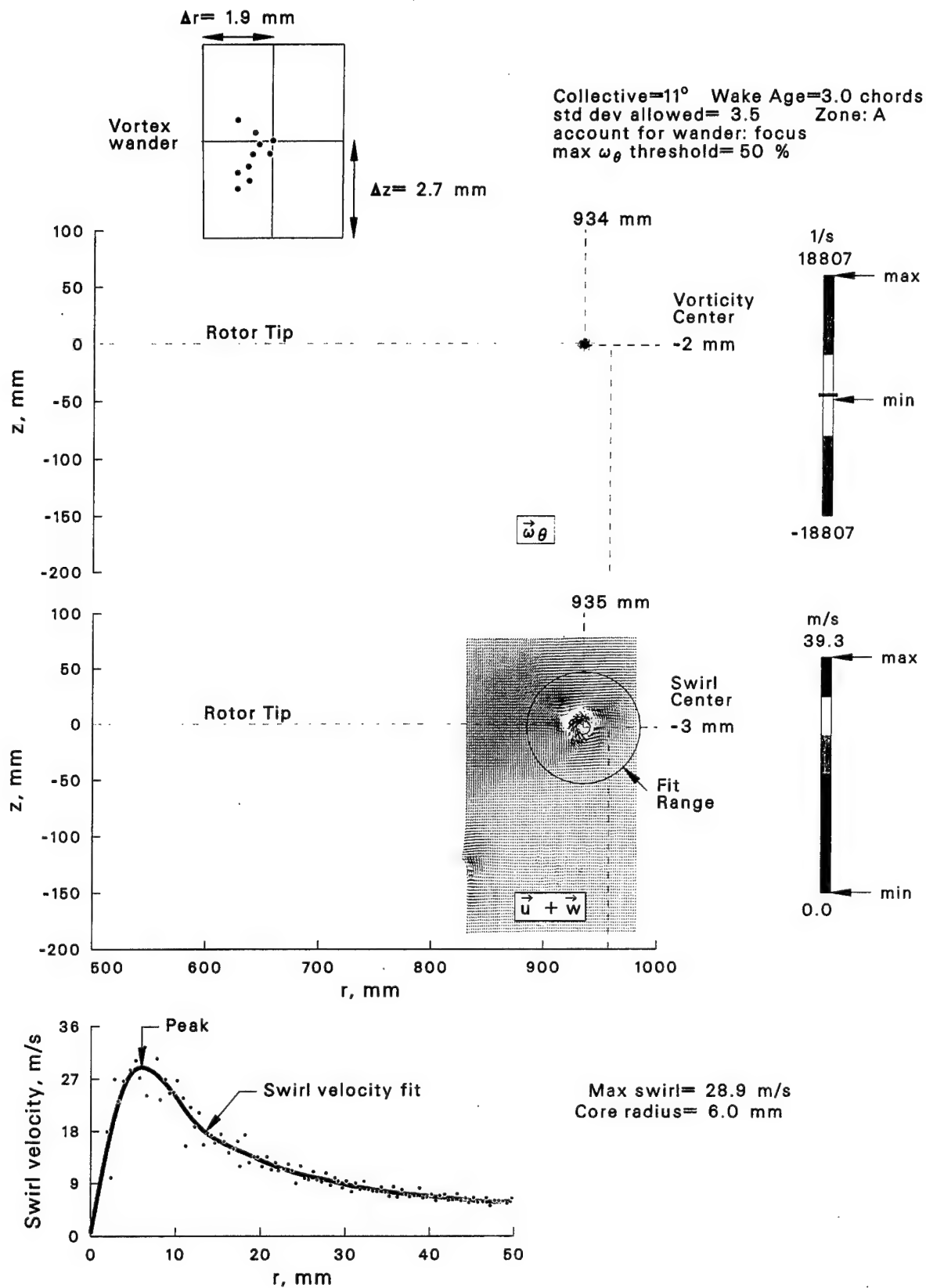
(a) Location and size of vortex.

Figure 28: Near wake at $\theta = 11^\circ$ and $\psi = 12.4^\circ$ (2 chords downstream from rotor tip).



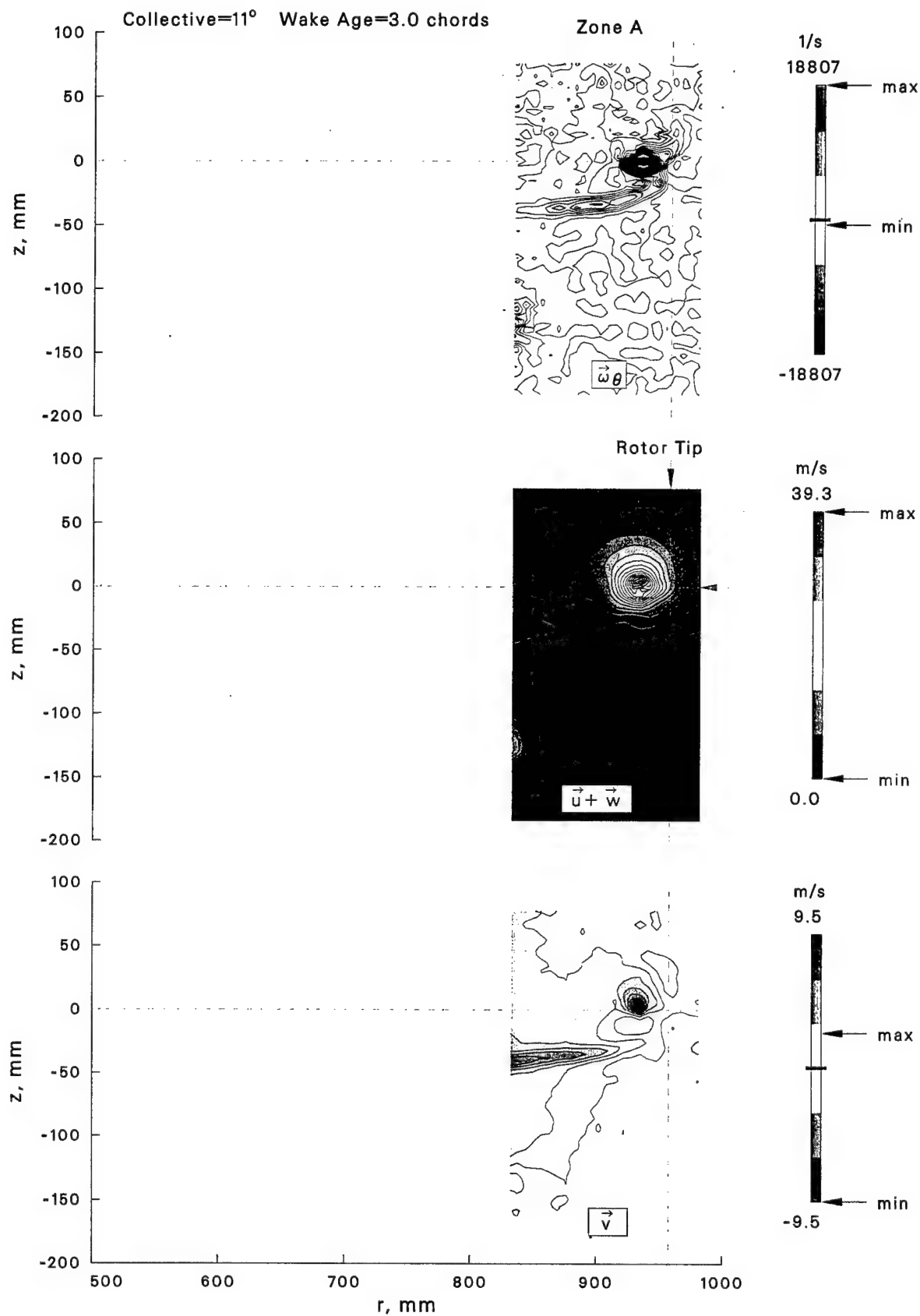
(b) Velocity and vorticity contour maps.

Figure 28: Concluded.



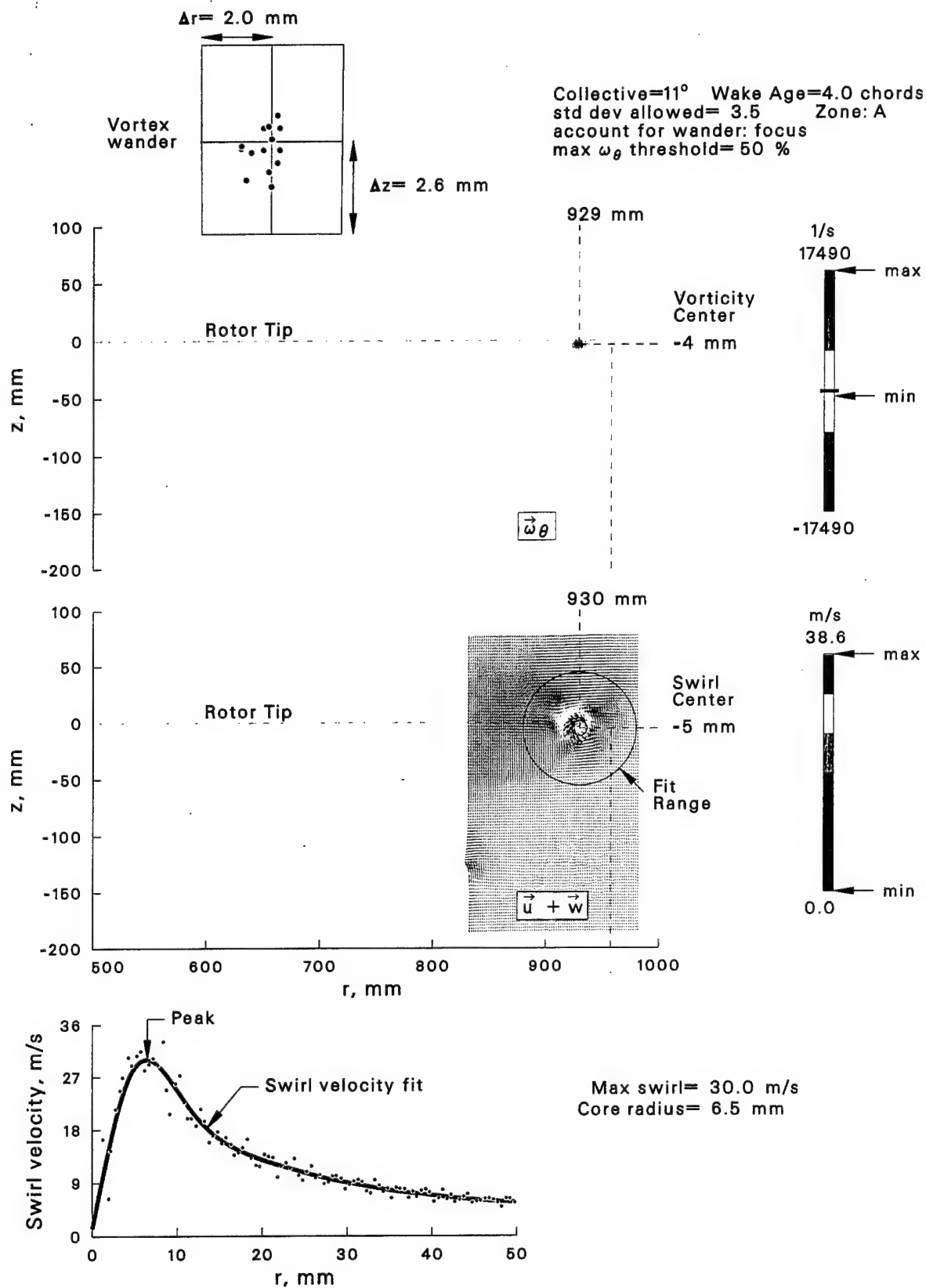
(a) Location and size of vortex.

Figure 29: Near wake at $\theta = 11^\circ$ and $\psi = 18.6^\circ$ (3 chords downstream from rotor tip).



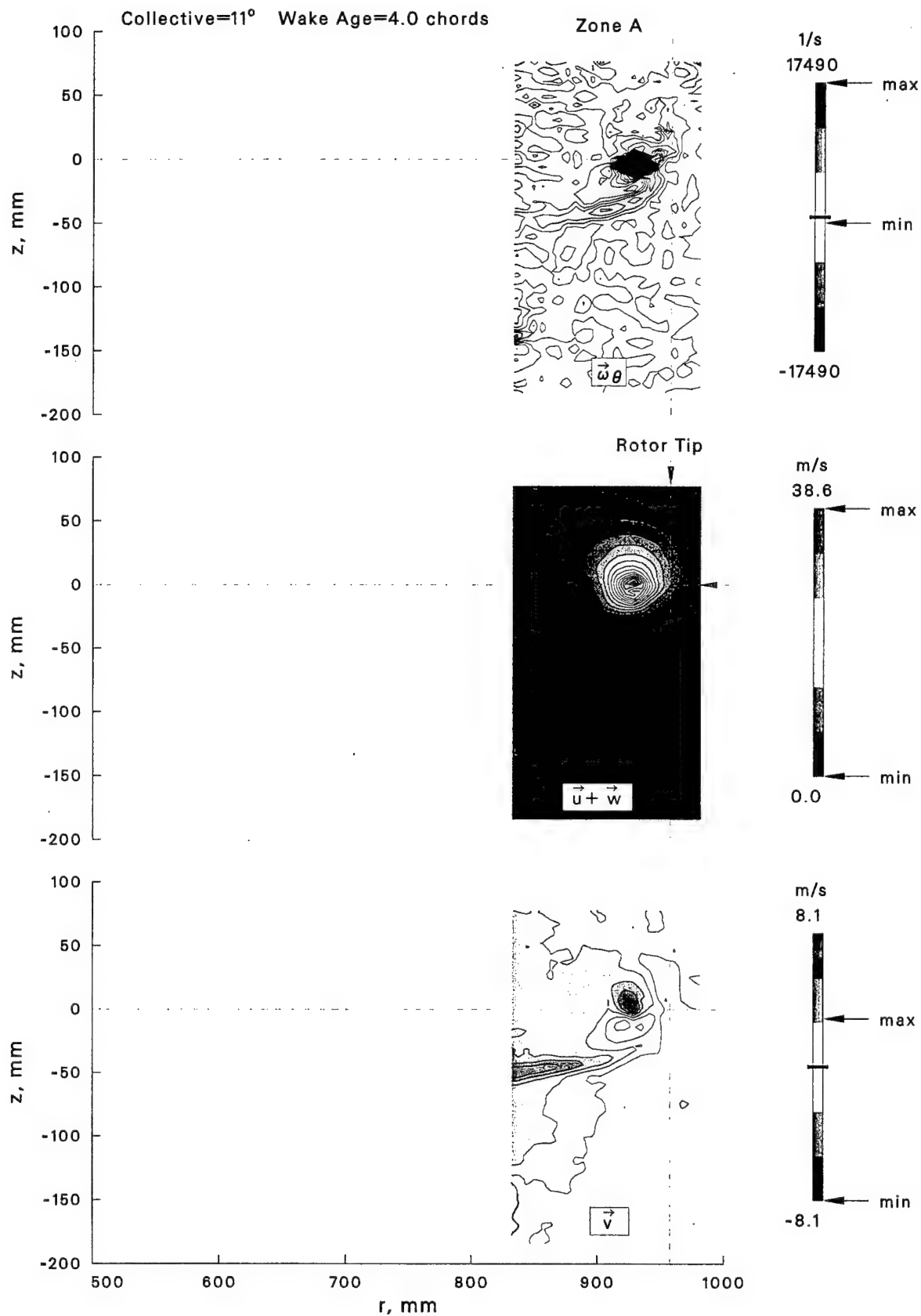
(b) Velocity and vorticity contour maps.

Figure 29: Concluded.



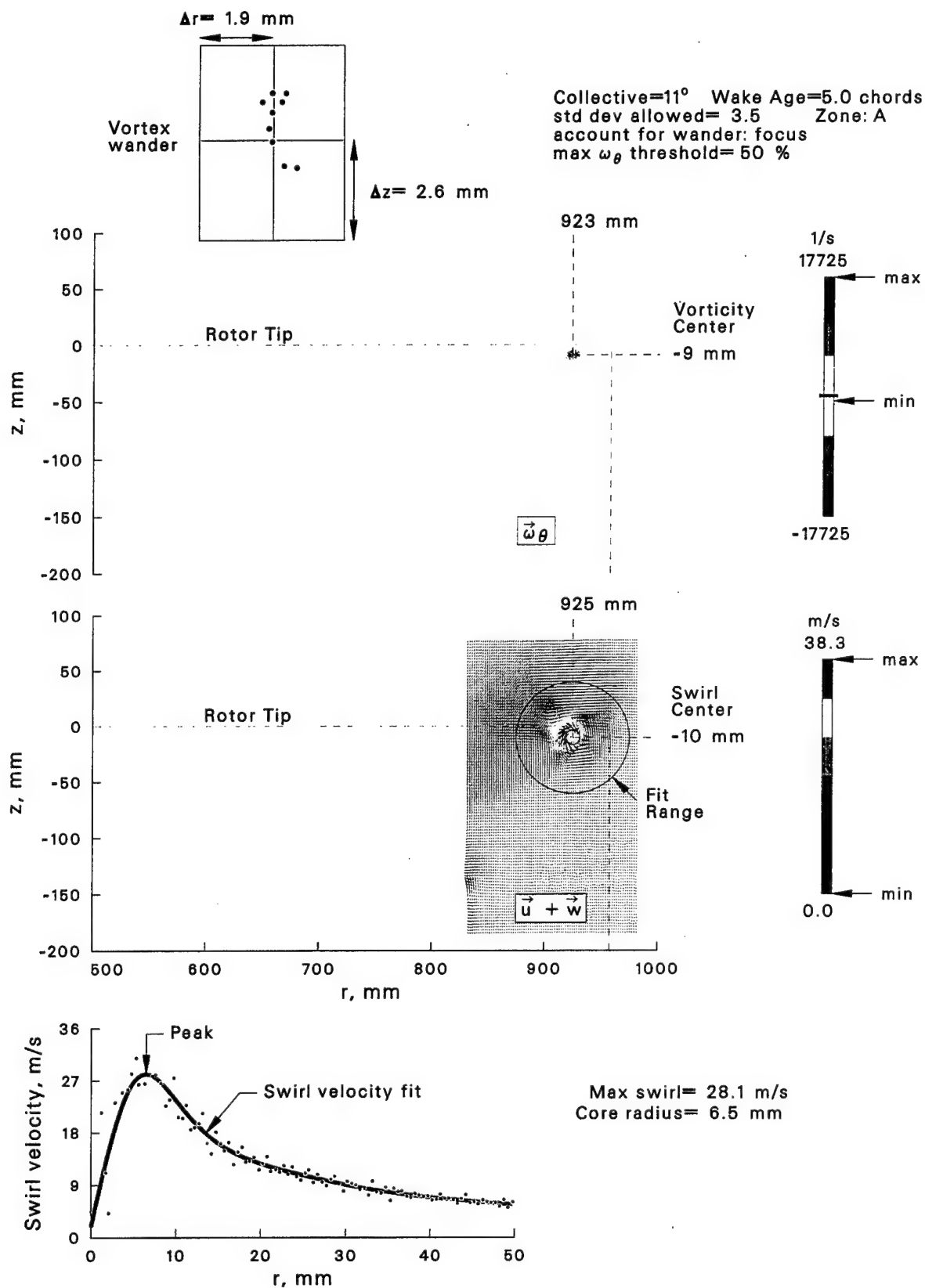
(a) Location and size of vortex.

Figure 30: Near wake at $\theta = 11^\circ$ and $\psi = 24.8^\circ$ (4 chords downstream from rotor tip).



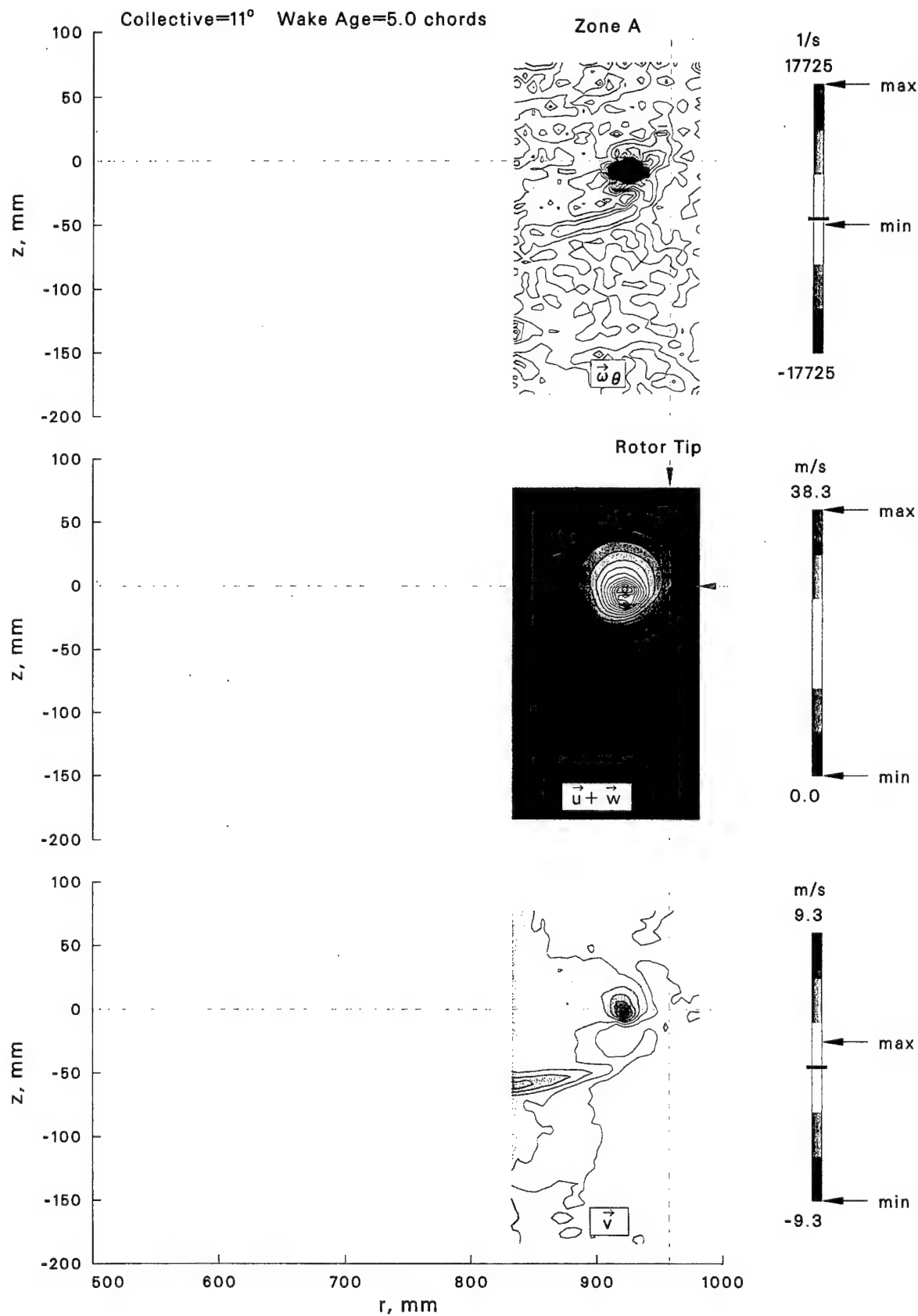
(b) Velocity and vorticity contour maps.

Figure 30: Concluded.



(a) Location and size of vortex.

Figure 31: Near wake at $\theta = 11^\circ$ and $\psi = 31.0^\circ$ (5 chords downstream from rotor tip).



(b) Velocity and vorticity contour maps.

Figure 31: Concluded.

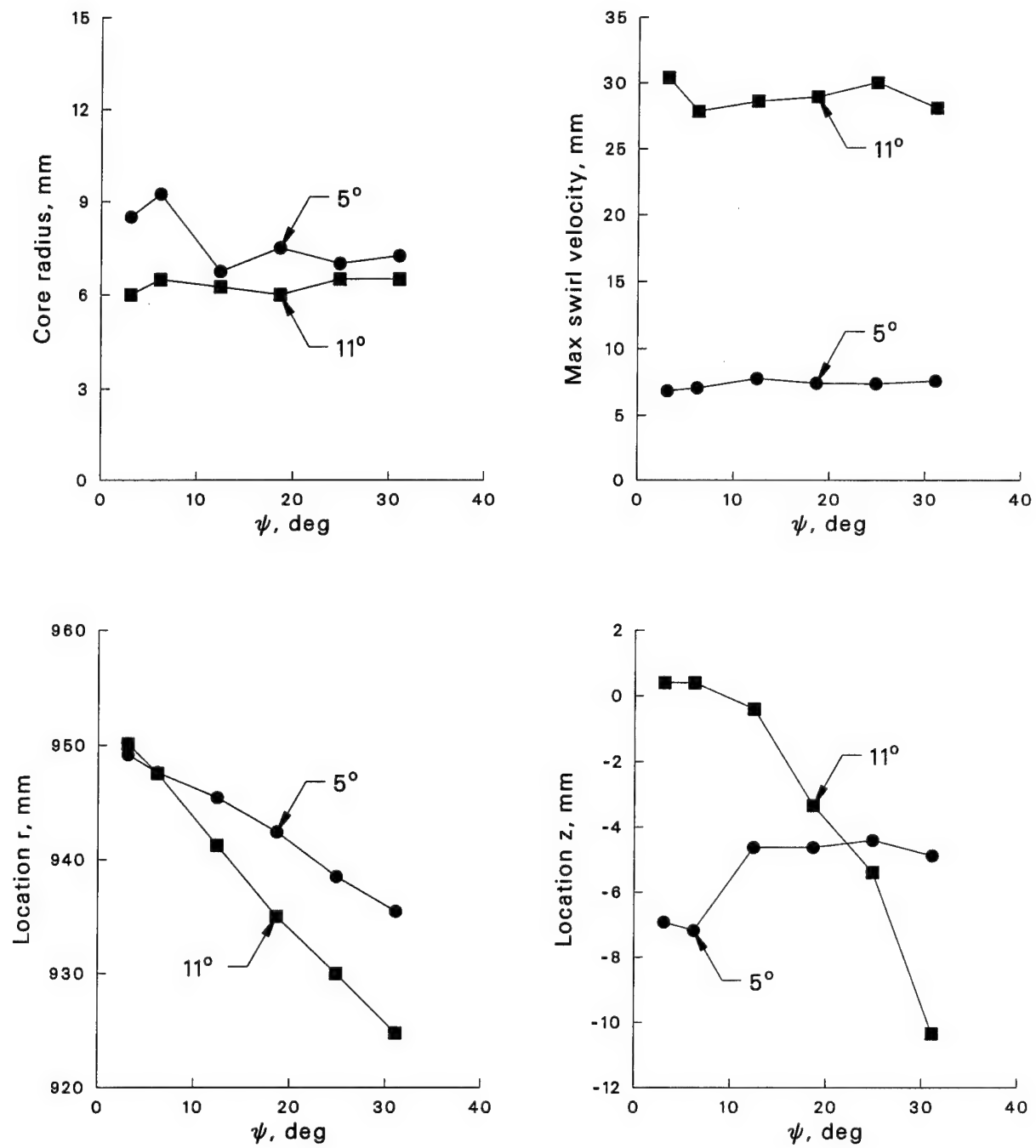


Figure 32: Vortex characteristics over initial 31.0° of wake.

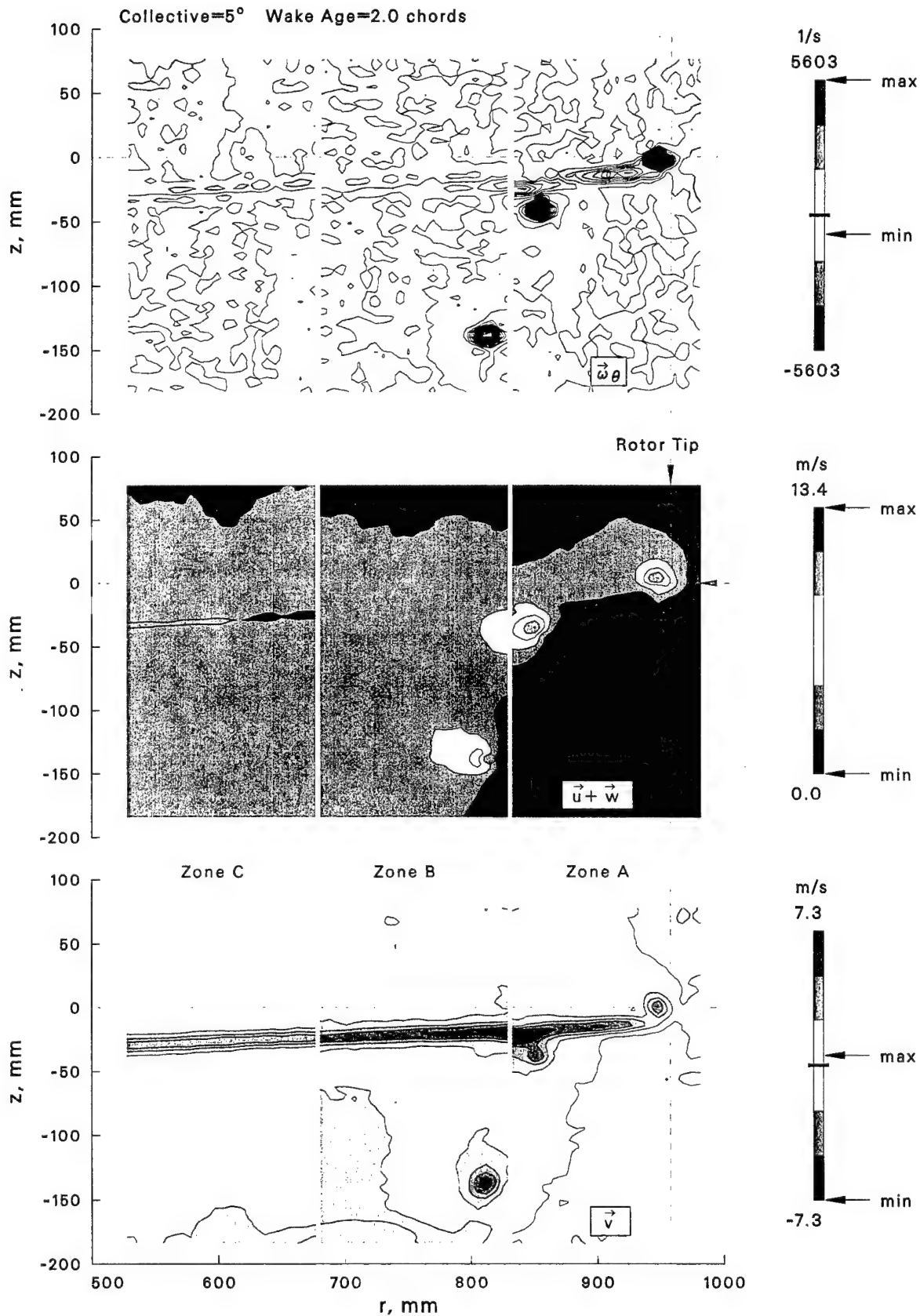
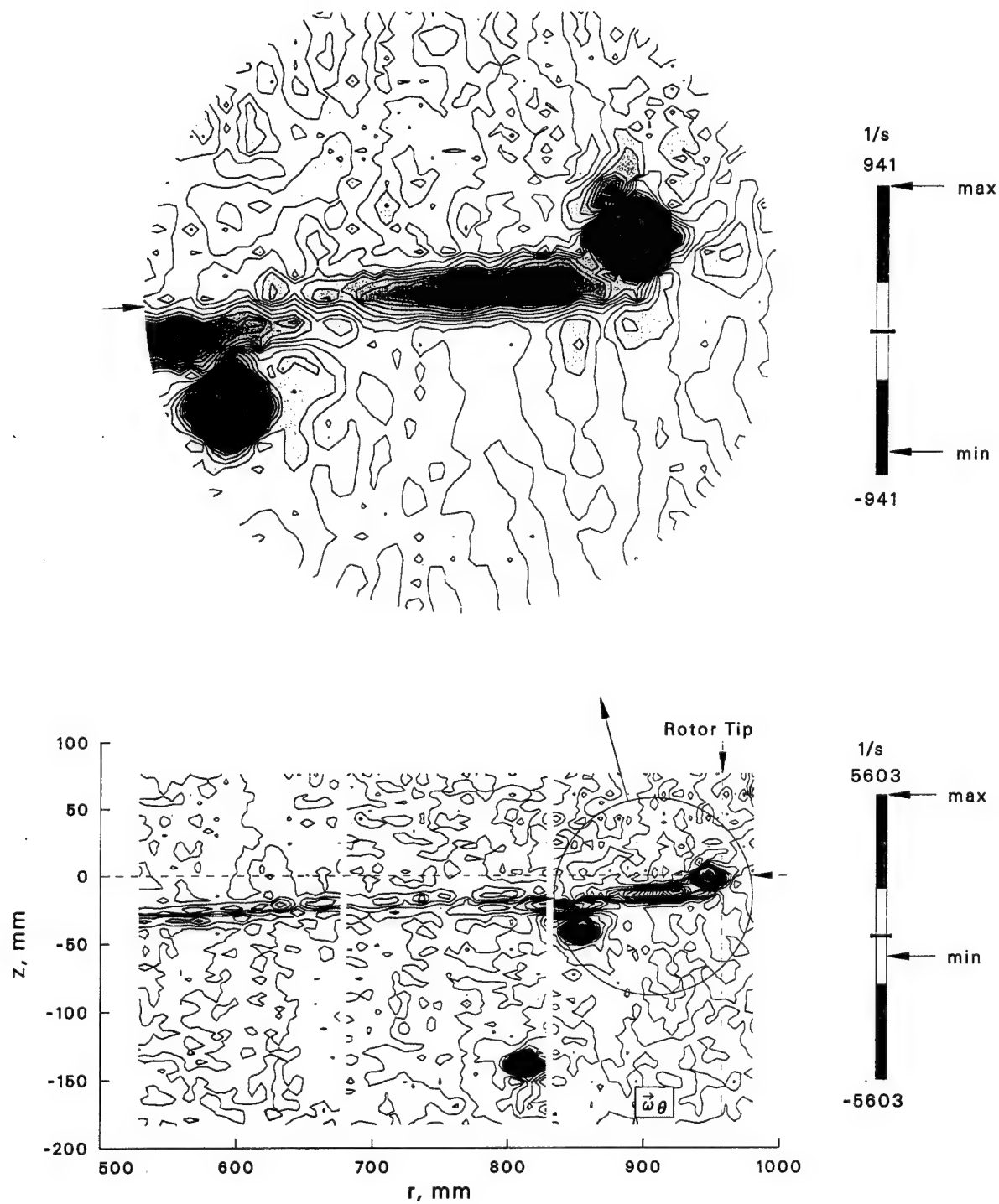


Figure 33: Velocity and vorticity contours covering 3 radial zones of flow for $\theta = 5^\circ$ and $\psi = 12.4^\circ$ (2 chords).

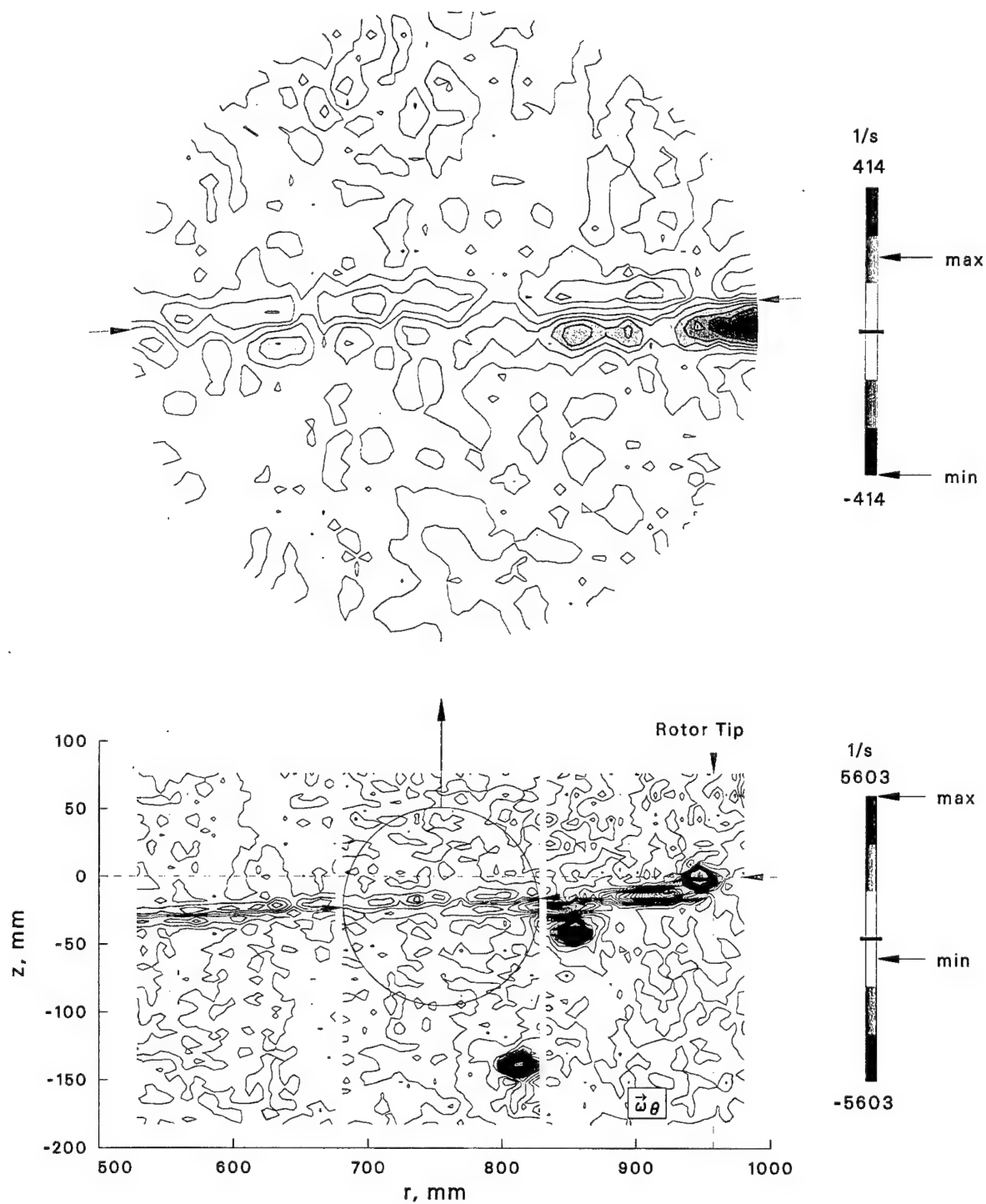
Collective= 5° Wake Age=2.0 chords



(a) Zone A.

Figure 34: Enlargement of vorticity contours for $\theta = 5^\circ$ and $\psi = 12.4^\circ$ (2 chords).

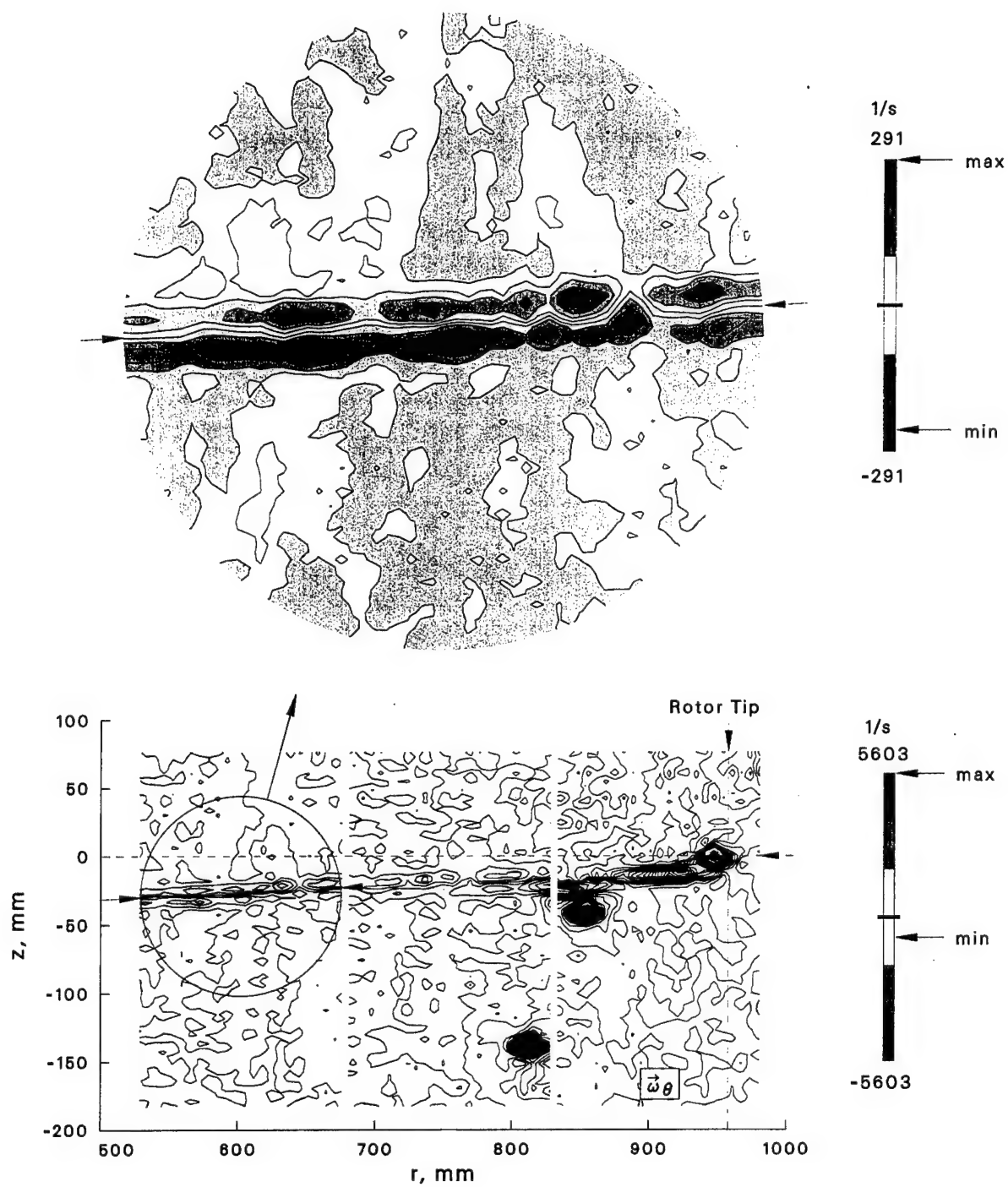
Collective=5° Wake Age=2.0 chords



(b) Zone B.

Figure 34: Continued.

Collective=5° Wake Age=2.0 chords



(c) Zone C.

Figure 34: Concluded.

Collective= 5° Wake Age=2.0 chords

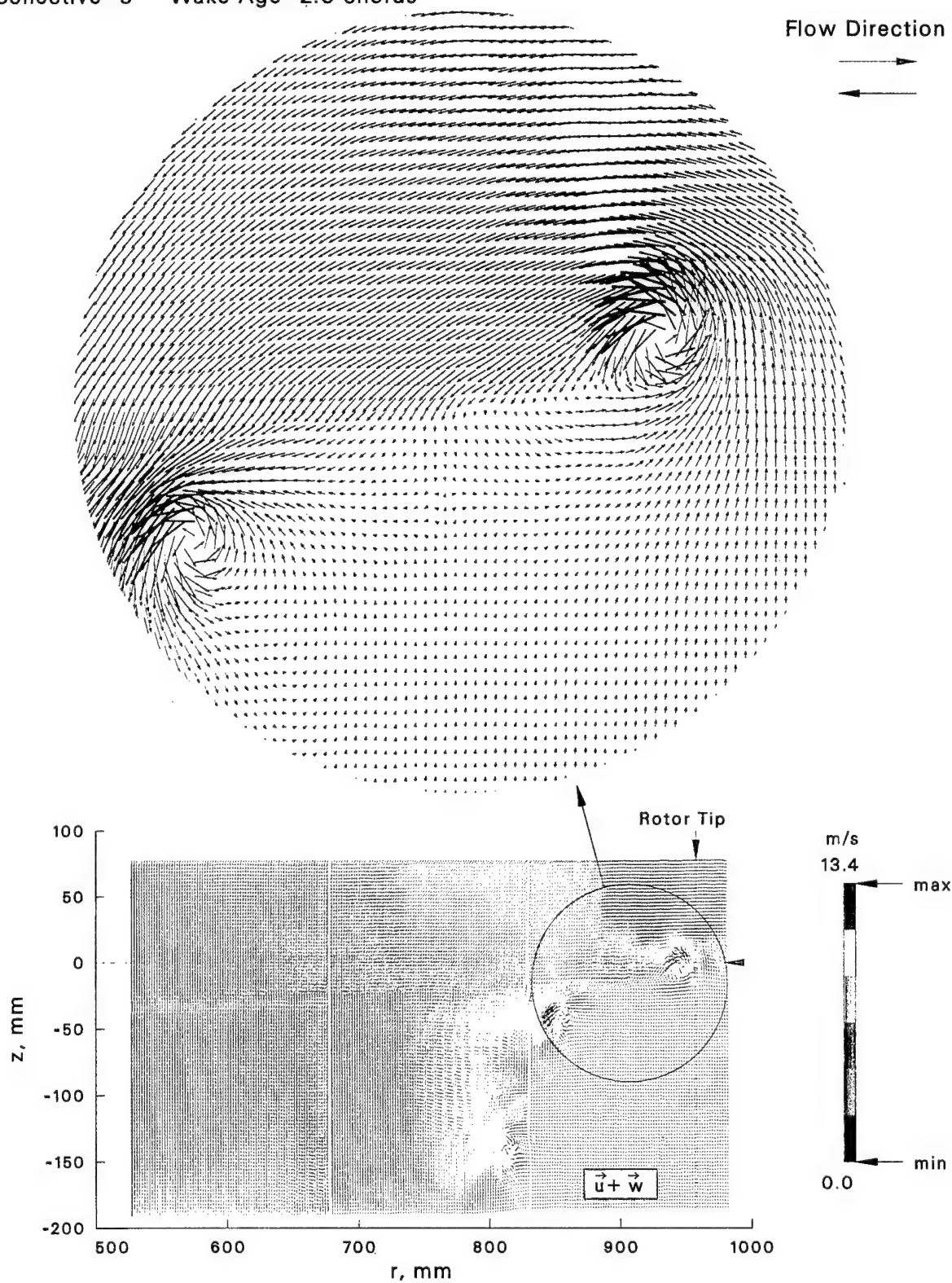


Figure 35: Enlargement of inplane velocity in zone A for $\theta = 5^\circ$ and $\psi = 12.4^\circ$ (2 chords).

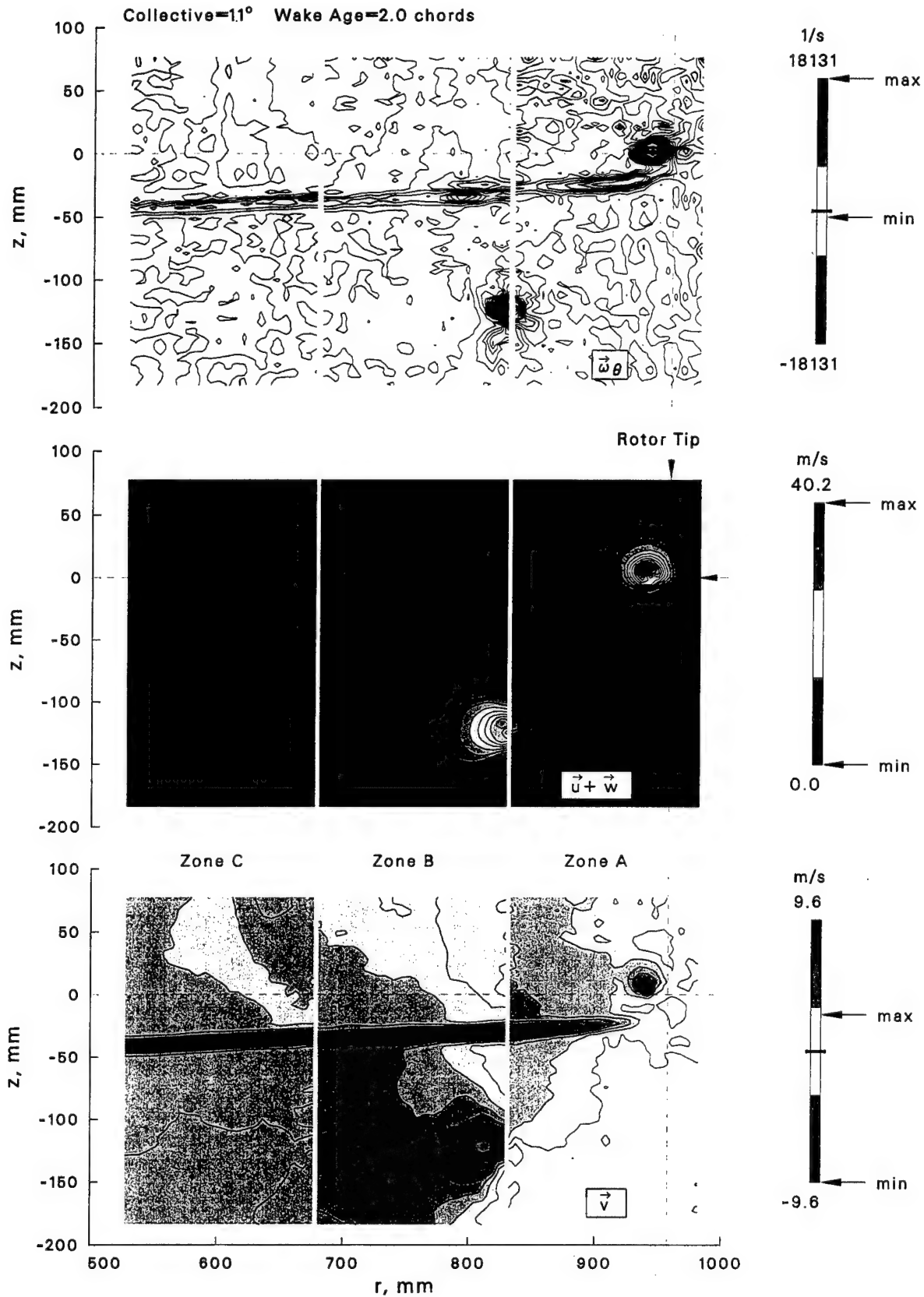
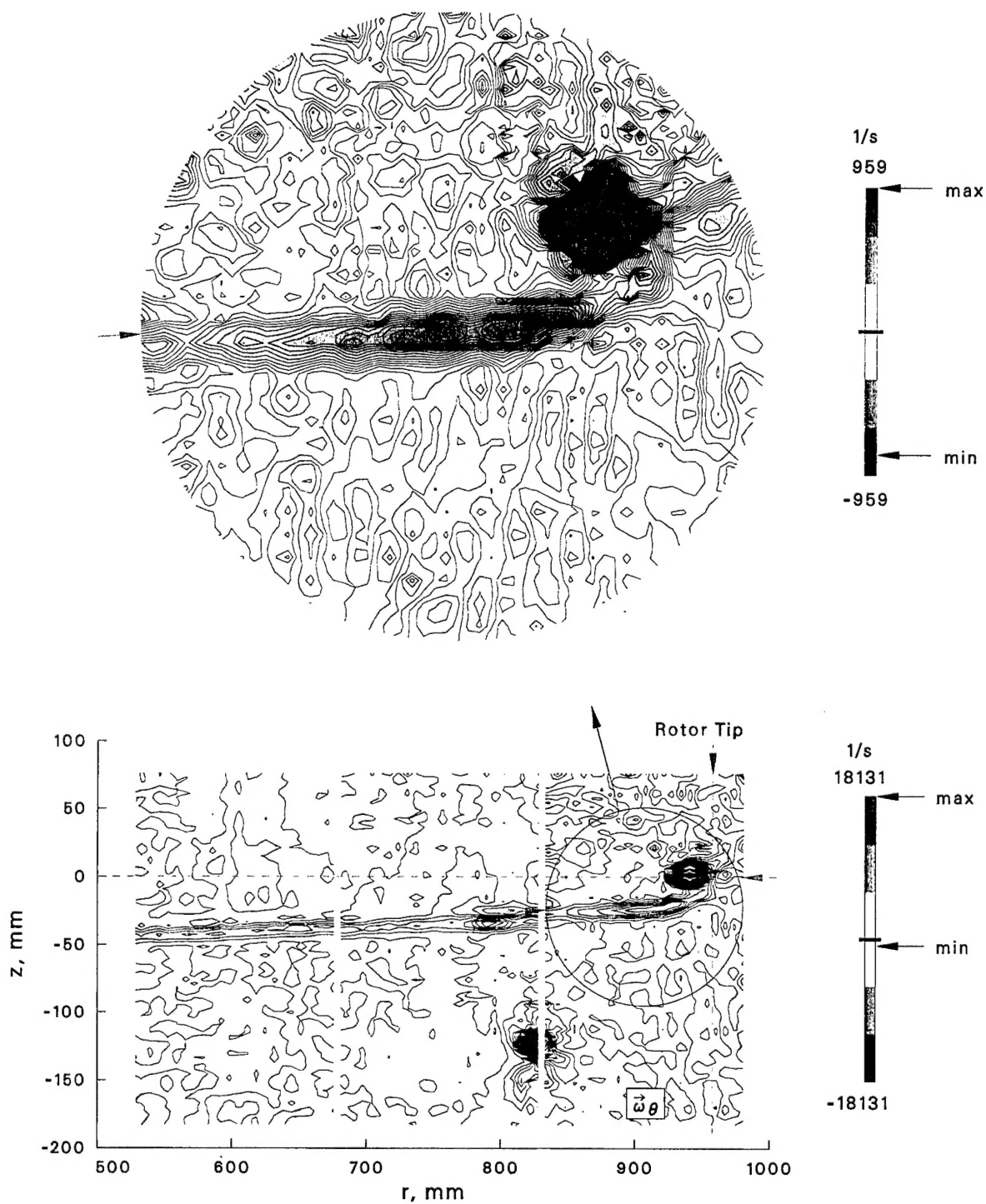


Figure 36: Velocity and vorticity contours covering 3 radial zones of flow for $\theta = 11^\circ$ and $\psi = 12.4^\circ$ (2 chords).

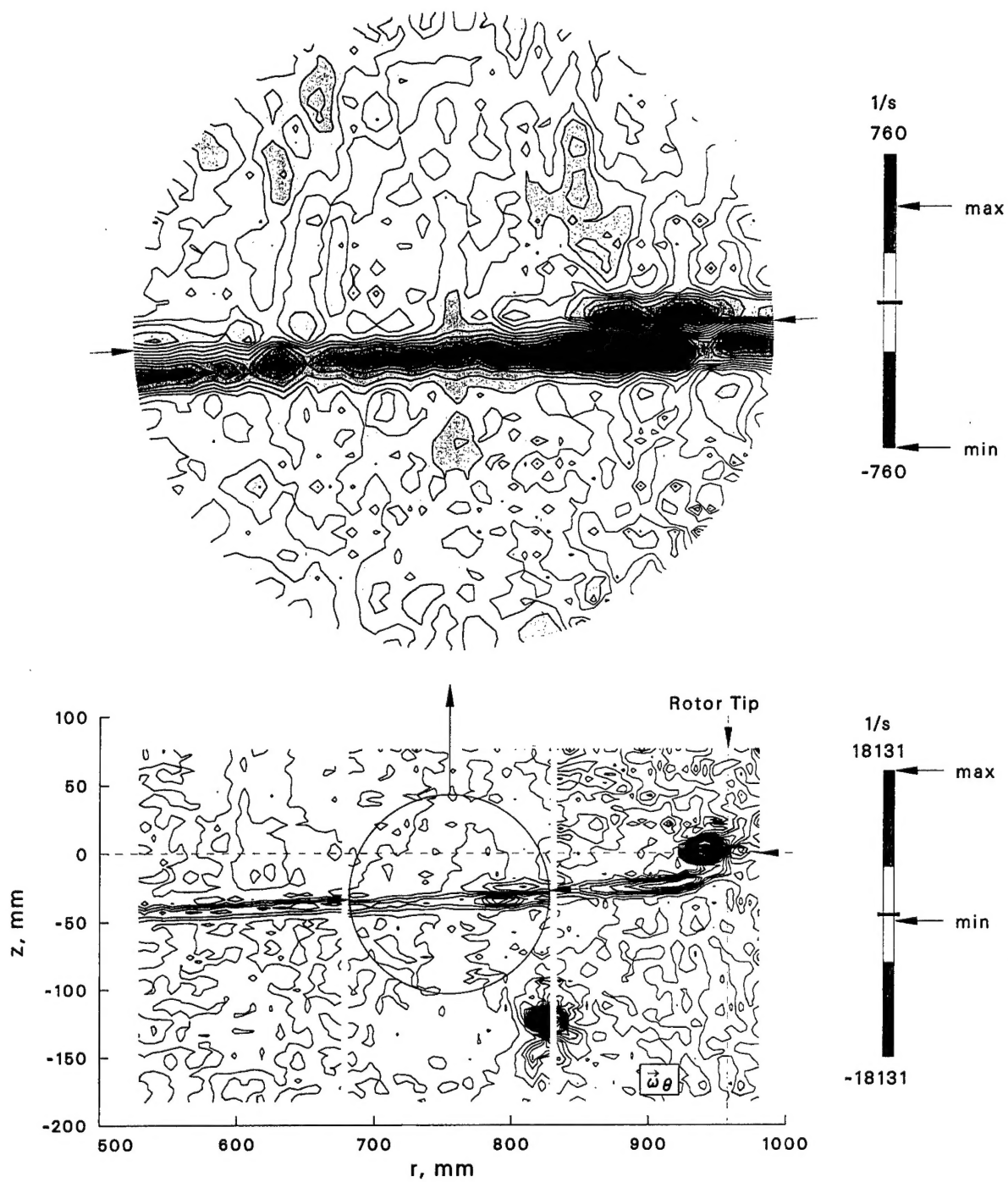
Collective= 11° Wake Age=2.0 chords



(a) Zone A.

Figure 37: Enlargement of vorticity contours for $\theta = 11^\circ$ and $\psi = 12.4^\circ$ (2 chords).

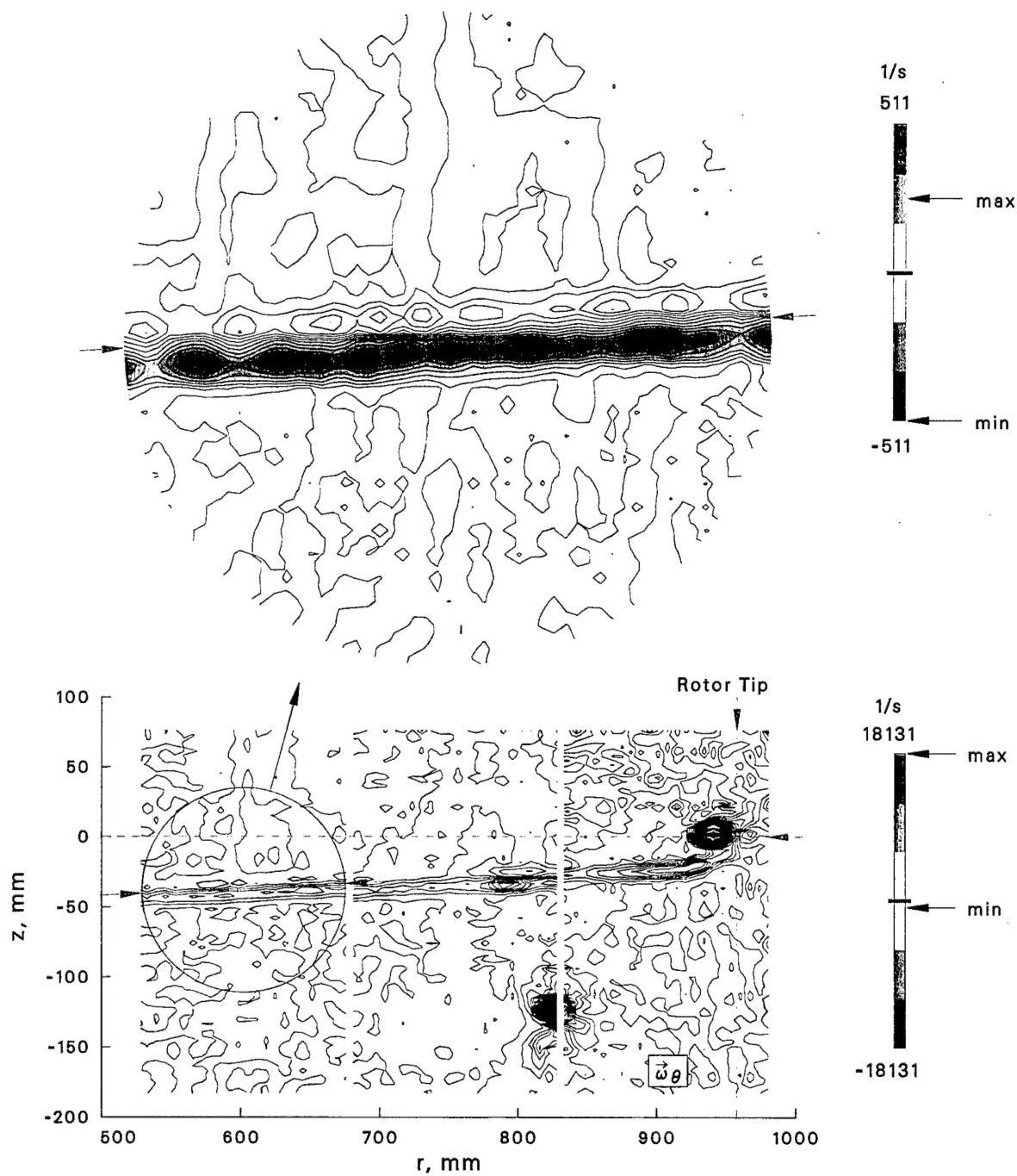
Collective=11° Wake Age=2.0 chords



(b) Zone B.

Figure 37: Continued.

Collective=11° Wake Age=2.0 chords



(c) Zone C.

Figure 37: Concluded.

REPORT DOCUMENTATION PAGEForm Approved
OMB No. 0704-0188

Public reporting burden for this collection of information is estimated to average 1 hour per response, including the time for reviewing instructions, searching existing data sources, gathering and maintaining the data needed, and completing and reviewing the collection of information. Send comments regarding this burden estimate or any other aspect of this collection of information, including suggestions for reducing this burden, to Washington Headquarters Services, Directorate for Information Operations and Reports, 1215 Jefferson Davis Highway, Suite 1204, Arlington, VA 22202-4302, and to the Office of Management and Budget, Paperwork Reduction Project (0704-0188), Washington, DC 20503.

1. AGENCY USE ONLY (Leave blank)		2. REPORT DATE June 2001	3. REPORT TYPE AND DATES COVERED Technical Memorandum	
4. TITLE AND SUBTITLE A Model Rotor in Axial Flight			5. FUNDING NUMBERS 712-10-12	
6. AUTHOR(S) K.W. McAlister, S.S. Huang, A.I. Abrego			7. PERFORMING ORGANIZATION NAME(S) AND ADDRESS(ES) Army/NASA Rotorcraft Division, Aeroflightdynamics Directorate (AMRDEC), U.S. Army Aviation and Missile Command. Ames Research Center, Moffett Field, CA 94035	
8. PERFORMING ORGANIZATION REPORT NUMBER A-00V0045			9. SPONSORING/MONITORING AGENCY NAME(S) AND ADDRESS(ES) National Aeronautics and Space Administration Washington, DC 20546-0001 and U.S. Army Aviation and Missile Command, Redstone Arsenal, AL 35898-5000	
10. SPONSORING/MONITORING AGENCY REPORT NUMBER NASA/TM-2001-210925 AFDD/TR-01-A-004			11. SUPPLEMENTARY NOTES Point of Contact: K.W. McAlister, Ames Research Center, MS 215-1, Moffett Field, CA 94035-1000	
12a. DISTRIBUTION/AVAILABILITY STATEMENT Unclassified - Unlimited Subject Category 02 Distribution: Standard Availability: NASA CASI (301) 621-0390			12b. DISTRIBUTION CODE	
13. ABSTRACT (Maximum 200 words) A model rotor was mounted horizontally in the settling chamber of a wind tunnel to obtain performance and wake structure data under low climb conditions. The immediate wake of the rotor was carefully surveyed using 3-component particle image velocimetry to define the velocity and vortical content of the flow, and used in a subsequent study to validate a theory for the separate determination of induced and profile drag. Measurements were obtained for two collective pitch angles intended to render a predominately induced drag state and another with a marked increase in profile drag. A majority of the azimuthally directed vorticity in the wake was found to be concentrated in the tip vortices. However, adjacent layers of inboard vorticity with opposite sense were clearly present. At low collective, the close proximity of the tip vortex from the previous blade caused the wake from the most recent blade passage to be distorted. The deficit velocity component that was directed along the azimuth of the rotor blade was never more than 15% of the rotor tip speed, and except for the region of the tip vortex, appeared to have totally disappeared from the wake left by the previous blade.				
14. SUBJECT TERMS Rotor wake, Trailing vortex, Model rotor, Particle image velocimetry			15. NUMBER OF PAGES 64	
16. PRICE CODE			17. SECURITY CLASSIFICATION OF REPORT Unclassified	
18. SECURITY CLASSIFICATION OF THIS PAGE Unclassified			19. SECURITY CLASSIFICATION OF ABSTRACT Unclassified	
20. LIMITATION OF ABSTRACT				